

**Titre:** Development and Investigation of High-Performance Thermoplastic Composites for Fused Filament Fabrication of Sandwich Panel Structures  
**Title:**

**Auteur:** Dogan Arslan  
**Author:**

**Date:** 2024

**Type:** Mémoire ou thèse / Dissertation or Thesis

**Référence:** Arslan, D. (2024). Development and Investigation of High-Performance Thermoplastic Composites for Fused Filament Fabrication of Sandwich Panel Structures [Thèse de doctorat, Polytechnique Montréal]. PolyPublie.  
**Citation:** <https://publications.polymtl.ca/61784/>

 **Document en libre accès dans PolyPublie**  
Open Access document in PolyPublie

**URL de PolyPublie:** <https://publications.polymtl.ca/61784/>  
**PolyPublie URL:**

**Directeurs de recherche:** Martin Lévesque, Daniel Therriault, & Mihaela Mihai  
**Advisors:**

**Programme:** Génie mécanique  
**Program:**

**POLYTECHNIQUE MONTRÉAL**

affiliée à l'Université de Montréal

**Development and investigation of high-performance thermoplastic composites  
for fused filament fabrication of sandwich panel structures**

**DOGAN ARSLAN**

Département de génie mécanique

Thèse présentée en vue de l'obtention du diplôme de *Philosophiæ Doctor*

Génie mécanique

Décembre 2024

# **POLYTECHNIQUE MONTRÉAL**

affiliée à l'Université de Montréal

Cette thèse intitulée :

## **Development and investigation of high-performance thermoplastic composites for fused filament fabrication of sandwich panel structures**

présentée par **Dogan ARSLAN**

en vue de l'obtention du diplôme de *Philosophiæ Doctor*

a été dûment acceptée par le jury d'examen constitué de :

**Basil D. FAVIS**, président

**Martin LÉVESQUE**, membre et directeur de recherche

**Daniel THERRIAULT**, membre et codirecteur de recherche

**Mihaela MIHAI**, membre et codirectrice de recherche

**Eduardo Antonio Julian RUIZ**, membre

**Nicolas CARRERE**, membre externe

**DEDICATION**

*To my family and loved ones,*

*“Dear friend, all theory is gray,  
And green the golden tree of life.”*

J. W. Goethe



## ACKNOWLEDGEMENTS

First, I would like to express my sincere appreciation to my supervisors, Prof. Martin Lévesque, Prof. Daniel Therriault, and Dr. Mihaela Mihai for their guidance, encouragement, and support during this study. It was a wonderful opportunity to work with them. I appreciate not just their scientific supervision but their great personality. I am also grateful for the financial support during my research.

I would like to thank my defence jury, Prof. Basil Favis, Prof. Eduardo Ruiz, and Prof. Nicolas Carrere for their time and effort they put to provide the feedback to improve the quality of the manuscript.

I would like to thank the technical team of NRC Tarik Beragrag, Ali Ihid, Patrick Gagnon, and Dr. Sajjad Saeidlou for their support in composites manufacturing and running experiments in their laboratories.

I would like to thank Dr. Rouhollah Farahani and Dr. Kambiz Chizari for their administrative, technical and moral support.

I also express my gratitude to Yanik Laundry-Ducharme for technical help during the study. I would like to thank especially Matthieu Gauthier, Marie-Hélène Bernier, and Claire Cerclé for equipment training at the beginning of the study.

Many thanks to Dr. Facundo Sosa-Rey for technical support for micro-CT image processing.

I also would like to thank all my friends at LM2 for the great environment and support: Facundo, Alessandra, JF, Juliette, Olivier, Olivier, Mathieu, Yahya, Paul, Ferran, Rui, Iee Lee, Gabriel, Anamaria and many others.

Over the last few years, I have had the pleasure of meeting different people who are truly generous and helpful. In many rough moments, they helped me through words or actions and made me motivated by friendship or just kindness. I would like to especially thank Emre, Aslı, Tallwinder, Molly, Burcu, Huseyin, Murat and Deniz.

My heartfelt thanks to Prof. M. Reza Nofar for believing in me, opening doors to my PhD journey, introducing me to my PhD family, and igniting a new chapter in my career.

My deepest gratitude goes to my partner Hélène and my family for their support and motivation. There is no right word to describe my feeling of appreciation to them.

## RÉSUMÉ

La fabrication par dépôt de filament fondu (FFF) de polymères à haute température offre un potentiel considérable pour l'industrie aérospatiale. Cela s'explique par la flexibilité de la FFF dans la création de structures complexes, ainsi que par les propriétés mécaniques, thermiques et ignifuges de certains polymères résistants à haute température. Cependant, plusieurs défis sont associés à la FFF des polymères à haute température, en particulier lorsqu'ils sont renforcés par des fibres courtes. Ces défis incluent le traitement à haute température, la viscosité élevée, les difficultés d'extrusion des filaments, la formation de porosité, le comportement thermique tel qu'amorphe et/ou semi-cristallin de la matrice et l'interface fibre-matrice, qui peuvent tous avoir un impact sur les propriétés mécaniques finales des pièces imprimées. De plus, le choix d'une matrice polymère appropriée et le développement de matériaux composites respectant les exigences strictes de certification de l'industrie aérospatiale représentent un défi important. La technologie FFF, qui est relativement récente, manque de procédés standardisés, et les propriétés des pièces imprimées par FFF ne sont pas encore complètement comprises, en comparaison avec celles produites par des techniques de fabrication conventionnelles.

Le travail présenté dans cette thèse propose le développement des différentes formulations de matrices polymères polyetherimide (PEI) amorphe et de polysulfure de phényle (PPS) semi-cristallin, renforcées avec de la fibre courte de carbone recyclée (rCF) et des particules de thermal black (TB). Quatre (4) formulations composites différentes ont été fabriquées pour chaque matrice. Initialement, les composites contenaient 20 % en poids de rCF, qui ont été progressivement remplacées par des particules de TB, par incréments de 5 % en poids. Après leur extrusion, les composites ont été moulés par injection (IM) et aussi ont été extrudés sous forme des filaments. Ensuite, les propriétés mécaniques, thermiques et microstructurales des pièces imprimées par FFF et celles des pièces moulées par injection ont été analysées et comparées.

Les propriétés mécaniques ont été étudiées en termes de performance en traction, en flexion et à l'impact. L'incorporation de rCF a significativement amélioré les propriétés mécaniques des composites PEI et PPS. L'incorporation de 20 % en poids de rCF a augmenté le module de traction de la matrice PEI moulée par injection de 3.2 GPa à 6.2 GPa, tandis que pour le PPS moulé par injection, le module de traction est passé de 3.5 GPa à 20 GPa. L'efficacité du renforcement avec un chargement en rCF pour les spécimens IM de PEI et de PPS peut être attribuée aux différences

dans leurs caractéristiques structurelles, PEI étant amorphe et PPS semi-cristallin. Pour les mêmes formulations, le module de traction des composites PEI et PPS imprimés par FFF a été respectivement de 4.3 GPa et 6.0 GPa. Pour d'autres formulations, les différences mécaniques entre les pièces moulées par injection et celles imprimées par FFF étaient moins prononcées.

Pour mieux comprendre ces différences des propriétés mécaniques entre les pièces moulées par injection et celles imprimées par FFF, nous avons étudié l'évolution de la microstructure associée à chacun des procédés, c'est-à-dire pour l'IM et le FFF. Une corrélation a été faite entre les caractéristiques microstructurales et la performance mécanique, en utilisant des techniques de caractérisation telles que la microscopie électronique à balayage (MEB), la micro-tomographie à rayons X (micro-CT) et la calorimétrie différentielle à balayage (CDB). Ces techniques ont permis de quantifier le contenu en porosité, la distribution et l'alignement de la longueur des fibres, ainsi que la cristallinité des pièces moulées par injection et imprimées par FFF.

Il a été constaté que les pièces imprimées par FFF présentent une porosité allant jusqu'à 17 % pour les composites PEI et 9.2 % pour les composites PPS renforcés avec 20 % en poids de rCF, comparativement aux mêmes formulations de pièces moulées par injection qui ont présenté seulement ~ 1 % de porosité. De plus, les fibres dans les pièces moulées par injection sont plus longues et mieux alignées dans la direction de l'injection par rapport à celles des pièces FFF. Par ailleurs, les composites PPS moulés par injection présentent une cristallinité plus élevée que les composites PPS imprimés par FFF. Ces analyses quantitatives nous aident à mieux comprendre les différences de performances mécaniques entre les pièces moulées par injection et celles imprimées par FFF.

La performance mécanique des pièces structurelles plus complexes imprimées avec les composites développés, notamment des panneaux sandwich en configuration de nids d'abeilles, a également été évaluée. Ces panneaux ont été choisis en raison de leur utilisation répandue dans les intérieurs des avions, donc par leur application dans l'industrie aérospatiale. La performance mécanique en flexion des panneaux sandwich imprimés par FFF a été comparée à celle des panneaux imprimés avec des filaments composites PEI et PPS disponibles commercialement.

Un dispositif de corrélation d'image numérique 3D (DIC) est utilisé lors des tests de flexion, permettant une mesure de déformation en champ complet et mettant en évidence les zones de concentration de la déformation. Cette analyse a aidé à mieux comprendre les mécanismes de

fracture des panneaux sandwich imprimés par FFF sous charge de flexion. Dans l'ensemble, les panneaux sandwich imprimés en 3D ont démontré une capacité de charge significative allant jusqu'à 3.0 kN, avec un poids moyen d'environ 50 g. Les propriétés de flexion de ces panneaux sandwich imprimés avec des filaments de composites PEI et PPS se sont avérées comparables à celles des panneaux imprimés avec des filaments commerciaux.

Les nouvelles formulations de filaments composites de PEI et de PPS ont montré des propriétés mécaniques améliorées par rapport aux matrices pures moulées par injection, ainsi qu'une bonne imprimabilité dans les structures sandwich en nids d'abeille imprimés par FFF. Ces nouveaux composites ont prouvé un réel potentiel d'application dans l'industrie aérospatiale, en particulier pour des composants secondaires non structuraux dans les pièces intérieures, telles que les conduits d'air, les capots de sièges et les panneaux de sol ou muraux.

## ABSTRACT

Fused Filament Fabrication (FFF) of high temperature and high mechanical performance polymers offers considerable potential for the aerospace industry. This is due to the flexibility of FFF in creating complex structures, as well as the mechanical, thermal and flame-retardant properties of these polymers that are resistant to high temperatures. However, there are several challenges associated with the FFF of high-temperature polymers, particularly when reinforced with short fibers. These challenges include high-temperature processing, high viscosity, filament extrusion difficulties, porosity formation, the amorphous or semi-crystalline behaviour of the matrix, and the fiber-matrix interface, all of which can impact the final mechanical properties of the printed parts. Additionally, selecting a suitable polymer matrix and developing composites that meet the strict certification requirements of the aerospace industry is challenging. The relatively new FFF technology lacks standardized processes, and the properties of FFF-printed parts are still not fully understood when compared to those produced by conventional manufacturing techniques.

The work presented in this thesis proposes the development of different formulations of amorphous polyetherimide (PEI) and semi-crystalline polyphenylene sulfide (PPS) matrices, reinforced with recycled short carbon fiber (rCF) and thermal black (TB) particles. Four (4) different composite formulations were manufactured based on each matrix. Initially, the composites contained 20 wt.% rCF, which was gradually replaced with TB particles, by 5 wt.% increments. After their melt compounding, the composites were injection molded (IM) and, as well, were extruded to shape them in filaments. Then, the mechanical, thermal, and microstructural properties of FFF printed parts and those of IM parts were analysed and were compared.

The mechanical properties are investigated in terms of tensile, flexural, and impact performance. The incorporation of rCF significantly enhanced the mechanical properties of both PEI and PPS composites. The incorporation of 20 wt.% rCF increased the tensile modulus of the IM PEI matrix from 3.2 GPa to 6.2 GPa, while for the IM PPS, the tensile modulus increased from 3.5 GPa to 20 GPa. The reinforcement efficiency with rCF loading for IM specimens of PEI and PPS may be attributed to differences in their structural characteristic, as they are amorphous and semi-crystalline, respectively. For the same formulations, the tensile modulus of FFF printed PEI and PPS composites is found to be 4.3 GPa and 6.0 GPa, respectively. For other formulations, the mechanical differences between IM and FFF printed parts are less pronounced.

To better understand these mechanical performance differences between IM and FFF printed parts, the microstructure evolution was investigated in respect to the melt-process applied, e.g., to IM and FFF processing. A correlation was done between the microstructural characteristics and the mechanical performance using characterization techniques such as scanning electron microscopy (SEM), X-ray micro computed tomography (micro-CT), and differential scanning calorimetry (DSC). These techniques allowed us to quantify porosity content, fiber length distribution and alignment, as well as crystallinity in both IM and FFF printed parts.

It is found that FFF printed PEI and PPS composites reinforced with 20 wt.% rCF have a porosity content of up to 16.8 % and 9.2 %, respectively, when compared to the same formulations of IM parts which presented only  $\sim 1$  % of porosity. Additionally, the fibers in IM parts are longer and more aligned in the injection direction compared to those in FFF parts. The IM PPS composites exhibited higher crystallinity than FFF printed PPS composites. These quantitative analyses help to better understand the mechanical performance differences between IM and FFF printed parts.

The mechanical performance of FFF printed parts using the developed composites, e.g., of more complex structural parts such as honeycomb sandwich panels, was also evaluated. These panels were chosen due to their widespread use in the interiors of planes, therefore for their application in aerospace industry. The flexural mechanical performance of the FFF printed sandwich panels was compared to that of panels printed with commercial PEI and PPS composite filaments.

A 3D digital image correlation (DIC) setup is employed during flexural testing, enabling full-field strain measurement and highlighting areas of strain concentration. This analysis helped to better understand the fracture mechanisms of the FFF printed sandwich panels under flexural loading. Overall, the 3D printed sandwich panels demonstrated a significant load-bearing capacity of up to 3.0 kN, with an average weight of approximately 50 g. The flexural properties of the sandwich panels printed with developed composite filaments were found to be comparable to those printed with commercial filaments.

The novel formulations of PEI and PPS composites filaments have demonstrated improved mechanical properties compared to injection molded neat matrices and also a good printability in FFF printing of sandwich panels. These new developed composites proved a real potential of application in the aerospace industry, particularly for secondary non-structural components in interior parts such as air ducts, seat caps, and wall or floor panels.

## TABLE OF CONTENTS

DEDICATION .....	III
ACKNOWLEDGEMENTS .....	IV
RÉSUMÉ.....	V
ABSTRACT .....	VIII
TABLE OF CONTENTS .....	X
LIST OF TABLES .....	XIV
LIST OF FIGURES.....	XVII
LISTE OF SYMBOLS AND ABBREVIATIONS .....	XXIII
LIST OF APPENDICES .....	XXV
CHAPTER 1    INTRODUCTION.....	1
CHAPTER 2    LITERATURE REVIEW .....	5
2.1    Fused filament fabrication.....	5
2.2    Polymer composites .....	6
2.3    Composite filaments in FFF .....	8
2.3.1    Layer adhesion and crystallinity .....	8
2.3.2    Fiber content.....	11
2.3.3    Fiber length and alignment.....	13
2.3.4    Porosity.....	14
2.4    High-temperature thermoplastic polymers in FFF .....	16
2.4.1    PEI based filaments for FFF.....	17
2.4.2    PPS based filaments for FFF .....	21
2.5    Sandwich panel structures in aerospace applications.....	24
2.5.1    Using digital image correlation (DIC) for analysing mechanical testing of sandwich panels .....	28

CHAPTER 3	OBJECTIVES AND SCIENTIFIC CONTRIBUTIONS .....	31
3.1	Synthesis of the literature .....	31
3.2	Research objectives .....	33
3.3	Scientific contributions .....	34
CHAPTER 4	METHODOLOGY .....	36
4.1	Materials .....	36
4.2	Processing methods .....	36
4.2.1	Composite preparation and compounding .....	36
4.2.2	Injection molding (IM) .....	37
4.2.3	Filament extrusion .....	37
4.2.4	Fused filament fabrication (FFF) .....	38
CHAPTER 5	ARTICLE 1: FORMULATION AND CHARACTERIZATION OF POLYETHERIMIDE COMPOSITES REINFORCED WITH RECYCLED CARBON FIBERS AND THERMAL BLACK PARTICLES FOR FUSED FILAMENT FABRICATION .....	41
5.1	Abstract .....	41
5.2	Introduction .....	42
5.3	Materials and Methods .....	44
5.3.1	Materials .....	44
5.3.2	Methods .....	44
5.3.3	Characterization techniques .....	46
5.4	Results and Discussion .....	48
5.4.1	Microstructural characterization of the manufactured composites .....	48
5.4.2	Mechanical properties of IM and FFF printed PEI composite specimens .....	58
5.4.3	Thermal resistance of IM and FFF printed PEI composite specimens .....	61
5.5	Conclusion .....	62



CHAPTER 6	ARTICLE 2: CRYSTALLINITY, POROSITY, AND MICROSTRUCTURE OF POLYPHENYLENE SULFIDE COMPOSITE PARTS FABRICATED BY FILAMENT-EXTRUSION ADDITIVE MANUFACTURING .....	63
6.1	Abstract .....	63
6.2	Introduction .....	64
6.3	Materials and Methods .....	67
6.3.1	Materials.....	67
6.3.2	Melt-processing methods .....	67
6.3.3	Characterization methods .....	69
6.4	Results and Discussion.....	73
6.4.1	Crystallization kinetics of PPS and its composites .....	73
6.4.2	Microstructural characterization of PPS composites .....	81
6.4.3	Mechanical properties of IM and FFF printed PPS composites.....	88
6.5	FFF applied to high performance composites: current challenges vs. required improvements .....	90
6.6	Conclusion.....	91
CHAPTER 7	ARTICLE 3: FLEXURAL MECHANICAL PROPERTIES OF SANDWICH PANELS FABRICATED BY FILAMENT-EXTRUSION OF HIGH-TEMPERATURE THERMOPLASTIC COMPOSITES .....	93
7.1	Abstract .....	93
7.2	Introduction .....	94
7.3	Materials and Methods .....	96
7.3.1	Materials.....	96
7.3.2	Manufacturing of composite filaments .....	97
7.3.3	Characterization methods .....	99

7.4	Results and Discussion.....	102
7.4.1	Dimensional accuracy of FFF printed sandwich panels.....	102
7.4.2	Microstructure analysis of FFF printed sandwich panels.....	104
7.4.3	Full-field strain measurement during flexural testing .....	108
7.4.4	Flexural properties of FFF printed sandwich panels .....	109
7.5	Conclusion.....	113
CHAPTER 8	GENERAL DISCUSSION.....	115
CHAPTER 9	CONCLUSION AND RECOMMENDATIONS.....	119
REFERENCES	.....	122
APPENDICES	.....	132

## LIST OF TABLES

Table 2.1 Summary of literature studies comparing the effects of rCF and virgin CF on the flexural and tensile properties of FFF printed PEEK. ....	7
Table 2.2 Summary of 3D printing studies that have been done in the literature with different grades of PEI.....	20
Table 2.3 Summary of 3D printing studies presented in the literature by using PPS and its composites. ....	23
Table 2.4 Summary of studies that have been done for 3D printing of sandwich panel structures with commercially available filaments. Schematic of sandwich panels adopted from literature to provide better understanding of corresponding literature studies. ....	28
Table 4.1 Formulations of the extruded composites of PEI and PPS matrices by using a twin-screw extruder.....	37
Table 4.2 FFF printing parameters for PEI and PPS composite formulations were tailored by trial and error, with the trial range determined based on the technical data sheets of the neat PEI and PPS matrices. ....	40
Table 5.1. Formulations of the extruded composites using a twin-screw extruder.....	45
Table 5.2 Micro-CT analysis of FFF printed and IM PEI composites: quantitative values regarding porosity content and rCF length distribution and orientation. The average values are reported with CI of 95 % in the parentheses. ....	53
Table 5.3 Mechanical properties of injection molded and FFF printed PEI composites presented as mean values, and a CI of 95% is provided based on a sample size (n) of 5. ....	60
Table 6.1 Formulations of the extruded composites using a twin-screw extruder.....	68
Table 6.2 Crystallinity content during isothermal step ( $X_{c-iso}$ ), crystallization half-time ( $t_{1/2}$ ), Avrami's parameter ( $n$ ), and melting temperature ( $T_{m1}$ , $T_{m2}$ ) data obtained from the combination of isothermal and non-isothermal DSC procedure for each formulation. The $X_{c-iso}$ , $t_{1/2}$ , and $n$ , were computed from isothermal curves, while $T_{m1}$ and $T_{m2}$ were obtained from the data for heating cycle after isothermal steps. ....	79

Table 6.3 Heat enthalpy, crystallinity content, and melting temperature data obtained from the first heating DSC thermograms of the PPS composite samples for FFF printed and IM dogbone specimens. ....	81
Table 6.4 Micro-CT analysis results, along with the 95 % CI, on average rCF length, the corresponding aspect ratios, and rCF deviation angles of IM and FFF printed PPS composites. ....	86
Table 6.5 Mechanical performance of injection molded and FFF printed PPS composites. The results are presented as mean values and a CI of 95 %. ....	89
Table 7.1 Formulations of PEI and PPS based filaments from this work and of the commercial filaments. The CF content for commercial filaments is reported based on the manufacturer's technical datasheet. ....	97
Table 7.2 FFF printing parameters used for the sandwich panel printing of developed and commercial PEI and PPS composite filaments. ....	99
Table 7.3 Elastic modulus values used for the analytical calculation of sandwich panel properties for developed and commercial composite filaments. ....	102
Table 7.4 Mean distance values of C2M signed distance extracted from a comparison of the 3D scanned volume of the sandwich panel with respect to the CAD model, FWHM of peaks, average weight, and density of sandwich panels. The average values are reported with CI of 95 % in the parentheses. ....	104
Table 7.5 Quantitative values regarding average porosity content, including inter-layer porosity on the bottom and top skins, and the average dimensional length values, including bottom skins, top skins, and core wall thicknesses, were extracted from the processing of micro-CT images. The average values are reported with CI of 95 % in between parentheses. ....	108
Table 7.6 Mechanical properties comparison of sandwich panels including maximum load, flexural stiffness, maximum displacement, core shear modulus, and core shear strength as computed from the results of flexural testing results based on ASTM standards. The average values are reported with CI of 95 % in the parentheses. ....	113

Table B.1 Summary of flammability, smoke density, and smoke toxicity performance for FFF printed PEI and PPS composites after 20 min exposure of flame. This table presents the results of key fire safety performance indicators with their limits based on ASTM standards.....136

## LIST OF FIGURES

Figure 2.1 Schematics of the FFF extrusion process and key printing and material parameters [11].

(a) FFF printing method consisting of a filament spool system to feed filament and a liquefier for the melting and deposition of the extruded filament through the heated nozzle on the heated printing bed. (b) Main process, material, and printer parameters affecting the printing quality and ultimate mechanical performance of the FFF printed parts..... 6

Figure 2.2 Bond formation mechanism between adjacent filaments in the FFF process. (1) the contact between two adjacent filaments depends on the raster (deposited filament) gap in which negative (overlap) or zero air gap allow the physical contact of filaments of the same layer, (2) the neck formation is the result of filament contact and molecular diffusion of polymer chains toward each other, and (3) diffusion mechanism is the key parameter for layer adhesion and strongly depends on material microstructure (molecular weight, crystallinity, etc.) and temperature profile (cooling rate, printing bed, and chamber temperature, etc.) [29]. ..... 9

Figure 2.3 Micro-CT images of PETG filaments for porosity analysis. (a) *XY* cross-section of neat PETG filament, (b) *XY* cross-section of PETG filament reinforced with CF, (c) *XZ* cross-section in the length direction of a PETG filament reinforced with CF. Micro-CT analysis illustrates the effect of CF incorporation on porosity formation (labeled in yellow) in the composite filaments [47]. ..... 14

Figure 2.4 Micro-CT images of FFF printed CF reinforced ABS specimens. (a) inter-layer porosity highlighted in red, (b) inter-layer and intra-layer porosity and (c) higher resolution of intra-layer porosity [49]. The formation of inter-layer porosity in the printed specimens is due to the layer-by-layer deposition inherent in the FFF process, while carbon fiber incorporation leads to additional intra-layer porosity in the FFF printed specimens. .... 15

Figure 2.5 Complex viscosity versus angular frequency at various temperatures; (a) neat ULTEM 1000, (b) ULTEM 1000 with 20 wt.% CF, and (c) ULTEM 1000 with 30 wt.% CF. .... 19

Figure 2.6 Schematic of the composition of a sandwich panel and its final shape [82]. The honeycomb sandwich panel includes two face sheets, one hexagonal geometry core, and adhesive bonding of the core to the two face sheets. .... 24

Figure 2.7 The DIC images of sandwich panels, as adopted from the literature, provide a clearer understanding of the deformation and failure mechanisms under flexural loading. (a) The evolution of the displacement field in the  $Y$  direction illustrates the deformation behavior of the sandwich panel, where displacement increases as the load is applied. (b) The strain field in the  $X$  direction before fracture shows the distribution of tensile strain across the panel. As the flexural load increases, maximum deformation and tensile strain are concentrated in the lower half of the panel, eventually leading to failure. (c) The  $\epsilon_{xx}$  strain at the maximum load highlights the area of high tensile strain, which indicates that the face sheet of the sandwich panel fails due to excessive tensile stress. (d) The  $\epsilon_{xy}$  strains at maximum load show a high concentration of shear strain near the center of the core, particularly on the right-hand side, which is associated with core shear failure. This indicates that shear strain is responsible for core failure, complementing the tensile failure observed in the face sheet. These DIC images provide valuable insights into the failure modes of sandwich panels, including tensile failure in the face sheets and shear failure in the core. Figure 2.7.a-b adapted from [99], and 2.7.c-d adapted from [100]. ..... 30

Figure 4.1 Image of the setup for composite filament manufacturing that includes a high-temperature single screw extruder, followed by a cooling system, conveyor belt, laser-controlled diameter monitoring system, and a spooling system. .... 38

Figure 4.2 Schematic of specimens for mechanical testing, including sandwich panel, ASTM D638 (tensile test), ASTM D790 (flexural test), and ASTM D256 (impact test) geometries. The inset highlights the raster orientation of  $\pm 45^\circ$  used during FFF printing for all specimens. .... 40

Figure 5.1 Images of extruded composite filaments and of FFF printed ASTM specimens; (a) PEI composite filament spools (from left to right; rCF/TB (20/00), rCF/TB (15/05), and rCF/TB (10/10)), (b) FFF printed Type-1 dogbone specimens (ASTM D638) by using filament containing rCF/TB (20/00) for tensile testing, (c) Optical microscopy images showing details on FFF printed dogbone specimens' surface..... 46

Figure 5.2 Micro-CT analysis of PEI containing rCF/TB (20/00) composite filaments processed with the OpenFiberSeg tool: (a) reconstructed scanned volume, (b)  $XY$  cross-section of the composite filament, (c)  $XZ$  cross-section of the composite filament. .... 47

- Figure 5.3 (a) Isometric 3D view representing the composite filament volume with porosity projection onto axial planes. Micro-CT images of porosity density and their corresponding porosity content (b.1-d.1, and b.2-d.2), and plots of porosity size distribution (b.3-d.3) computed with a CI of 95 % for the composite filaments, (b.1-b.3) PEI/rCF/TB (80/20/00), (c.1-c.3) PEI/rCF/TB (80/15/05), (d.1-d.3) PEI/rCF/TB (80/10/10). ..... 50
- Figure 5.4 SEM images of the fracture surface of composite filaments: (a) PEI/rCF/TB (80/20/00), (b) PEI/rCF/TB (80/15/05), (c) PEI/rCF/TB (80/10/10), (d) PEI/rCF/TB (80/00/20). ..... 52
- Figure 5.5 Plots of rCF deviation angle distribution for developed composites; (a) IM and (b) FFF printed dogbone specimens. .... 54
- Figure 5.6 SEM images at three different magnifications of the fracture surfaces of the IM Izod impact specimens: (a.1-a3) PEI/rCF/TB (80/20/00), (b.1-b.3) PEI/rCF/TB (80/15/05), (c.1-c.3) PEI/rCF/TB (80/10/10), (d.1-d.3) PEI/rCF/TB (80/00/20). ..... 56
- Figure 5.7 SEM images of the fracture surface of FFF printed impact specimens: (a) PEI/rCF/TB (80/20/00), (b) PEI/rCF/TB (80/15/05), (c) PEI/rCF/TB (80/10/10), (d) PEI/rCF/TB (80/00/20). ..... 57
- Figure 5.8 Tensile properties of injection molded (solid bars) and FFF printed (patterned bars) composites, showing (a) tensile modulus (TM) and (b) tensile strength (TS) of the various specimens. The results are presented as mean values and a CI of 95 % is provided based on a sample size (n) of 5. .... 59
- Figure 6.1 Images of: (a) PPS composite filament spools (top: PPS/rCF/TB (80/20/00) and bottom: PPS/rCF/TB (80/10/10)), (b) FFF printing of a Type-1 dogbone specimen, (c) FFF printed Type-1 dogbone specimens using filament PPS/rCF /TB (80/20/00). ..... 68
- Figure 6.2 DSC plot illustrating the combination of isothermal and non-isothermal cycles applied to the studied PPS composites to observe their crystallization behaviors in thermal conditions variations mimicking the temperature variations met in FFF printing. .... 70
- Figure 6.3 Micro-CT procedure to assess porosity and fiber distribution for IM and FFF printed dogbone specimens: (a) inter-layer porosities were measured from scans of the entire cross-section of dogbone specimens, followed by higher resolution scans for intra-layer porosities. The porosities, matrix and fibers are highlighted with arrows. (b) rCF were tracked and labeled



- by using OpenFiberSeg software, allowing for the computation of fiber length distributions and deviation angles from the extrusion direction. .... 72
- Figure 6.4 Non-isothermal DSC curves of cooling and second heating cycle in which the heat flow is given with respect to increasing temperature (a) exothermic crystallization peaks during cooling, (b) endothermic melting peaks during second heating cycle. .... 75
- Figure 6.5 DSC plots from the combination of isothermal and non-isothermal DSC procedure show crystallization behavior of PPS/rCF/TB (80/20/00) for different isothermal conditions: (a) exothermic crystallization peaks during isothermal steps for different isothermal crystallization temperatures, (b) endothermic melting peaks during heating cycle after isothermal steps. .... 76
- Figure 6.6 SEM (a.1-d.1) and micro-CT (a.2-d.2) images of the fracture surface of PPS composite filaments used to determine the porosity level with a CI of 95 %. (a.1-a.2) PPS/rCF/TB (80/20/00), (b.1-b.2) PPS/rCF/TB (80/15/05), (c1.-c.2) PPS/rCF/TB (80/10/10), (d.1-d.2) PPS/rCF/TB (80/00/20). .... 82
- Figure 6.7 SEM images of the fracture surfaces (left column) and micro-CT images of FFF printed specimens (right column): (a) PPS/rCF/TB (80/20/00), (b) PPS/rCF/TB (80/15/05), (c) PPS/rCF/TB (80/10/10), and (d) PPS/rCF/TB (80/00/20). .... 85
- Figure 6.8 Plots of rCF of; (a) and (b) represent deviation angles that ranges from  $0^{\circ}$  to  $90^{\circ}$  with respect to their relative frequency for IM and FFF printed specimens, respectively; (c) and (d) the cumulative probability as a measure of fibers that have an angle less than or equal to a given values of  $0^{\circ}$  to  $90^{\circ}$ . .... 88
- Figure 7.1 Images of CAD design of sandwich panels and FFF printed sandwich panel specimens: (a) rendered images of sandwich panel CAD file with dimensional parameters, (b) FFF printed sandwich panel specimens and composite filament spool based on PEI/rCF/TB(80/10/10).99
- Figure 7.2 DIC image of FFF printed sandwich panel (PEI/rCF/TB (80/20/00) with spackle pattern and three-point bending test setup with support span distance and loading tool position on the specimen equidistant from the two end supports. .... 100
- Figure 7.3 The sandwich beam cross-section with the dimensional parameter for the calculation of the flexural mechanical properties. .... 102

Figure 7.4 3D images of the scanned surface of a sandwich panel made of PEI/rCF/TB (80/20/00) developed composite filament for measuring the dimensions and comparison dimensional accuracy: (a) rendered 3D scanned surface of sandwich panel, (b) 3D scanned surface of sandwich panel processed with a color map of C2M signed distance with respect to their CAD model, (c) C2M distance distribution for PEI composites, (d) C2M distance distribution for PPS composites. .... 104

Figure 7.5 Micro-CT images of FFF printed sandwich panel structure: (a) reconstructed 3D volume of sandwich panel made of PEI/rCF/TB(80/20/00), (b) top view cross-section of sandwich panel that shows hexagonal core, (c) side views of sandwich panels showing cross-sections of top skin, bottom skins, and core walls for sandwich panels printed with PEI/rCF/TB(80/20/00), and PPS/rCF/TB(80/20/00) composite filaments, respectively, (d) rendered image of segmented inter-layer porosity in the top and bottom skin of sandwich panel, respectively. .... 107

Figure 7.6 (a) DIC strain map of a sandwich panel printed with PEI/rCF/TB(80/20/00) prior to the application of the bending force in which the color scale indicates the magnitude of strain, (b) corresponding strain graph after applied bending force, showing the value of compression strain in the top skin and tensile strain in the bottom skin. .... 109

Figure 7.7 DIC analysis of three-point bending results of sandwich panel printed with PEI/rCF/TB (80/20/00) composite filament: (a) a series of DIC images showing the evolution of strain with respect to the applied load, (b) load-displacement curve showing the mechanical response of the sandwich panel during flexural testing. (c) DIC raw image for crack initiation, which is indicated by the yellow circle, (d) DIC image presenting the strain concentration at the core prior to the crack formation (e) post-mortem analysis of crack propagation in the sandwich panel core. .... 110

Figure 7.8 Force-displacement curves showing the mechanical response of the sandwich panels during flexural testing with images of failed specimens at maximum load showing the post-mortem analysis of crack propagation in the sandwich panels. .... 112

Figure 8.1 (a) Image of the recycled filament spool of PPS composites containing rCF/TB (10/10) that was recycled by mechanically grinding the previously tested mechanical specimens into pellet size. These pellets were then fed into a single-screw extruder, transforming them into

filaments suitable for FFF printing, (b) SEM images of the rCF revealed the presence of surface sizing, (c) the frequency sweep test for the PPS composites demonstrated that the incorporation of rCF and TB led to an increase in viscosity, which can impact the presence of porosity..... 116

Figure A.1 SEM and EDS characterization of rCF. (a) The image shows the surface morphology of rCF, highlighting the presence of residual sizing. (b) The image presents the EDS elemental mapping, indicating the distribution of carbon (C), nitrogen (N), oxygen (O), and fluorine (F) on the rCF surface.....132

Figure B.1 TGA graph of PEI and its composites: (a) non-isothermal, (b) isothermal heating for neat PEI under nitrogen and air atmospheres, (c) non-isothermal heating for PEI/rCF/TB (80/20/00), PEI/rCF/TB (80/10/10), and PEI/rCF/TB (80/00/20) composites. The results from both isothermal and non-isothermal TGA clearly demonstrate that the PEI composites exhibit a good thermal stability throughout the processing cycles involved.....134

Figure B.2 Images of FFF printed PEI/rCF/TB (80/20/00) and PPS/rCF/TB (80/20/00) composites before and after the 20-minute vertical burning test. The burned specimens showed no dripping and met the flammability criteria according to ASTM standards.....136

## LISTE OF SYMBOLS AND ABBREVIATIONS

ABS	Acrylonitrile butadiene styrene
BAAM	Big Area Additive Manufacturing
CAD	Computer aided design
CF	Virgin carbon fiber
CI	Confidence interval
C2M	Cloud-to-mesh
DIC	Digital image correlation
DSC	Differential scanning calorimetry
EDS	Energy Dispersive Spectroscopy
FAA	Federal Aviation Administration
FFF	Fused Filament Fabrication
FDM	Fused Deposition Modeling
FM	Flexural modulus
FS	Flexural strength
HDT	Heat deflection temperature
IM	Injection molding
IS	Impact strength
Micro-CT	X-ray micro-tomography
PA	Polyamide
PC	Polycarbonate
PE	Polyethylene
PEI	Polyetherimide
PEEK	Polyetheretherketone
PEKK	Polyetherketoneketone
PLA	Polylactic acid
PP	Polypropylene
PPS	Polyphenylene sulfide
PS	Polystyrene
rCF	Recycled carbon fiber
SEM	Scanning electron microscopy
TB	Thermal black

TM	Tensile modulus
TS	Tensile strength
$T_g$	Glass transition temperature
$T_c$	Temperature of crystallization
$T_m$	Melting temperature
$X_c$	The crystallinity content
3D	Three-dimensional

## LIST OF APPENDICES

APPENDIX A SEM AND EDS ANALYSIS OF RECYCLED CARBON FIBER SURFACE.....	132
APPENDIX B THERMAL STABILITY AND FLAME SMOKE TOXICITY PROPERTIES OF PEI AND PPS COMPOSITES.....	133
B.1 Thermal stability of PEI and its composites .....	133
B.2 Fire Safety Performance .....	134
B.2.1 Flammability.....	134
B.2.2 Smoke Density.....	134
B.2.3 Smoke Toxicity.....	135

## CHAPTER 1 INTRODUCTION

The global additive manufacturing (AM) market is projected to reach \$37 billion by 2029 [1]. This technology is widely used in prototyping, tooling, and other production fields. The market is dominated by a few commercial companies with closed-source printing technologies featuring printers and materials. Fused Filament Fabrication (FFF) is an open-source technology for processing thermoplastic filaments to manufacture complex three-dimensional (3D) structures. FFF technology also shares a significant market portion of 11.5 % within the additive manufacturing industry by 2024, mainly because it is open-source technology.

The FFF process could yield significant benefits to the aerospace field. For example, sandwich panel structures consist of two outer layers, called skins, with a lightweight core [2, 3]. These structures are usually made of dissimilar materials that are glued together. The manufacturing of sandwich panels requires therefore many steps. Moreover, the hollow core structures are usually periodic and offer little room for variations in their geometries. The FFF printing could be used to fabricate sandwich panels in a single step while offering full flexibility on the manufacturing of complex core geometries.

Aerospace applications have challenging environmental conditions such as high temperatures, oxidative and chemical exposures, combined with mechanical loading. For example, aluminium (Al) 7000 and 2000 series alloys are limited to maximum operating temperatures ranging from 90 °C to 175 °C, as temperatures above this range can induce over-aging in the Al alloys. Regarding oxidative and chemical environment, the exposure of moisture and hydraulic fluids can cause corrosion and hydrogen embrittlement in most metallic parts.

Thermoplastic polymers like Polyetherimide (PEI) and Polyphenylene sulfide (PPS) are adequate candidates for secondary (non-structural) application in aerospace interior parts owing to their mechanical performance, inherent flame retardancy, and chemical and UV resistance. PEI is an amorphous thermoplastic polymer that has a tensile strength of up to 110 MPa, a tensile modulus of 3.2 GPa, and a service temperature of up to 175 °C, for selected grades [4]. PPS is a semi-crystalline thermoplastic polymer that has a tensile strength of up to 90 MPa, a tensile modulus of 3.5 GPa, and a service temperature of up to 200 °C, for selected grades [5].

The bulk mechanical properties of pure PEI and PPS cannot meet, in a neat form, the demanded requirements for the aerospace industry to replace metals. For example, the stiffness of PEI is approximately 3.5 GPa, whereas Al has a stiffness of approximately 69 GPa, making Al approximately 20 times stiffer than PEI. However, when considering their specific properties relative to density, with PEI having a bulk density of approximately 1300 kg/m<sup>3</sup> and Al a density of 2700 kg/m<sup>3</sup>, the gap narrows. The specific stiffness of PEI becomes  $0.26 \times 10^{-2}$  GPa.m<sup>3</sup>/kg, while for Al it is  $2.5 \times 10^{-2}$  GPa.m<sup>3</sup>/kg. In terms of specific stiffness, Al is only approximately 10 times stiffer than neat PEI.

PEI and PPS, as neat matrices, still do not possess adequate specific mechanical properties compared to Al. To address this drawback, developing composites with the incorporation of fillers and implementing them for manufacturing of lighter geometric structures such as sandwich panels is a viable solution to compete with metallic parts. For example, incorporating carbon fibers can improve the mechanical properties of the polymer matrix. According to the technical datasheet of commercially available carbon fibers (CF)-reinforced polyetheretherketone (PEEK) filaments, the modulus of neat PEEK, which is approximately 4 GPa, increases with CF incorporation up to approximately 10 GPa for 3DXTech PEEK-20 % CF and 17 GPa for Tecafil™ Vx 30 % CF filaments, both with a density of approximately 1400 kg/m<sup>3</sup> [6, 7]. The specific stiffness of these filaments becomes  $0.7 \times 10^{-2}$  GPa.m<sup>3</sup>/kg and  $1.2 \times 10^{-2}$  GPa.m<sup>3</sup>/kg, respectively. This means that, in terms of specific stiffness, Al is now approximately 3.5 and 2 times stiffer than the CF-reinforced PEEK composites, respectively, while Al was approximately 8 times stiffer, when compared to neat PEEK. The sandwich panel geometry increases the strength to weight ratio thanks to their low-density cellular core. For example, a commercial Al honeycomb core with 4.8 mm cell size has approximately 400 kg/m<sup>3</sup> of density, while a honeycomb core made of aramid fiber impregnated with phenolic resin, known commercially as Nomex, with the same geometry has density of 48 kg/m<sup>3</sup>, which provides significant advantage of light core density. In this context, the flexibility of FFF could lead to optimized geometries of sandwich panels printed with developed PEI and PPS composite filaments that cannot be made with commercial Al or Nomex core.

Incorporating fibrous reinforcement into polymer matrix enhances mechanical performance and reduces the cost of final products since fillers are generally less expensive, when compared to neat matrix. However, developing composite materials introduces other problems, such as increased viscosity that significantly affects the processability during composite compounding, filament



extrusion, and FFF printing. Developing new thermoplastic composite materials involves multiple processing steps, including composite compounding, filament extrusion, and FFF printing, while each one requires significant know-how and expertise. It also necessitates careful material selection to ensure the materials can withstand repetitive thermal processing cycles. On the other hand, commercially available PEI and PPS filaments with standard diameter of 1.75 mm are limited to only few manufacturers and are more expensive, up to 10-fold, when compared to pellets counterparts. Moreover, commercially available carbon-reinforced PEI and PPS filaments are currently limited to a maximum content of 15 wt.% of short carbon fiber.

This study was a part of National Research Council Canada's (NRC) project named 3D Research Ecosystem for Additive Manufacturing of Thermoplastic Composites, 3DREAM. 3DREAM project proposed to develop high-performance thermoplastic composites and to adapt them to the existing open-source FFF technology. 3DREAM was an industrial R&D group, initiated by the NRC, where Polytechnique Montreal (Laboratory for Multiscale Mechanics (LM2)) was a collaborator. There were 15 partners in total, among which 13 were from the industry. The industrial partners were chosen by NRC to create a unique value chain for 3D printing of parts for transportation while using novel developed advanced composites. This collaboration includes, among others, the development of novel PEI and PPS composites reinforced with recycled carbon fibers (rCF) and thermal black (TB) particles and, as well, the advancement of the FFF printing process for the manufacturing of sandwich panel structures for the aerospace industry.

In this context, the main objectives of this thesis were the development and the comprehensive investigation of amorphous PEI and semi-crystalline PPS composites adapted for FFF printing of parts featuring significantly improved specific stiffness and strength, when compared to injection molded parts made from neat polymers. The methodology included the melt processing of composites and their comprehensive analysis in terms of rheological, thermal, microstructural, and mechanical characterization using advanced methods such as differential scanning calorimetry (DSC), X-ray microtomography (micro-CT), digital image correlation (DIC), 3D scanning, and scanning electron microscopy (SEM).

The main challenge for this work relied in the fabrication of a printable filament with a maximum reinforcement content, optimized at 20 wt.%, while reducing the presence of porosities and increasing the strength and toughness of FFF printed parts. The quality of printed parts needed to

be addressed by using advanced characterization methods applied to initial extruded composites and to the printed parts, both before and after testing, since the selection of printing parameters was challenging and involved machine calibration and many changes of FFF processing parameters. Moreover, the FFF technology is still not fully mastered and lacks of appropriate standard testing methods for the final printed parts, all combined to the high costs of high-performance thermoplastic polymers. The lack of standards for 3D printing technology and 3D printed parts and the existing strict safety regulations specific to the aerospace industry require a full understanding of the FFF printing process and the development of new materials to be able to compete with conventional manufacturing methods, such as injection molding.

This thesis consists of eight (9) chapters. Chapter 1 contains a short introduction on existing FFF 3D printing technology and its current challenges. Chapter 2 is the literature review that includes the main considerations for developing new polymer composite materials for FFF. It also reviews the literature on different types of polymers and emphasizes the need for developing novel high-temperature composite materials for FFF printing for aerospace interior applications. Chapter 3 analysis and identifies the gaps existing in the scientific literature to support the choices of the hypotheses at the basis of this thesis. Chapter 3 also defines the three specific objectives of this research project. Chapters 4 presents the methodology for composite processing including compounding, injection molding, filament extrusion and FFF printing. Chapters 5, 6, and 7 present the three research papers submitted to peer-reviewed scientific journals as part of this work, each corresponding to a specific objective. Chapter 8 is a general discussion that synthesizes all the results and the knowledge acquired from the previous chapters, correlating them with the hypotheses and objectives formulated at the beginning of the study. Chapter 9 encompasses the conclusions and the recommendations for potential future studies that would bring other scientific advancements for the development done in this work.

## CHAPTER 2 LITERATURE REVIEW

### 2.1 Fused filament fabrication

Fused filament fabrication (FFF) additive manufacturing uses thermoplastic filaments to build structures through the melting and computer-controlled deposition of thermoplastic polymers and their composites, layer-by-layer. The FFF is an open-source printing technology and the printing process could be freely modified, unlike the closed-source fused deposition modeling (FDM) technology. **Figure 2.1(a)** shows the schematic representation of the FFF process. The thermoplastic filament is fed into a heated nozzle through the feed system which usually consists of two pinch rollers and a stepper motor. The heated polymer is ejected onto the printed bed in the molten state, and then the deposited polymer starts to cool down and solidifies. The layers are built with the programmed movement of the printing head in  $X$ ,  $Y$  and  $Z$  coordinates to draw particular patterns which are designed with a computer aided design (CAD) and a slicing software.

Thermoplastic polymers commonly used as feedstocks for 3D printing are acrylonitrile butadiene styrene (ABS), polylactic acid (PLA), polyamide (PA), and polycarbonate (PC). Before using a material in FFF printing, the thermoplastic polymers or their composites containing reinforcing or filling components such as fibers or particles (when applicable) are first compounded together in an extrusion line and then converted, also by extrusion, into composite filaments featuring the desired diameter (e.g., 1.75 mm or 2.85 mm). The reinforcing or filling components and the polymer matrix should be compounded adequately and dried to attain a certain level of moisture below a critical one (specific to each thermoplastic polymer). Moreover, there are some other considerations during the transformation of compounded composite pellets in a filament such as filament dimensional tolerance (diameter and ovality), flexibility, porosity content, and melt viscosity [8].

The 3D printed parts usually have lower mechanical properties, when compared to injection and compression molded parts, mainly due to the presence of defects formed during the printing process, such as porosity, a weaker layers adhesion compared to bulk parts, etc. [9, 10]. **Figure 2.1(b)** summarizes studied key elements and main parameters that affect the FFF printing quality.

In terms of material parameters, the crystallinity, viscosity, and surface characteristics of polymers are mostly dependent on the temperature of the FFF printing. Material parameters dominate the flow behaviour of polymer through the nozzle and have a significant role in developing adhesion between printed layers. Raster angle and infill ratio are the other important printing parameters that lead to different mechanical performance and void contents across the material printing direction [9-11]. Raster angle is the deposition angle of deposited filament for each layer ranging from  $0^\circ$  to  $180^\circ$ . Infill ratio is the fill density regarding amount of material withing the printed part.

The FFF process offers flexibility and adaptability due to its open-source nature, which allows modifications to the printing parameters and materials to improve mechanical performance. Therefore, the careful selection of printing parameters and materials, as well as tailoring of each parameter, are essential to improve the performance of the final printed parts.

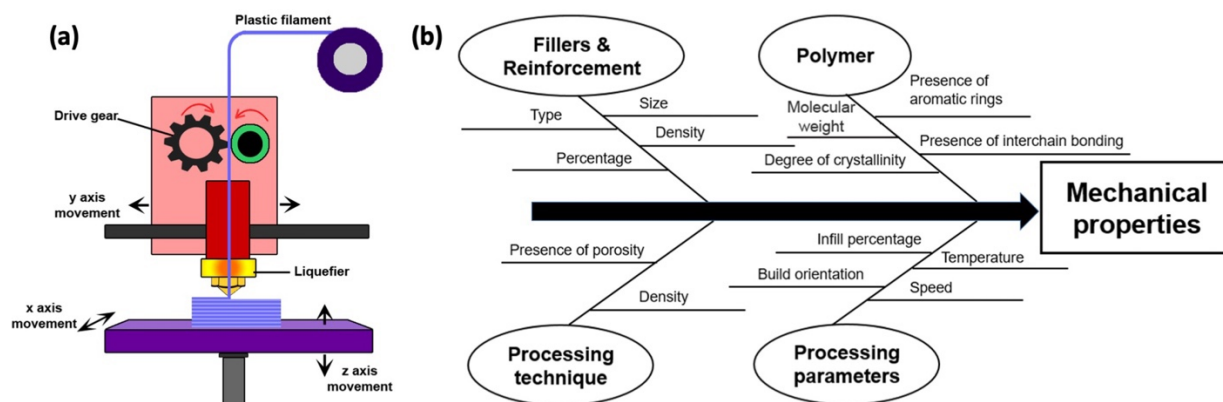


Figure 2.1 Schematics of the FFF extrusion process and key printing and material parameters [11]. (a) FFF printing method consisting of a filament spool system to feed filament and a liquefier for the melting and deposition of the extruded filament through the heated nozzle on the heated printing bed. (b) Main process, material, and printer parameters affecting the printing quality and ultimate mechanical performance of the FFF printed parts.

## 2.2 Polymer composites

The incorporation of fibers into a polymer matrix often enhances its mechanical and physical properties such as tensile, flexural and impact performance, thermal conductivity, electrical conductivity, etc. [12, 13]. Carbon fibers are widely used for applications in the aerospace industry. Polyacrylonitrile (PAN)-based high strength carbon fibers have a tensile strength of  $\sim 4.5$  GPa, a Young's modulus of  $\sim 230$  GPa, and a density of  $1.75\text{--}1.93$  g/cm<sup>3</sup> [14].

The recycling process of CF wastes to manufacture recycled carbon fibers (rCF) was reported to require roughly 5-10 % of the energy expenditure associated with the manufacturing of virgin CF [15, 16]. The mechanical properties of rCF are comparable to those of virgin CF while being more cost-effective. For example, the rCF could have a tensile modulus of 231 GPa, a tensile strength of 4.4 GPa and density of 1.78 g/cm<sup>3</sup>. The cost of rCF (~17 \$/kg) is approximately the third of that of virgin CF (~60 \$/kg). Similarly, it was reported that rCF costs 40 % lower and maintain at least 90 % of their tensile strength, when compared to virgin CF. For smaller production capacity of 100 t/yr, the rCF costs 15 \$/kg, but at production capacity of 500-6000 t/yr the market price of rCF could reduce down to 5 \$/kg [17, 18].

Very few studies focused on using rCF for developing FFF composite filaments as summarized in **Table 2.1**. For example, Huang et al. [19] reinforced polyether ether ketone (PEEK) matrix with 10 wt.% of rCF and compared the flexural mechanical properties with pure PEEK and PEEK reinforced with virgin CF. It was reported that with the incorporation 10 wt.% rCF, the flexural strength and modulus increased by ~ 10 % and 25 %, respectively, when compared to pure PEEK. In contrast, the addition of virgin CF improved the flexural strength and modulus by ~ 15 % and 30 %, respectively, over pure PEEK. Similarly, Liu et al. [20] developed PEEK composite filaments reinforced with 10 wt.% of rCF and compared the tensile properties with pure PEEK and PEEK reinforced 10 wt.% of virgin CF. It was reported that rCF reinforced PEEK exhibited 17 % and 23 % higher tensile strength and modulus, when compared to pure PEEK. Specimens printed with virgin CF reinforced PEEK exhibited 23 % and 31 % higher tensile strength and modulus, respectively, when compared to pure PEEK.

Table 2.1 Summary of literature studies comparing the effects of rCF and virgin CF on the flexural and tensile properties of FFF printed PEEK.

Study	Matrix	Reinforcement (wt.%)		Property measured	Improvement over pure PEEK (%)	
		rCF	Virgin CF		rCF	Virgin CF
Huang et al. [19]	PEEK	10	10	Flexural Strength	10	15
		10	10	Flexural Modulus	25	30
Liu et al. [20]	PEEK	10	10	Tensile Strength	17	23
		10	10	Tensile Modulus	23	31

Thermal black (TB) is a form of carbon black particles produced by the burning of natural gas, which results in a powder with contents of elemental metals < 0.5 ppm, sulphur < 10 ppm, and ash < 0.02 ppm [21]. The production of TB particles yields only hydrogen (H<sub>2</sub>) as a side product and

this is used for reheating the reactor and electricity generation. It has an average particle size of 280 nm. Unlike the furnace carbon black, TB is not electrically conductive (electrical volume resistivity of  $4.5 \times 10^7$  ohm.cm) due to its surface characteristics and amorphous structure [22]. The cost of TB (~2 \$/kg) is significantly lower than that of virgin carbon fiber (CF) (~60 \$/kg).

To the best of my knowledge, only two studies investigated the use of TB with polymer matrices. For example, Ziebell et al. [23] incorporated TB particles into ethylene propylene diene monomer (EPDM) rubber and the study showed that the addition of TB enhanced the processability by lowering the dynamic viscosity and storage modulus. In another study [24], the advantage of using TB and combination with TB and CF in terms of rheological and thermal properties improvement was demonstrated. For example, it was reported that the complex viscosity of PA6 reinforced up to 20 wt.% TB remained similar to neat PA6. Incorporating up to 20 wt.% of TB increased the heat deflection temperature (HDT) from 160 °C to 183 °C, while providing cost reduction up to 32 %, when compared to neat PA6. Moreover, the morphological characterization showed that the addition of TB enhanced the fiber-matrix adhesion as the surface of CF was completely covered by a mixture of matrix and TB in hybrid composites, when compared to composites reinforced by CF alone.

Thus, incorporating carbon fibers into a polymer matrix can improve its mechanical and thermal properties. The use of rCF offers a cost-effective and sustainable alternative to virgin carbon fibers. Using rCF in combination with TB to produce FFF filaments could yield to a cost-effective and energy-effective alternative to filaments made of virgin CF.

## **2.3 Composite filaments in FFF**

Surface characteristics and mechanical performance of 3D printed composite parts strongly depend on polymer matrix innate properties, layer adhesion, fiber content, porosity, and fiber-matrix interaction such as fibers distribution, aspect ratio, and fiber-matrix adhesion [10, 25].

### **2.3.1 Layer adhesion and crystallinity**

The adhesion between the layers of printed parts strongly depends on the bond formation during layers deposition that could affect the final mechanical performance of the printed parts [26]. The bond formation is a physical phenomenon driven by the diffusion of polymer chains through interfaces. This mechanism is significantly affected by the polymer's microstructure (semi-

crystalline or amorphous), crystallization kinetics, and cooling rate. **Figure 2.2** illustrates the steps of the bond formation mechanism between the extruded filaments which starts with the contact of filaments followed by the formation of the neck through molecular diffusion between layers. Layer adhesion depends on polymer molecular mobility, viscosity, thermal conductivity, and microstructure (e.g., semi-crystalline or amorphous). According to the reptation theory, which describes the thermal motion of polymer chains and diffusion mechanism for polymers, the lower cooling rates could provide greater mechanical strength for the printed part [27]. Moreover, the thermal conditions of printing and heat transfer phenomena during bond formation also affect the adhesion degree between layers. The interfacial bond continues to grow as polymer chains diffuse across the interface until temperature reduces below glass transition temperature, as described by the polymer healing model proposed by Wool et al [28].

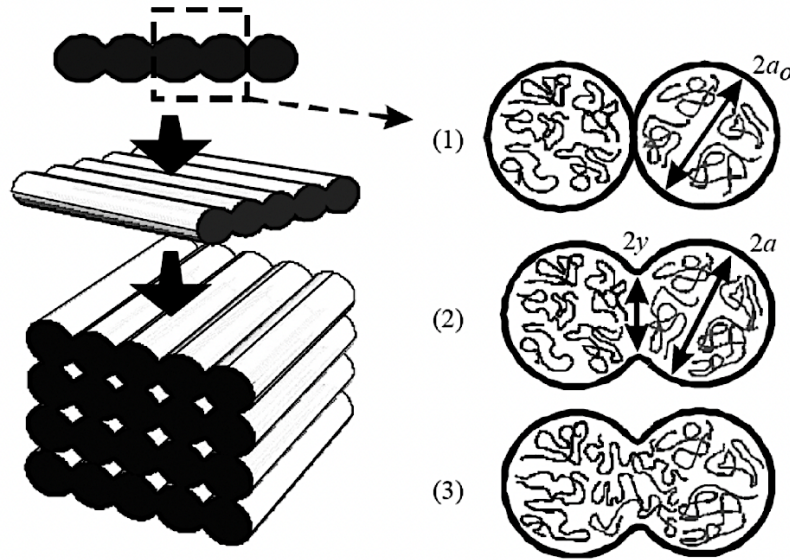


Figure 2.2 Bond formation mechanism between adjacent filaments in the FFF process. (1) the contact between two adjacent filaments depends on the raster (deposited filament) gap in which negative (overlap) or zero air gap allow the physical contact of filaments of the same layer, (2) the neck formation is the result of filament contact and molecular diffusion of polymer chains toward each other, and (3) diffusion mechanism is the key parameter for layer adhesion and strongly depends on material microstructure (molecular weight, crystallinity, etc.) and temperature profile (cooling rate, printing bed, and chamber temperature, etc.) [29].

The Newtonian sintering model for bonding quality prediction is given in equation (2.1) where  $t$ ,  $y$ ,  $a_0$ ,  $a$ ,  $\eta$ , and  $\Gamma$  represents time, neck length, initial particle radius, filament radius during necking, viscosity, and surface tension, respectively [29]. According to the equation 2.1, faster coalescence

rate occurs when the molecular weight ( $M_w$ ) or the viscosity of polymers is lower, regardless of semicrystalline and amorphous polymers.

$$\frac{d\theta}{dt} = \frac{\Gamma}{a_0\eta} \frac{2^{-\frac{5}{3}} \cos\theta \sin\theta (1 - \cos\theta)^{1/3}}{(1 - \cos\theta)(1 + \cos\theta)^{1/3}}, \quad \theta = \sin^{-1}(y/a) \quad (2.1)$$

The interlayer bonding mechanisms in FFF-printed polymers vary significantly between amorphous and semicrystalline materials due to their molecular characteristics, which influence polymer-polymer interdiffusion [30]. For amorphous polymers, the coalescence of adjacent filaments occurs primarily through viscous sintering, driven by surface tension and opposed by viscous forces. However, the time available for molecular diffusion during FFF is limited. Increasing temperatures can enhance filament fusion by improving molecular chain mobility. In semicrystalline polymers, bond formation is more challenging due to crystallization, which increases viscosity and inhibits neck growth as the material cools. It was observed that crystallization hinders molecular diffusion, and the interdiffusion length in semicrystalline polymers results in weaker bond strengths.

Collinson et al. [31] investigated the effect of crystallinity on layers adhesion for FFF printed PEEK. They printed specimens at chamber temperatures of 70 °C, 100 °C, and 130 °C which resulted in crystallinity content of 8 %, 8 %, and 32 %, respectively. The specimens printed at lower temperature resulted in a larger amorphous phase due to higher cooling rate and which resulted in higher mechanical properties, when compared to specimens printed at higher temperatures which had higher crystallinity. The authors explained this observation as a premature surface crystallization of PEEK depositions at higher temperatures that prevented the adhesion between printed layers, leading to a weak layer interface, which resulted in lower mechanical properties than expected.

Different layers adhesion enhancement methods have been reported in the literature such as annealing, printing parameter selection, in-situ local heating techniques, and matrix modification [32]. For example, Yang et al. [33] investigated the effect of annealing on the mechanical properties of FFF printed PEEK reinforced with 10 wt.% CF. It was reported that the crystallinity of specimens increased from ~ 21 % up to 36 % after annealing at 300 °C for 2 h. They reported that the tensile strength and tensile modulus of the specimens increased from ~ 50 MPa to 135 MPa and from 3.5 GPa to 9.2 GPa, respectively, owing to enhanced crystallinity after annealing.



Levenhagen et al. [34, 35] reported that the incorporation of low molecular weight ( $M_w$ ) additives could improve layer adhesion of FFF printed specimens, since these additives have higher diffusion ability due to higher molecular mobility. They synthesized PLA with different molecular weights and architectures and blended them with commercial PLA. The authors reported that blending 10 mol.% of low  $M_w$  PLA ( $M_w$  of 50 k) with commercial PLA ( $M_w$  of 220 k) increased the tensile stress and modulus by 66 % and 10 %, respectively, when compared to neat commercial PLA. Moreover, they investigated the effect of the architecture of Low  $M_w$  PLA with linear, 3-arms and 4-arms structures. The addition of 3 mol.% of 3-arm PLA exhibited optimum performance, with tensile stress and modulus increasing by 100 % and 36 %, respectively, when compared to neat commercial PLA.

Rostom et al. [36] reported that the incorporation of graphene nanoparticles in PLA matrix enhanced the inter-filament bonding quality due to improved thermal conductivity. They compared graphene loading contents of 0.5 %, 1 %, and 2 %. The only improvement was observed at 0.5 % graphene content, which enhanced thermal conductivity by ~ 15 %. This formulation exhibited 4 % porosity, while neat PLA had 11 % porosity. As a result, the tensile strength and modulus increased by 22 % and 30 %, respectively, when compared to neat PLA.

Therefore, enhancing adhesion between layers is key to improving mechanical performance. Layer adhesion is significantly affected by crystallinity and printing parameters. Studies also suggest that incorporating additives can enhance layers bonding by improving diffusion and thermal conductivity. Therefore, adjusting printing parameters by considering the microstructure of polymers and formulation is crucial for achieving stronger layers adhesion.

### **2.3.2 Fiber content**

A variety of short fibers reinforced composite filaments with different content and size have been developed for FFF [37]. Short fiber reinforced composites usually contain less than 50 wt.% loading, as increasing the fiber content adversely affects the processability and causes nozzle clogging [25]. Liao et al. [38] investigated the effect of different carbon fiber loadings (2, 4, 6, 8, and 10 wt.%) on the mechanical performance of a polyamide (PA) matrix. The tensile and flexural performance of the printed parts were enhanced by increasing CF loading while reducing the impact strength due to stress concentration at fiber ends resulting in crack initiation and propagation.

Zhong et al. [39] reinforced ABS with up to 30 wt.% of glass fibers. The authors observed that the extruded filaments could not be spooled and fed into the 3D printer due to brittleness resulting from the incorporation of glass fibers. Linear low-density polyethylene (LLDPE) plasticizer and hydrogenated Buna-N compatibilizer were used to eliminate this problem by enhancing the ductility and toughness of the composite structure. The authors found the optimum formulation for ABS containing 10 wt.% of LLDPE, 1 wt.% of compatibilizer, and a glass fiber content of 13-18 wt.%. The mechanical testing results showed an improvement in tensile properties compared to neat ABS. However, the incorporation of glass fibers reduced the adhesion strength between layers.

Diouf-Lewis et al. [40] developed composite filaments of PEEK/PEI blends with 30 wt.% CF content for FFF, where the CF ratio was fixed but the PEEK/PEI ratio gradually changed from 100/0 to 50/50. They reported that CF reinforcement increased the tensile modulus of the filaments up to 4-fold compared to their neat PEEK/PEI blends. However, they also observed that CF incorporation led to porosity formation. For instance, the PEEK/PEI (100/0) filament with 30 wt.% CF had a porosity of 3.9 %, while the PEEK/PEI (50/50) filament with the same CF content had a porosity of 19.7 %. The PEEK/PEI (100/0) and PEEK/PEI (50/50) filaments with 30 wt.% CF exhibited tensile modulus of 13 GPa, and 10.6 GPa, respectively, with the reduction in modulus attributed to the increase in porosity content.

Kishore et al. [41] investigated the rheological properties of carbon fiber reinforced polyphenylene sulfide (PPS) and polyetherketoneketone (PEKK) at different temperatures to determine the process condition and printability of these polymers. The zero-shear viscosity of PPS and PEKK increased by approximately 3 orders of magnitude at the incorporation of 40 wt.% of CF. Moreover, for PPS composites, it was reported that at CF incorporation the storage modulus became dominant, when compared to the loss modulus. The dominant elastic component is likely to cause cracks between the printed layers due to reduced layers adhesion and increased number of defects. This phenomenon was observed for CF reinforced PPS where the crack initiation appeared between deposited layers.

Increasing the fiber content could have a significant effect on the processability of composites and mechanical performance of the printed parts due to increased viscosity, porosity formation, and poor layers adhesion. Therefore, determining the optimum fiber content for a composite filament

is needed for facilitating the printing process and improving the mechanical performance of a polymer composite part.

### 2.3.3 Fiber length and alignment

The length of short fibers and their orientation in the matrix significantly affect the mechanical performance of the printed composite parts. For example, two grades of commercial composites of Acrylonitrile Styrene Acrylate (ASA) reinforced with 23 wt.% CF, having different average fiber length of 42  $\mu\text{m}$  and 96  $\mu\text{m}$ , were printed and their mechanical properties were compared. The printed specimens with longer fiber length exhibited 15 % and 66 % higher tensile strength and modulus, respectively, when compared to those with shorter fiber length [42]. Moreover, a commercial filament featuring 20 wt.% CF reinforced polyethylene terephthalate glycol (PETG) was used to investigate the effect of fiber alignment on mechanical properties. The commercial filament had an average fiber length of  $\sim 40 \mu\text{m}$  with a minimum aspect ratio of 3:1. The average fiber alignment were reported for the deviation with respect to extrusion direction along the toolpath. It was reported that specimens with an average fiber alignment of  $9^\circ$  in the extrusion direction exhibited 70 % and 117 % higher tensile strength and modulus, respectively, when compared to specimens with an average fiber alignment of  $\sim 30^\circ$  [43].

The shear stress applied to the melted matrix during the extrusion process leads to fiber breakage and the melt flow orientation due to elongational stresses presented in the nozzle leads to the alignment of fibers [37, 44]. Initially, long fibers are shortened in length due to shear forces created by screw rotation during the compounding in the extruder barrel. Its well-known that the fiber aspect ratio is an important parameter for the tensile mechanical performance of short fiber composites [45]. Inadequate fiber length distribution significantly decreases the load transfer between fiber and matrix, resulting in fiber pull-out instead of load-bearing. Werken et al. [25] reported that a fiber aspect ratio greater than 1000 is required to achieve 80 % of the theoretical effect on strength and modulus of a fiber reinforced composite.

The filament extrusion and printing processes have a relatively lower effect on fiber breakage, when compared to the compounding process. Tekinalp et al. [46] compared the fiber length distribution of printed and compression-molded ABS/CF specimens. It was reported that the initial fiber length of 3.2 mm was reduced to the average length of 0.4 mm during the compounding period due to high shear forces and interactions. Although there is a relatively lower shear rate in the FFF

method, the printing process further shortened the fiber length, especially with increasing fiber content, when compared to compression molded specimens.

The mechanical performance of FFF printed short fiber-reinforced composite is significantly influenced by the length and orientation of the fibers within the polymer matrix. Longer fibers and better alignment along the extrusion direction have been shown to enhance tensile strength and modulus. Therefore, managing fiber length distribution and alignment during the compounding and extrusion steps is crucial for improving the mechanical properties of printed composites.

### 2.3.4 Porosity

The carbon fiber incorporation generally leads to porosity formation in extruded filaments. For example, in **Figure 2.3**, commercial filaments of neat and 13 wt.% CF reinforced PETG were analyzed with micro-CT, where the resolution only allowed for the detection/visualisation of porosities, not individual fibers. It was reported that neat PETG filaments did not contain any porosity while CF reinforced PETG filaments had porosities occupying up to 15 % of their volume [47]. The porosities are labeled in yellow in the images of *XY* and *XZ* cross-section of filaments and were oriented in the *Z* flow direction. The source of porosity formation could be trapped air, inadequate wetting of fibers by the PETG matrix, and possible gases release during processing due to the degradation of fiber sizing.

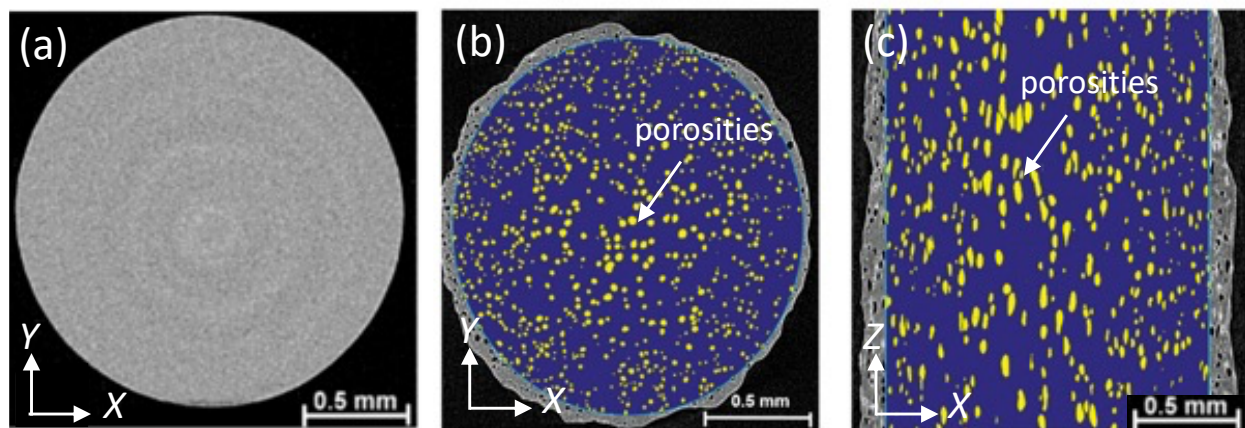


Figure 2.3 Micro-CT images of PETG filaments for porosity analysis. (a) *XY* cross-section of neat PETG filament, (b) *XY* cross-section of PETG filament reinforced with CF, (c) *XZ* cross-section in the length direction of a PETG filament reinforced with CF. Micro-CT analysis illustrates the effect of CF incorporation on porosity formation (labeled in yellow) in the composite filaments [47].

In the FFF process, the porosity can be classified in two types. The intra-layer porosity occurs in the extruded beads and the inter-layer porosity form between the layers of printed parts. For example, **Figure 2.4** shows the micro-CT images of FFF printed CF reinforced ABS composite specimens. As shown in **Figure 2.4(b)**, diamond shape inter-layer porosities are present between deposited layers, indicated in red. In contrast, **Figure 2.4(c)** shows that intra-layer porosities are randomly distributed within the extruded bead and are smaller in size ( $\sim 50 \mu\text{m}$ ), when compared to inter-layer porosity. Tekinalp et al. [46] reinforced ABS with varying CF content of 10-30 wt.%, and observed that with the increasing CF content the intra-layer porosity become dominant over inter-layer porosities, while total porosity fluctuates between 16 - 27 %. In another study [48], the porosity content of ULTEM 9085 and carbon fiber reinforced ULTEM 1000 were compared after the printing process of a compressor inlet guide vane. It was reported that porosity content ranged between 5 - 8 % for ULTEM 9085 which was mostly consisting of inter-layer porosity. Incorporating 10 wt.% carbon fiber in ULTEM 1000 increased the porosity content up to 25 % for the printed part, and both types of porosity, intra-layer and inter-layer, were observed.

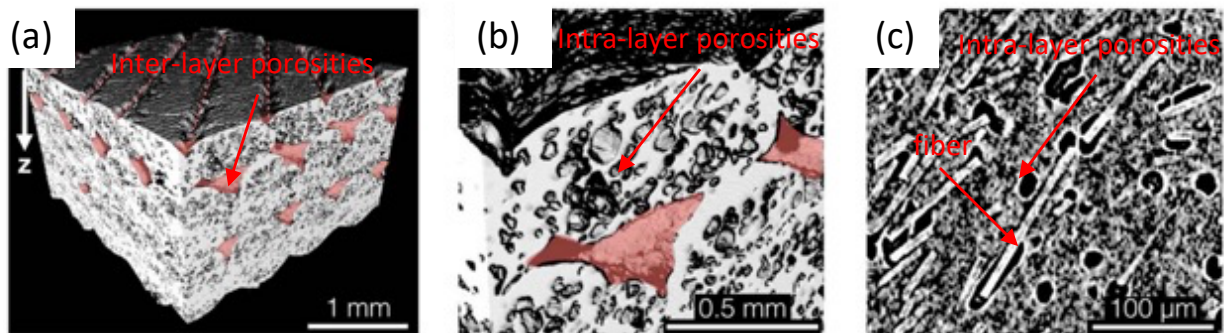


Figure 2.4 Micro-CT images of FFF printed CF reinforced ABS specimens. (a) inter-layer porosity highlighted in red, (b) inter-layer and intra-layer porosity and (c) higher resolution of intra-layer porosity [49]. The formation of inter-layer porosity in the printed specimens is due to the layer-by-layer deposition inherent in the FFF process, while carbon fiber incorporation leads to additional intra-layer porosity in the FFF printed specimens.

The presence of porosity could significantly reduce the mechanical properties of FFF printed parts. For example, Wang et al. [50] investigated the effect of porosity on the mechanical properties of FFF printed commercial PLA. Based on the different set of printing parameters, it was observed that the tensile modulus and strength of the FFF printed specimens reduced by  $\sim 15 \%$  and  $\sim 10 \%$  respectively, as porosity content increased from 4 % up to 6 %. The presence of porosity can result in weaker mechanical performance as pores affect adhesion and act as stress concentrations points.

To summarize, porosity is a significant factor that could affect the mechanical performance of parts produced by the FFF process. To mitigate porosity formation and enhance the mechanical performance of FFF printed parts, both fine tuning of material formulation and FFF processing parameters is needed. Understanding and quantifying porosity through experimental methods is crucial for fine-tuning of the mechanical behavior of FFF printed parts as it provides a quantifiable output that can be optimized.

## 2.4 High-temperature thermoplastic polymers in FFF

Thermoplastic polymers are made up of simple long chains that can be repetitively heated, melted, shaped, or welded without any significant change in their structure. Generally, thermoplastic polymers can be classified into three main categories which are commodity, engineering, and high-performance polymers based on their physical and mechanical properties. High-performance and high-temperature polymer terms are used interchangeably and defined differently depending their application, since their definition is evolving based on industry standards. In this work, "high-performance" refers to polymers with exceptional stability in harsh environments and superior properties over conventional ones. A widely accepted definition combines these attributes and includes: Flame, Smoke, and Toxicity (FST) compliance, thermal decomposition temperatures above 450°C, low weight loss rates at high temperatures (e.g., 0.05 wt.%/h at 450°C), high heat deflection temperatures (>177 °C), and high aromatic content with rigid, high  $T_g$  [51, 52].

Commodity polymers such as PLA is mainly used in 3D prototyping, while high-performance polymers like PEI, PPS, or PEEK are used for engineering applications such as interior parts in aerospace applications [53]. Moreover, polymers used in aerospace parts must meet the Federal Aviation Administration (FAA) regulations of FST [13, 53]. High-performance polymers have a high amount of double carbon (C=C) and aromatic bonds which enables their use at elevated temperatures, high pressure, and under a corrosive atmosphere [51, 54].

High-performance polymer families include polyimides, polysulfone, polyaryletherketones, and polyphenylsulfides [51]. These polymers exhibit amorphous or semi-crystalline structures. Amorphous high-temperature polymers such as polysulfones (PSU), polyetherimides (PEI), and polyphenylsulfone (PPSU) have clear optical properties, isotropic dimensional stability, relatively higher toughness, and impact strength, when compared to semi-crystalline polymer. Semi-crystalline high-temperature polymers such as PPS, PEEK, liquid crystal polymer (LCP),

polyetheretherketone (PEKK), polyphthalamide (PPA) have an opaque appearance, poor dimensional stability, and relatively higher chemical resistance compared to amorphous polymers.

PEI and PPS offer significant advantages for aerospace and transportation applications due to their inherent properties. For example, PEI offers ease of processability and high dimensional stability and toughness due to its amorphous structure. On the other hand, PPS has significant chemical resistance, when compared to other semi-crystalline high-performance polymers. Moreover, both PEI and PPS have relatively lower cost compared to high-performance polyaryletherketones, such as PEEK, making it a more cost-effective option for certain industrial applications while still offering robust properties. PEI and PPS are already used in aerospace and ground transportation applications, like interior of planes, parts for train exteriors and interiors, due to their inherent flame retardancy, low smoke emissions, and chemical resistance [4, 5].

FFF 3D printing technology applied to PEI and PPS polymers features many challenges due to their high processing temperatures (up to 390 °C or higher in the case of composites) and their high viscosity. The high thermal differences and fluctuations in the printing environment induce warping, distortion, or/and delamination, which significantly decrease the mechanical performance of the printed part. These challenges must be carefully managed to maintain the mechanical performance and integrity of final printed parts. Tailoring printing parameters and material formulations are essential to successfully adapt the behaviours of these high-melting temperature polymers and composites to FFF technology.

#### **2.4.1 PEI based filaments for FFF**

PEI, also known as ULTEM (SABIC's trademark for PEI resin), has a tensile strength of up to 110 MPa, a tensile modulus of 3.2 GPa, and a service temperature of up to 175 °C for selected grades. PEI has an amorphous structure which includes repeating units of ether and imide linkages. PEI has a glass transition temperature ( $T_g$ ) of approximately 210 °C. The aromatic imide units offer high thermal and mechanical performance, while the ether links in the molecular chain provide flexibility and melt processability. Therefore, PEI can be processed by melt extrusion, injection molding, and compression molding. Moreover, some grades of PEI have been verified to meet flammability requirements for the aerospace industry including FST tests. However, PEI also suffers from drawbacks such as high temperature and long time for drying it before processing due

to its hygroscopic structure. Weakness against chlorinated solvents and high cost are other PEI' drawbacks, when compared to semi-crystalline high-temperature polymers such as PEEK.

There are different commercially available grades of ULTEM; the ULTEM 1000 resin series are pure PEI grades with different melt flow rates such as ULTEM 1040A, ULTEM 1000, and ULTEM 1010. Grades from ULTEM 9000 resin series are blends of PEI and polycarbonate (PC), where the PC was used in low concentration to enhance the melt flow properties such as for ULTEM 9075 and ULTEM 9085 [4]. Some ULTEM grades are commercialized already in the shape of filaments, such as ULTEM 9085 and ULTEM 1010, while being very expensive when compared to conventional pellets. The current prices of these commercial filaments can be as high as 500 \$/kg [55], while the prices of corresponding commercial pellets are approximately ~ 60 \$/kg.

**Table 2.2** summarizes literature studies done on ULTEM based filaments used in FFF process. Different grades of commercial PEI filaments have been studied in the literature in terms of printing parameters and mechanical properties of printed parts. Studies on printing ULTEM 1010 mainly focus on optimization of the printing parameters and on the comparison of the mechanical properties of parts printed under different conditions [56-58]. Most of the studies focused on the commercial ULTEM 9085 filaments and investigated the effect of printing parameters such as printing direction, raster angle, and raster width, on mechanical properties [59-65].

Gebisa et al. [66] investigated the effect of printing parameters, such as the raster angle, raster width, raster air gap, contour width, and contour number on the mechanical properties of FFF printed ULTEM 9085 dogbone specimens. The mechanical results showed that raster angle is the most significant parameter affecting tensile properties; changing the raster angle from 90° to 0° increased the tensile strength from 30 MPa to 87 MPa, while the effects of other parameters remained minor. Similarly, Zaldivar et al. [60] studied the effect of raster angle and built direction on mechanical properties of FFF printed ULTEM 9085 dogbone specimens and compared them with those fabricated in injection molding. The specimens were printed in flatwise, edgewise, and 45° incline position with raster angle of 0° and 90°. It was found that specimens printed in the flatwise position and at 0° direction exhibited highest tensile properties and their tensile strength was equivalent to 85 % of that of the injection molded specimens.

Zaldivar et al. [61] investigated the effect of moisture content on the mechanical performance and porosity content of FFF printed specimens by using ULTEM 9085 filaments. Various moisture



concentrations (0, 0.05, 0.1, 0.16, 0.4, and 0.8 wt.%) were examined and it was found that porosity content in the printed specimens increased with moisture. For moisture content above 0.4 wt.%, porosity increased to over 45 %, corresponding to a reduction in tensile strength higher than 60 %.

Shelton et al. [63] investigated the effect of chamber temperature on the mechanical properties of FFF printed ULTEM 9085 specimens, with chamber temperatures ranging from 110 °C to 170 °C. It was reported that the tensile strength of specimens increased by 20 % as the chamber temperature increased from 110 °C to 170 °C.

Ajinjeru et al. [67] studied the rheological properties of commercially available ULTEM 1000 and its pellets reinforced with 20 wt.% and 30 wt.% of CF that were used for Big Area Additive Manufacturing (BAAM). **Figure 2.5** is showing that the addition of 20 wt.% and 30 wt.% of CF increased the complex viscosity by 150 % and 200 %, respectively, at frequency of 100 rad/s, when compared to neat ULTEM 1000. Moreover, increasing the temperature of testing from 365 °C to 400 °C reduced the complex viscosity by 51 %, 47 %, and 53 % for neat ULTEM 1000, and ULTEM 1000 containing 20 wt.% and 30 wt.% CF, respectively. Apart from increasing viscosity, they reported that CF incorporation provided shear thinning, when compared to neat ULTEM 1000. Neat ULTEM 1000 exhibited Newtonian like behaviour, where the loss modulus dominates over the storage modulus, making it fail or require longer times to retain their shape during the printing process, when compared to CF reinforced ULTEM 1000.

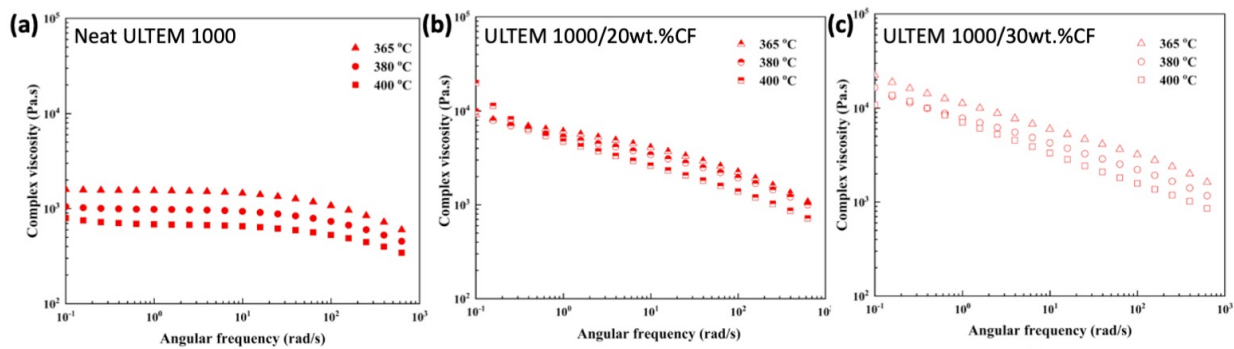


Figure 2.5 Complex viscosity versus angular frequency at various temperatures; (a) neat ULTEM 1000, (b) ULTEM 1000 with 20 wt.% CF, and (c) ULTEM 1000 with 30 wt.% CF.

Contrary to commercial PEI filaments, limited studies are available for developing custom PEI based composite filaments. For example, Chuang et al. [48] developed composite filament of carbon fiber reinforced ULTEM 1000 with 10 wt.% loading content and compared the mechanical properties with FFF printed neat ULTEM 1000, ULTEM 9085, and injection molded ULTEM

1000. The FFF printed ULTEM 1000 composite specimens showed a tensile mechanical performance of ~ 70 % of that ULTEM 9085 and ~ 50 % of an injection molded ULTEM 1000 due to the high porosity content, ~ 25 %, in the printed composites parts.

In another study, Slonov et al. [68] developed PEI based composite filament by modifying ULTEM 1010 matrix with oligophenylene sulfone (OPSU) and PC. Filament formulations of ULTEM 1010 containing of 25 wt.% CF with 20 wt.% of OPSU (CF/OPSU (25/20)) and 25 wt.% of CF with 20 wt.% of PC (CF/PC (25/20)) were manufactured. The mechanical performance of FFF printed specimens were compared with injection molded specimens. The FFF printed ULTEM 1010 composite containing CF/OPSU (25/20) exhibited 40 % of the tensile strength and 60 % of the tensile modulus compared at injection molded specimens. Similarly, the FFF printed ULTEM 1010 composite containing CF/PC (25/20) exhibited 48 % of the tensile strength and 35 % of the tensile modulus compared at the injection molded specimens.

Table 2.2 Summary of 3D printing studies that have been done in the literature with different grades of PEI.

Study	Material	Key parameters	Key results
Gebisa et al. [66]	ULTEM 9085	Raster angle	Tensile strength increased from 30 MPa to 87 MPa (90° to 0°)
Zaldivar et al. [60]	ULTEM 9085	Build direction, raster angle	Highest tensile strength at 85% of injection molded in flatwise, 0° position
Zaldivar et al. [61]	ULTEM 9085	Moisture content (0 to 0.8 wt.%)	>45% porosity and >60% reduction in tensile strength at 0.4 wt.% moisture
Shelton et al. [63]	ULTEM 9085	Chamber temperature (110 °C to 170 °C)	20% increase in tensile strength (110 °C to 170 °C)
Ajinjeru et al. [67]	ULTEM 1000 + 20 wt.% & 30 wt.% CF	Rheological properties at various temperatures	150% and 200% increase in viscosity (20 wt.% and 30 wt.% CF); 51% viscosity reduction (365 °C to 400 °C)
Chuang et al. [48]	ULTEM 1000 + 10 wt.% CF	Mechanical properties comparison	~70% tensile strength of FFF printed ULTEM 9085, ~50% of injection molded ULTEM 1000; with ~25% porosity
Slonov et al. [68]	ULTEM 1010 + 25 wt.% CF with OPSU/PC	Mechanical performance comparison	When compared to IM: CF/OPSU (25/20): 40% tensile strength, 60% modulus; CF/PC (25/20): 48% tensile strength, 35% modulus

Overall, PEI-based composites hold promise for high-performance application. While there is a significant body of literature on the use of commercially available PEI filaments for FFF, there are limited studies on developing novel PEI-based composite filaments. Mechanical performance of FFF printed PEI composites still does not match the mechanical properties of their injection molded counterparts. In this context, to fully harness PEI potential in FFF technology, new PEI composite

formulations are needed and ongoing challenges such as material cost, porosity, high viscosity, and the need for optimizing the printing parameters should be extensively studied.

## 2.4.2 PPS based filaments for FFF

PPS is a semi-crystalline thermoplastic polymer consisting of an aromatic ring connected to a sulphide atom that forms the basic unit of polymerization [69, 70]. There has been a growing interest in PPS due to its important mechanical performance, for example a tensile strength of 90 MPa and a tensile modulus of 3.5 GPa. The polymer's  $T_g$  is  $\sim 90$  °C while its melting temperature is  $\sim 280$  °C. Moreover, PPS is inherently flame retardant owing to its distinctive chemical configuration and its innate capacity to undergo charring upon exposure to an open flame [69].

There are three reported types of PPS including cured, linear, and branched. Each type has a different molecular weight, resulting in distinct mechanical properties. It is reported that linear PPS is suitable for injection molding applications due to its molecular chains length which provides adequate elongation and strength, while other types of PPS are mostly used for coating and films due to their thermal and chemical stability along with more ductile characteristics [69]. PPS is used in the injection molding of valves, high-pressure nozzles, fuel manifolds exterior light reflectors, coil bobbins, and flow measuring units, among many others [71].

**Table 2.3** summarizes the limited number of studies dealing with the FFF printing of neat PPS and carbon reinforced PPS composites. A search using keywords like polyphenylene sulfide, additive manufacturing, and carbon fiber yielded roughly 30 relevant studies in the scientific literature databases. The existing literature mainly studied commercial PPS filaments and pellets to investigate the effect of printing parameters on the mechanical properties of printed parts [72-75]. For example, Geng et al. [73] used a design of experiment to study the effects of various parameters, including extrusion multiplier, raster gap, outline overlap, infill angle, number of outlines, layer thickness fingerprint on the tensile, bending, and impact properties of FFF printed PPS specimens. The most significant parameters affecting the mechanical properties with contribution rate were reported with respect to each other. The raster gap, contributing at 46 % to tensile strengths and 43 % to bending strength was deemed to be the most important parameter, when compared to the other parameters. The extrusion multiplier was proved to affect tensile strength with a contribution of 31 % and bending strength with a contribution of 25 %. For impact strength, outline overlap was the most important parameter, contributing at a level of 51 %.

Garmabi et al. [72] investigated the effect of printing temperature, chamber temperature, and layer height on the mechanical properties and inter-layer bonding of FFF printed parts using commercial neat PPS filaments. They reported that increasing nozzle temperature from 310 °C to 340 °C reduced the viscosity by 50 %, making it the most effective parameter for inter-layer adhesion enhancement. Using optimized printing parameters, the tensile strength and tensile modulus of FFF printed specimens reached 93 % and 96 % from those of compression molded specimens.

Similarly, Magri et al. [76] investigated the effect of different printing temperatures (320, 330, 340, and 350 °C) on the crystallinity and mechanical properties of PPS. It was found that the crystallinity of printed specimens increased from 23 % to 37.3 % with increasing temperature up to 340 °C, but decreased to 33.6 % at a temperature of 350 °C. Similarly, the tensile modulus slightly increased from 1910 MPa to 2030 MPa with increasing temperature up to 340 °C, but decreased to 1980 MPa at 350 °C. The reason is that increasing the temperature promotes crystallinity by creating highly ordered lamellae during printing, while temperatures close to degradation lead to chain breakage, resulting in lower crystallinity and reduced mechanical properties.

Geng et al. [77] investigated the effect of a heat treatment on the mechanical properties of FFF printed neat PPS filaments. The FFF printed specimens were heat-treated for 100 min at temperatures of 130 °C, 150 °C, 200 °C, and 240 °C. The crystallinity content of FFF printed specimens increased from 19 % up to 64 % with increasing the post-processing treatment temperature, when compared to untreated specimens. The tensile properties also were improved as a function of the temperature of the heat treatment, with specimens treated at 240 °C exhibiting ~ 2-fold higher tensile strength, when compared to untreated specimens. However, the increased crystallinity significantly reduced the impact properties, as the impact strength dropped from 17 kJ/m<sup>2</sup> in untreated specimens down to 2 kJ/m<sup>2</sup> in those heat-treated at 240 °C.

Similarly, Kishore et al. [78] studied the effect of post processing on the crystallization and dynamic mechanical properties of printed commercial neat PPS and PPS containing 40-60 wt.% of CF used in a BAAM 3D printing technology. The printed specimens were submitted at a post-treatment at 250 °C for 18 h. The heat treatment increased the crystallinity by 37 % for neat PPS, by 55 % for PPS containing 40 wt.% CF, by 96 % for PPS containing 50 wt.% CF, and by 20 % for PPS containing 60 wt.% CF. The storage modulus of heat-treated specimens increased by 150

%, 124 %, 60 %, and 115 %, for neat PPS and PPS containing 40 wt.%, 50 wt.%, and 60 wt.% of CF, respectively, when compared to untreated specimens.

Fitzharris et al. [79] investigated the effect of post-processing on the inter-layers adhesion and mechanical properties of 3D printed neat PPS filaments. The optimal post-processing parameters, based on the design of the experiment, were found to be for a printing temperature of 300 °C, a 24-hour heat treatment, and a heat treatment temperature of 180 °C. It was found that, for the same printing conditions, heat-treated specimens at 180 °C had a tensile strength of 60 MPa, a tensile modulus of 2.3 GPa, and 48.4 % crystallinity, while specimens that were not heat treated had a tensile strength of 50 MPa, a tensile modulus of 1.8 GPa, and 25.7 % crystallinity. They compared the mechanical properties of printed specimens with compression-molded specimens, which had a crystallinity of 51 %. They reported that the heat treatment of the 3D printed specimens allowed to reach 80 % of the tensile strength and 72 % of the tensile modulus of the compression-molded PPS specimens.

Yeole et al. [80] studied the additive manufacturing of PPS composites using commercially available composite pellets containing 50 wt.% of CF. They processed the pellets into filaments for their use in BAAM and compared the evaluated mechanical properties with those obtained for IM parts. It was reported that the printed composites exhibited 45 % of the tensile strength and 63 % of the tensile modulus of the IM composites. The lower mechanical properties were attributed to the high porosity content, up to 15.5 % in the printed parts, and to a better alignment of CF in the IM parts.

Table 2.3 Summary of 3D printing studies presented in the literature by using PPS and its composites.

Study	Material	Key parameters	Key results
Geng et al. [73]	PPS	Printing parameters (raster gap, extrusion multiplier)	Raster gap contributed 46 % to tensile strength (TS) and 43 % to bending strength. Extrusion multiplier contributed 31 % to TS.
Garmabi et al. [72]	PPS	Nozzle temp (310°C to 340°C), layer height	With increased nozzle temp. viscosity reduced by 50 %; TS and tensile modulus (TM) reached 93%/96% of compression molded parts.
Magri et al. [76]	PPS	Printing temperature (320°C to 350°C)	Crystallinity increased from 23 % to 37.3 % at 340°C, TM from 1.9 GPa to 2.0 GPa.
Geng et al. [77]	PPS	Heat treatment (130°C to 240°C)	Crystallinity increased from 19 % to 64 %; TS 2-fold higher at 240°C; impact strength dropped from 17 kJ/m <sup>2</sup> to 2 kJ/m <sup>2</sup> .

Kishore et al. [78]	PPS + 40-60 wt.% CF	Heat treatment at 250°C for 18h	Crystallinity increased by 37 % -9 6 %; storage modulus increased from 60 % up to 150 % based on CF content.
Fitzharris et al. [79]	PPS	Post-processing, heat treatment (180°C)	Heat-treated specimens had 60 MPa TS, 2.3 GPa TM, 48.4 % crystallinity, reaching 80 %/72 % of compression molded properties.
Yeole et al. [80]	PPS + 50 wt.% CF	Composite pellets in BAAM	Printed composites had 45 % of TS and 63 % of TM compared to IM parts due to 15.5 % porosity.

Therefore, various factors such as printing parameters, temperatures of the post-processing treatments, and the CF reinforcement significantly affect the crystallinity, porosity content, and mechanical properties of PPS. Optimizing these variables could enhance the performance of FFF printed PPS composites. The literature highlights the importance of fine-tuning printing parameters and post-processing temperatures to maximize the mechanical properties of the semi-crystalline PPS and its composites.

## 2.5 Sandwich panel structures in aerospace applications

**Figure 2.6** shows the sandwich panel structures that consist of two outer layers (skin) and lightweight core structures [81]. Similar to I-beam structures, the skins of sandwich panels act as flanges while the core acts as the web. The incorporation of a core between two skin plates increases the stiffness of the structure by enhancing the moment of inertia. When submitted to flexural loads, the skins are mostly loaded uniaxially while the core is submitted to shear stresses.

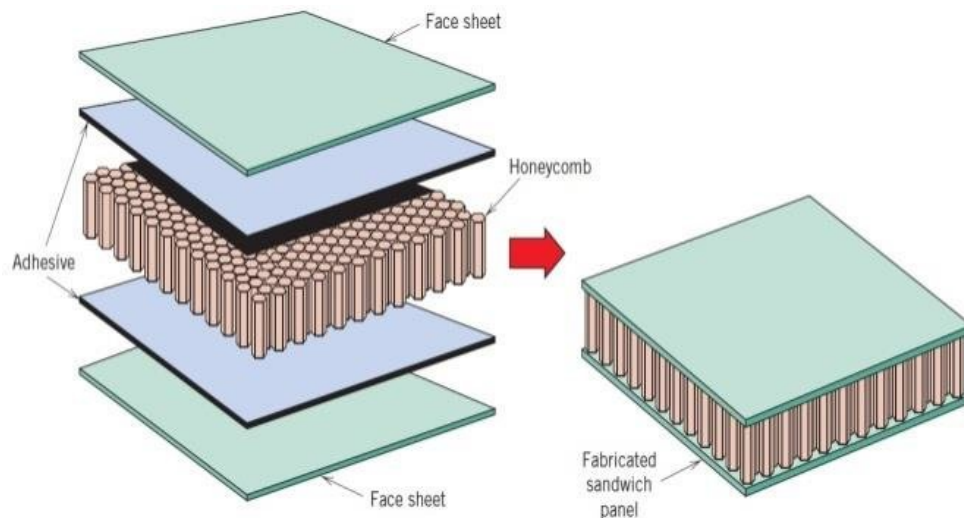


Figure 2.6 Schematic of the composition of a sandwich panel and its final shape [82]. The honeycomb sandwich panel includes two face sheets, one hexagonal geometry core, and adhesive bonding of the core to the two face sheets.

The most commonly used core types are corrugated, honeycomb, balsa wood, and cellular foams. Honeycomb cores, primarily used in aerospace applications, can be manufactured with different cell types. A common type of honeycomb for aerospace applications is made of aramid fiber impregnated with phenolic resin, known commercially as Nomex. Nomex is widely used because its mechanical properties are comparable to those of Al honeycombs. Nomex honeycomb can be used up to 180 °C. It has been reported that Nomex cores with a cell density of 129 kg/m<sup>3</sup> have a shear modulus of 112 MPa and 64 MPa and a core shear strength of 3.2 MPa and 1.7 MPa in the longitudinal and lateral directions, respectively [83].

The core-to-skin adhesive in sandwich panels is a critical component as it can lead to failure of the sandwich panel structure. Failure modes in sandwich panels include skin fracture or yielding, core shear failure, face wrinkling, buckling, and local indentation [84].

Sandwich structures are utilized in both primary and secondary applications in interior parts for aircraft applications. Carbon/epoxy and Nomex are mostly used in primary applications because of their reliability. Al honeycomb/boron-epoxy skin were used in secondary non-structural applications like interior parts, sidewalls, baggage racks, galleys, flooring, spoilers, rudders, ailerons, and flaps [85, 86].

The conventional production of thermoplastic composite sandwich panel structures includes separate manufacturing of skins (e.g., laminates, prepreg) and core structures (e.g., tube extrusion, hot press, ThermHex concept), and subsequently joining the skins to the core structures with adhesive or by fusion bonding methods [2, 3]. The current manufacturing method of sandwich structures manifests significant challenges due to the difficulty of the fabrication of a wide variety of shapes, of hollow configurations, and due to the critical adhesions between the cores and the face sheets. The thermoset-based sandwich panels production is also labor and time intensive and has as disadvantages a lack of the environmental sustainability due to poor recyclability of the thermoset-based parts. Moreover, joining the skins to the cores presents challenges, as it requires careful cleaning of their surfaces to remove potential contamination, release agents, machine oils, etc. Additional surface treatments could be applied as well in order to achieve adequate chemical bonds between cores and skins. Contrary, the FFF additive manufacturing technology using thermoplastic polymers and composites enables the fabrication of these complex structures in a

single step while permitting a higher flexibility in the core's design and offering a more sustainable environmental solution since the thermoplastics can be recycled.

**Table 2.4** presents literature studies for 3D printing of sandwich panels. The literature studies regarding FFF printing of sandwich panels mostly focused on the mechanical performance of sandwich panels with different core designs by using commercial filaments. PLA or ABS were extensively used to print sandwich panel structures for process optimization, modelling, and for investigating the effect of core structure on the mechanical properties [87-91]. For example, Castro et al. [92] investigated the mechanical properties of printed PLA sandwich panels with different core types, including out-of-plane and in-plane hexagonal honeycomb core structures (**Table 2.4**). It was reported that the out-of-plane honeycomb sandwich panels exhibited 29 % and 55 % higher flexural modulus and strength, respectively, when compared to in-plane honeycomb cores.

Essassi et al [93] used a commercial PLA reinforced with flax fiber to print sandwich panels with auxetic structure and different core densities (**Table 2.4**). They investigated the bending behaviour with cyclic loading. Sandwich panels were printed with four different core densities of 8.3 %, 16.7 %, 25.1 %, and 33.5 %, respectively. It was found that the failure load increased from 184 N up to 276 N as core density increased. However, the fatigue resistance of sandwich panels was reduced with increasing core density. The panel with 8.3% core density withstood five times more loading cycles under 65 % of the maximum applied load, when compared to the panel with 33.5% core density.

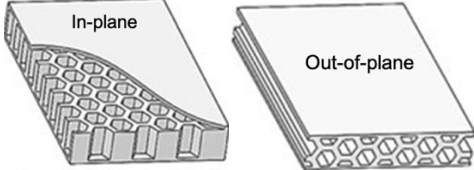
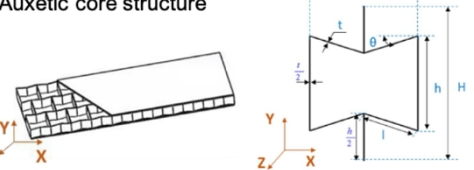
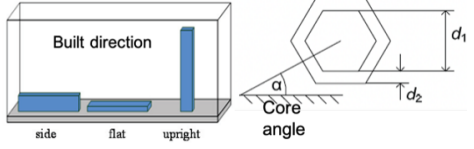
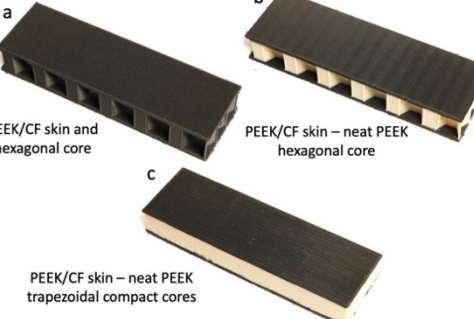
Few studies use high-temperature polymers for FFF printing of sandwich panel applications. For example, commercial ULTEM 9085 was used to predict the mechanical properties of honeycomb structures through analytical and numerical models [94]. In another study, Bagsik et al. [95] studied the effect of building direction of side, flat, upright (**Table 2.4**) and core angle of 0°, 90° and 45° on the mechanical properties of sandwich panels printed with ULTEM 9085 filaments. The specimens printed on the side and flat positions showed similar bending stresses (60–75 MPa), which were higher than those printed upright (25–35 MPa), regardless of core angle. Panels with a 0° core angle showed relatively higher bending stress compared to core with angles of 90° and 45°.

Pierre et al. [96] compared the flexural properties of sandwich panels with different core designs and materials using commercial neat PEEK and PEEK reinforced with 30 wt.% carbon fibers (CF). The study included panels with honeycomb cores made entirely from PEEK/CF and others with



hexagonal honeycomb and trapezoidal compact cores printed from neat PEEK, while the skins were printed with PEEK/CF. Results indicated that sandwich panels with PEEK/CF skins and neat PEEK cores showed notable improvements in flexural stiffness. Specifically, panels with hexagonal honeycomb cores demonstrated an 18 % increase in stiffness, and those with trapezoidal compact cores showed a 66 % increase, compared to panels printed entirely from PEEK/CF.

Table 2.4 Summary of studies that have been done for 3D printing of sandwich panel structures with commercially available filaments. Schematic of sandwich panels adopted from literature to provide better understanding of corresponding literature studies.

Material	Figures of parameters	Key results
PLA [92]	 <p>In-plane</p> <p>Out-of-plane</p>	Out-of-plane honeycomb cores exhibited 29 % higher flexural modulus and 55 % higher strength compared to in-plane cores.
PLA + Flax Fiber [93]	 <p>Auxetic core structure</p> <p>Y, Z, X axes</p> <p>t, <math>\theta</math>, h, H, l</p>	Failure load increased from 184 N to 276 N as core density rose from 8.3 % to 33.5 %; panel with 8.3 % core density withstood 5x more loading cycles.
ULTEM 9085 [95]	 <p>Built direction</p> <p>side, flat, upright</p> <p>Core angle</p> <p><math>d_1</math>, <math>d_2</math>, <math>\alpha</math></p>	Bending stress was higher for side/flat printed specimens (60–75 MPa) compared to upright (25–35 MPa); 0° core angle panels showed higher bending stress than 90° and 45°.
PEEK, PEEK + 30 wt.% CF [96]	 <p>a</p> <p>PEEK/CF skin and hexagonal core</p> <p>b</p> <p>PEEK/CF skin – neat PEEK hexagonal core</p> <p>c</p> <p>PEEK/CF skin – neat PEEK trapezoidal compact cores</p>	PEEK/CF skins with neat PEEK cores: 18 % higher flexural stiffness for hexagonal cores, 66 % higher for Trapezoidal Compact cores, compared to all-PEEK/CF panels.

The literature studies suggest that there is an advantage of using FFF technology for manufacturing of parts having complex designs and structures. Studies on FFF printed sandwich panels primarily focus on understanding how core structures and printing parameters would influence mechanical performance. Commercial commodity polymers are commonly studied. There is limited research on high-temperature polymers like PEI and PPS and their composites used in FFF of sandwich panels.

### 2.5.1 Using digital image correlation (DIC) for analysing mechanical testing of sandwich panels

DIC is an optical contactless measuring technique, that presents significant advantage over other methods that use extensometers or strain gauges, for full field strain measurement. The complex

geometries like sandwich panels can be analyzed with this technique since this method is not depending on the sample geometry. The use of DIC for sandwich panels testing can give significant information regarding core and skin deformations during testing which help to understand their type of failure mechanism [97].

Few studies investigated the failure mechanism of sandwich panels by using DIC system. For example, Ogasawara et al. [98] used a DIC system to investigate the failure mechanism of sandwich panels with a Nomex core and carbon fiber reinforced skins. They detected three failure modes during flexural loading: outward local buckling at the specimen center, and inward and outward buckling at the edges. These buckling failures caused core-skin debonding, crack propagation, and final failure of the sandwich panels. More than 80 % of specimens showed failure initiation at the specimen edge.

The **Figure 2.7(a-b)** presents images from Zhang [99] et al. study on the flexural properties of FFF printed PLA sandwich panels with variable core density by using DIC. They found that maximum tensile strain occurred in the lower half of the sandwich panels, leading to crack initiation in the lower face sheet, followed by core and upper face sheet fractures. Similarly, as shown in **Figure 2.7(c-d)**, Edelen et al. [100] used DIC system to examine the effect of process parameters on the mechanical response of printed ABS and PC sandwich panels for prediction of failure modes. Their study detected different failure modes, such as axial tensile strain accumulation in the lower face sheet, indicative of face sheet failure, and shear strain accumulation in the core, signaling core failure.

Therefore, DIC is very useful for investigating failure modes and sandwich panels and demonstrated that failure usually initiate at weak bonding points between core and skin in sandwich panels. DIC was used for understanding deformation in both the core and skin of sandwich panels, which is essential for diagnosing failure modes. Various studies have demonstrated how DIC can reveal key failure mechanisms such as buckling, core-skin debonding, and crack propagation in different materials, helping to improve the design and optimization of these structures.

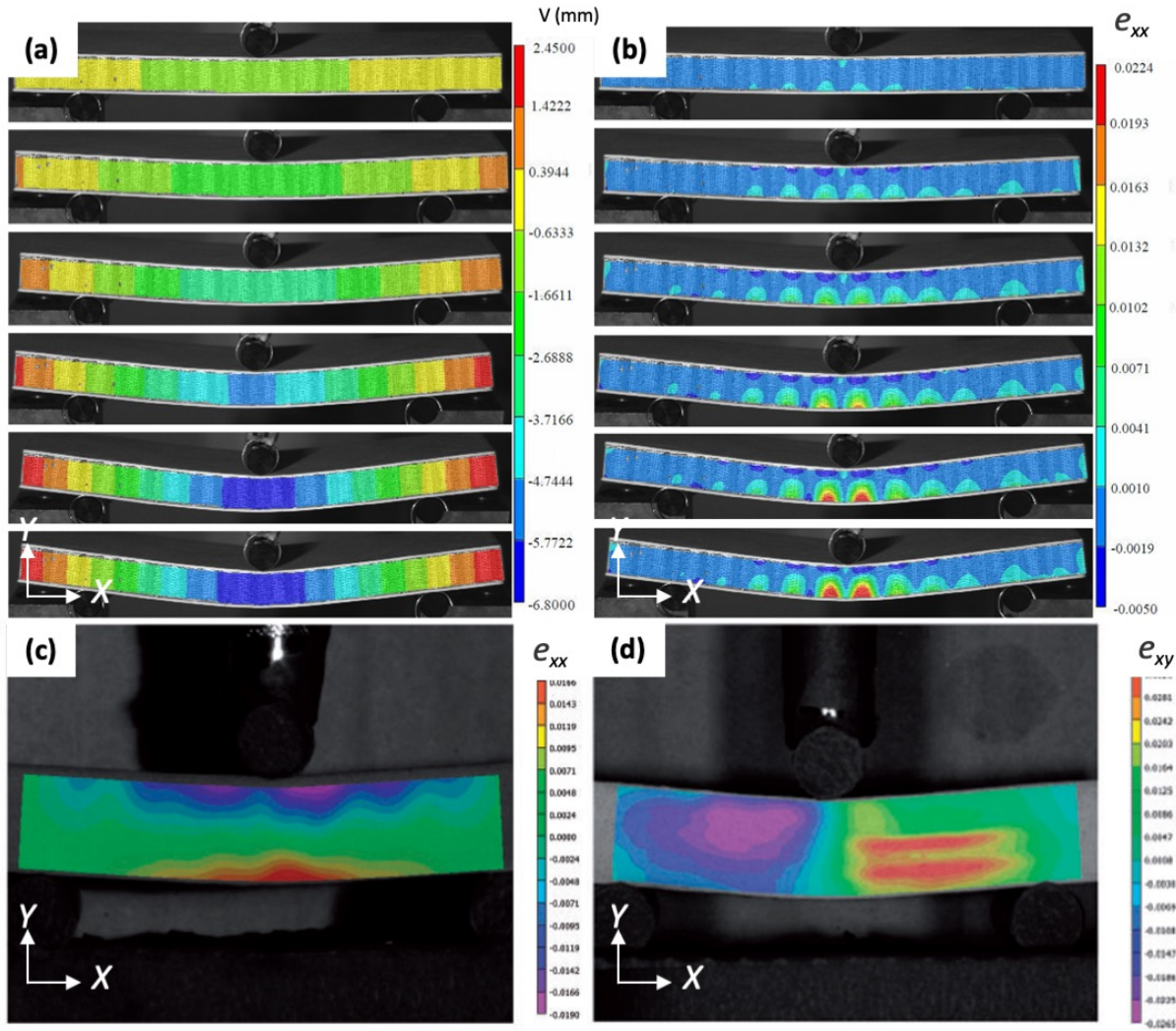


Figure 2.7 The DIC images of sandwich panels, as adopted from the literature, provide a clearer understanding of the deformation and failure mechanisms under flexural loading. (a) The evolution of the displacement field in the  $Y$  direction illustrates the deformation behavior of the sandwich panel, where displacement increases as the load is applied. (b) The strain field in the  $X$  direction before fracture shows the distribution of tensile strain across the panel. As the flexural load increases, maximum deformation and tensile strain are concentrated in the lower half of the panel, eventually leading to failure. (c) The  $e_{xx}$  strain at the maximum load highlights the area of high tensile strain, which indicates that the face sheet of the sandwich panel fails due to excessive tensile stress. (d) The  $e_{xy}$  strains at maximum load show a high concentration of shear strain near the center of the core, particularly on the right-hand side, which is associated with core shear failure. This indicates that shear strain is responsible for core failure, complementing the tensile failure observed in the face sheet. These DIC images provide valuable insights into the failure modes of sandwich panels, including tensile failure in the face sheets and shear failure in the core. Figure 2.7.a-b adapted from [99], and 2.7.c-d adapted from [100].

## CHAPTER 3 OBJECTIVES AND SCIENTIFIC CONTRIBUTIONS

### 3.1 Synthesis of the literature

The literature review highlighted the gaps in existing knowledge regarding the development of high-performance composites and filaments specially adapted for the utilization in FFF printing technology for the fabrication of robust parts designated for aerospace interior applications. These gaps are as follow:

- The porosity, the fiber length distribution, and the fiber alignment have a significant impact on the mechanical performance of both amorphous and semi-crystalline reinforced polymers. However, the effect of various thermal conditions during the FFF printing on layers adhesion and mechanical performance of semi-crystalline polymers are more severe, than those observed on amorphous polymers. The literature present gaps in terms of investigating and comparing the effect of porosity, fiber length, fiber alignment, and crystallization kinetic on printing quality and mechanical performance of FFF printed PEI and PPS composites.
- The existing commercial PEI and PPS filaments prove to be made only from some basic grades offering limited performance. The 3D printing market is dominated by a low number of big companies offering those filaments at prohibitive prices, as high as 500 \$/kg. Moreover, commercial PEI and PPS composite filaments containing low concentrations of fibers, up to a maximum of 15 wt.% of short carbon fibers, offering again a limited performance. This situation constraints the design space and calls for the development of a wider range of lower-cost and higher-performance composite filaments. In this context, rCF and TB can assure significant cost-advantage and performance enhancements when used in PEI, PPS resins.
- Only a few studies discuss the development of virgin carbon fibers reinforced PEI and PPS composites. The studies regarding PEI used the ULTEM 1000 matrix, while studies regarding PPS composites was for BAAM rather than FFF.
- There is no existing scientific work or commercially available filaments using the amorphous PEI ULTEM 1040A and the semi-crystalline PPS reinforced with rCF, TB particles, and their hybrid combinations. This combination of fillers, reinforcements, and

high-performance matrices is the first time studied and adapted to FFF technology in this work

- The impact of printing parameters on the mechanical properties of printed parts was addressed only for commercial filaments, such as neat PPS and neat ULTEM 9085. The mechanical performance resulted from these studies does not compete with the one of parts fabricated by conventional manufacturing processes. The printed PEI and PPS composites roughly attained 50 % of the performance of injection molded polymers or composites.
- Composites formulation solutions, such as the use of nano/submicron particles or by adding a secondary polymer phase were proposed to improve the thermal, electrical, and mechanical properties of composites. However, very limited or no studies exist on the development of new formulations based on high-performance thermoplastic adapted for FFF and for aerospace interior applications.
- So far, sandwich panels are mostly FFF printed with commodity polymer filaments. Studies dealing with such structures only focused on the effect of different core geometries on mechanical properties and on the optimization of 3D printing parameters. There is no published work presenting an extensive characterization of FFF printed sandwich panels made from high-performance thermoplastic polymers and composites.
- The development of performant sandwich panel structures using PEI and PPS composites is a promising alternative to Aluminum or Nomex honeycomb for aerospace applications, offering competitive thermal and mechanical properties. However, there is no study on FFF printing of sandwich panel structures made using PEI and PPS composite or hybrid filaments.
- Damage evaluation poses a significant challenge for FFF printed sandwich structures and there are limited studies that provide insights regarding suitability of using DIC system to analyse failure behaviour of FFF printed composite sandwiches under flexural loading.

## 3.2 Research objectives

The main objective of this thesis was the development of high-performance thermoplastic composites featuring significantly improved specific stiffness and strength, when compared to their injection molded neat matrices and, using FFF printing technology, to fabricate performant sandwich panel structures for aerospace interior applications.

This objective was attained by the successful completion of three specific objectives (SO):

**SO1: Development of novel amorphous composite formulations based on Polyetherimide (PEI) with the incorporation of recycled Carbon Fibers (rCF) and Thermal Black (TB) for their adoption in FFF technology**

**SO2: Development of novel semi-crystalline composite formulations based on Polyphenylene Sulfide (PPS) with the incorporation of recycled Carbon Fibers (rCF) and Thermal Black (TB) for their adoption in FFF technology**

**SO3: Fabrication of sandwich panel structures by FFF using novel and performant formulations of PEI and PPS composites and characterize their flexural properties.**

### Coherence between the specific objectives

To achieve the main objective of this thesis, **SO1** and **SO2** addressed important challenges related to high-performance composite behaviours to further understand the differences in mechanical performance between FFF printed and IM specimens. For this, multiple characterization methods were used. In this context, novel printable formulations of amorphous PEI and semi-crystalline PPS composites, containing rCF, TB, and their hybrid combinations, were developed and extensively studied to further adapt their behaviours to the FFF fabrication of sandwich panels. An extensive comprehension of these novel high-performance composites was achieved to further accomplish a maximum mechanical performance of FFF printed parts by correlating the performance to matrix crystallinity, fiber content, fiber length distribution, and alignment. **SO3** aimed to use the advancements obtained from **SO1** and **SO2** with the purpose to use FFF technology to manufacture performant sandwich panels for aerospace applications of interior parts such as air ducts, wall panels, seat frameworks etc.

### 3.3 Scientific contributions

#### **Article 1: Formulation and characterization of polyetherimide composites reinforced with recycled carbon fibers and thermal black particles for fused filament fabrication**

This article presents the development of novel PEI composite formulations by the incorporation of rCF, TB particles, and hybrid combinations of rCF/TB. These formulations of composites were compounded, injected, and extruded in filaments. FFF printing parameters were adjusted to PEI composites behaviours to improve the quality and the performance of the printed specimens. The effect of rCF and TB contents on the mechanical and thermal performance, and the microstructure of injected and FFF printed specimens were evaluated, analyzed, and compared.

*Scientific contribution - Article 1:* the development of unique formulations, using for the first time the PEI grade ULTEM 1040A as high-performance thermoplastic for 3D printing applications. The uniqueness is emanating also from the unique selection of rCF and TB as sustainable additives. Therefore, the ULTEM 1040A/rCF/TB are the first time studied here, and, more the first time applied successfully in FFF printing. There are no similar formulations or results existing in the scientific literature or available as commercial filaments.

The article was submitted in the Composite Part A: Applied Science and Manufacturing on April 16, 2024. The first author wrote the full article under the scientific supervision of Prof. Martin Lévesque, Prof. Daniel Therriault, and Dr. Mihaela Mihai.

#### **Article 2: Crystallinity, porosity, and microstructure of polyphenylene sulfide composite parts fabricated by filament-extrusion additive manufacturing**

This article presents the development of novel PPS composite formulations by the incorporation of rCFs, TB particles, and the combination of rCF/TB hybrids. Different formulations of PPS composites were compounded, injected, and extruded in filaments. The effects of incorporating rCF and TB on mechanical properties, on crystallization behaviour of PPS, on morphology, and on the microstructure of FFF printed parts were extensively investigated. The effect of processing conditions on the crystallinity content of PPS composites was examined, along with an investigation into the crystallization kinetics of the developed composites. The effect of



crystallinity, porosity, and microstructure on the properties of IM and FFF printed specimens were evaluated, analysed, and compared.

*Scientific contribution - Article 2:* the uniqueness of the work described here is emanating from the unique selection of PPS as thermoplastic matrix in combination to rCF and TB, as sustainable additives. Therefore, the PPS/rCF/TB are the first time extensively studied here and the first time applied successfully in FFF printing. There are no similar formulations or results existing in the scientific literature or available as commercial filaments.

The article was submitted to the Composite Part B: Engineering on October 07, 2024. The first author wrote the full article under the scientific supervision of Prof. Martin Lévesque, Prof. Daniel Therriault, and Dr. Mihaela Mihai.

### **Article 3: Flexural mechanical properties of sandwich panels fabricated by filament-extrusion of high-temperature thermoplastic composites**

This article presents the design of sandwich panels followed by their FFF printing using developed formulations of PEI and PPS composite filaments previously developed and analysed. The mechanical properties of the sandwich panels printed with these novel composite filaments were compared with those printed with commercial filaments. The printed sandwich panels were extensively characterized in terms of dimensional stability, microstructure, and flexural properties, proving to have adequate characteristics to further be adopted in aerospace interior applications.

*Scientific contribution - Article 3:* Sandwich panels having adequate performance for aerospace interior applications, made from novel formulations of PEI/rCF/TB and PPS/rCF/TB developed in this PhD research work, were the first time fabricated using the open-source FFF 3D printing technology.

The article was submitted to Additive Manufacturing on October 07, 2024. The first author wrote the full article under the scientific supervision of Prof. Martin Lévesque, Prof. Daniel Therriault, and Dr. Mihaela Mihai.

## CHAPTER 4      METHODOLOGY

### 4.1 Materials

ULTEM 1040A, a low viscosity PEI grade with a melt flow rate (MFR) of 77 g/10 min, was purchased from SABIC (Massachusetts, USA). PPS Fortron 0214P1 grade in a pellet form was purchased from Celanese (Celanese Corporation, Fortron Industries LLC., Wilmington, NC, USA). Recycled short carbon fibers, rCF, (re-Evo<sup>®</sup> HSC) were purchased from Carbon Conversion (Lake City, SC, USA). According to the manufacturer, the rCF have an initial length of 6 mm, an average diameter of 4.9  $\mu\text{m}$ , and the sizing content ranges between 1.5 and 3.5 wt.%. The sizing type and chemistry are not disclosed by the manufacturer. Characterization results to identify the type of sizing is provided in the **Appendix A**. Thermal Black (Thermax<sup>®</sup> N990, TB) particles were supplied by Cancarb Limited (Medicine Hat, AB, Canada). The TB spherical particles have an average size of 280 nm.

### 4.2 Processing methods

#### 4.2.1 Composite preparation and compounding

The pure PEI pellets were first dried at 140 °C for 12 hours, while the neat PPS pellets were dried at 100 °C for 12 hours before compounding. Prior to extrusion, the PEI and PPS pellets, along with TB particles were mechanically mixed to ensure even distribution, where the TB particles covered the surface of the pellets uniformly. The materials feeding mechanism consisted of the PEI/TB and PPS/TB mixtures being fed into the main hopper, while rCF was introduced through a side feeder. The compounding of PEI and PPS with rCF and TB was performed using a Bühler clamshell co-rotating twin-screw extruder (Bühler Group, Gupfenstrasse 5, Uzwil 9240, Switzerland) with the motor speed of 200 rpm. For PEI, the temperature profile of the extruder was incrementally set to rise from 280 °C to 350 °C, spanning from the feeding zone to the die. For PPS, the extruder temperature profile was incrementally set to rise from 280 °C to 330 °C, spanning from the feeding zone to the die for PPS.

The temperature profiles for both PEI and PPS extrusion were determined based on the technical datasheets of the respective polymer matrices to ensure optimal processing conditions. The extruded composites were cooled in air and subsequently pelletized. These pellets were later used for both injection molding (IM) and filament extrusion. **Table 4.1** lists the extruded PEI and PPS composite formulations containing combinations of rCF and TB.

During the processing of composites containing TB, specific safety measures were implemented to ensure safe handling and minimize health risks from airborne dust exposure and material contact. Dust generation and accumulation were controlled through carefully managed processes and regular surface cleaning. Local exhaust ventilation systems were utilized to maintain airborne dust concentrations within safe limits. To prevent skin, eye, and respiratory exposure, operators were equipped with appropriate personal protective equipment (PPE), including safety goggles or glasses, protective clothing, and approved respiratory protection as necessary.

Table 4.1 Formulations of the extruded composites of PEI and PPS matrices by using a twin-screw extruder.

Formulation	Matrix (wt.%)	rCF (wt.%)	TB (wt.%)
PEI/PPS	100	0	0
rCF/TB (20/00)	80	20	0
rCF/TB (15/05)	80	15	5
rCF/TB (10/10)	80	10	10
rCF/TB (00/20)	80	0	20

### 4.2.2 Injection molding (IM)

The compounded pellets of PEI and PPS composites were dried prior to injection molding, with PEI dried at 140 °C for 12 hours and PPS at 100 °C for 12 hours. Injection molding was carried out using a 34-ton Boy injection molding press (Boy Machines Inc, Exton, PA, USA). The injection barrel and mold temperatures were set based on the melting temperatures of the respective polymer matrices. For PEI, the barrel temperatures were incrementally increased from 280 °C to the 350-400 °C range, while for PPS, the temperatures were set to rise from 280 °C to 330 °C. The injection molding process utilized an injection speed of 30 mm/s, an injection pressure of 110 bar, and a screw rotation speed of 50 rpm, and the specimens were molded into heated molds maintained at a temperature range of 140 - 160 °C for both PEI and PPS, respectively.

Standard specimens were produced according to ASTM standards, specifically ASTM D638 for tensile properties, ASTM D790 for flexural properties, ASTM D256 for Izod impact strength, and ASTM D648 for heat deflection temperature evaluations.

### 4.2.3 Filament extrusion

The developed composites of PEI and PPS were processed into standard-sized FFF filaments using a filament making extruder (Xcalibur, Noztek, Shoreham, England). For PEI composites, the temperature profile of the extruder was set to rise from 370 °C to 390 °C at a motor speed of 25

rpm, while for PPS composites, the temperatures were set to increase from 330 °C to 350 °C with the motor speed of 25 rpm. **Figure 4.1** illustrates the filament extrusion system, where the filaments were melted using a single-screw extruder, cooled, and then spooled. During the spooling process, the filament diameter was continuously monitored to maintain a consistent  $1.75 \pm 0.05$  mm diameter and constant ovality. A laser control system operating at 1200 scans/s along the radial axes (Zumbach-ODAC18XY, Switzerland) was employed to ensure precision in filament dimensions.

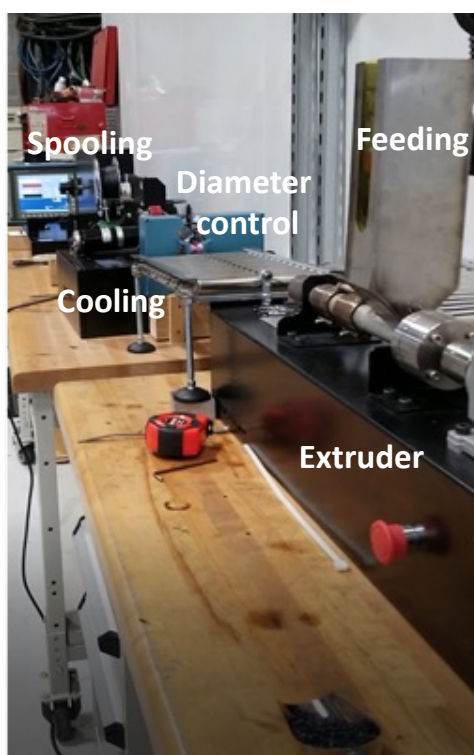


Figure 4.1 Image of the setup for composite filament manufacturing that includes a high-temperature single screw extruder, followed by a cooling system, conveyor belt, laser-controlled diameter monitoring system, and a spooling system.

#### 4.2.4 Fused filament fabrication (FFF)

Simplify3D software (Simplify3D-4.1.2, Cincinnati, OH, USA) was used to slice the 3D models of the specimens. An open-source 3D printer, AON-M2 (AON3D, Montreal, QC, Canada), was used to print the specimens which were oriented in the flatwise position according to their geometries defined by the ASTM standards used as shown in **Figure 4.2**.

The 3D printing parameters for the developed PEI and PPS composites were optimized through a systematic trial-and-error approach to achieve reduced porosity and improved mechanical

properties. Although no specific Design of Experiment (DoE) was employed, multiple printing trials were conducted by varying key parameters, including extrusion multiplier, extrusion width, layer height, printing speed, and nozzle temperature. Based on the iterative trials, the adjusted parameters were selected to minimize porosity and ensure good mechanical performance of the printed parts. The trial and final printing parameters are presented in **Table 4.2**.

For PEI composites, the final printing parameters included a nozzle diameter of 0.4 mm with a nozzle temperature of 400 °C, a heated bed temperature of 180 °C, and a heated chamber temperature of 130 °C. The specimens were printed with a raster angle of  $\pm 45^\circ$  relative to the horizontal plane, using 16 successive layers with a thickness of 0.2 mm, a layer width of 0.48 mm, and a 100% infill ratio.

For PPS composites, the final printing parameters consisted of a nozzle diameter of 0.4 mm with a nozzle temperature of 350 °C, a heated bed temperature of 160 °C, and a heated chamber temperature of 100 °C. The specimens were printed with an in-plane raster angle of  $\pm 45^\circ$  relative to the horizontal plane, using 16 layers with a thickness of 0.2 mm, a layer width of 0.48 mm, and a 100% infill ratio. Before printing, the composite filaments were dried at 100 °C for 12 hours to eliminate moisture and ensure high-quality processing.

Compared to the ASTM mechanical specimens, all final printing parameters for the PEI and PPS composites remained the same for the sandwich panel specimens, except for an increase in layer thickness from 0.2 mm to 0.3 mm and an increase in printing speed from 20 mm/s to 50 mm/s. These adjustments were made to reduce the printing time from over 10 hours to approximately 5 hours for the sandwich panel specimens.

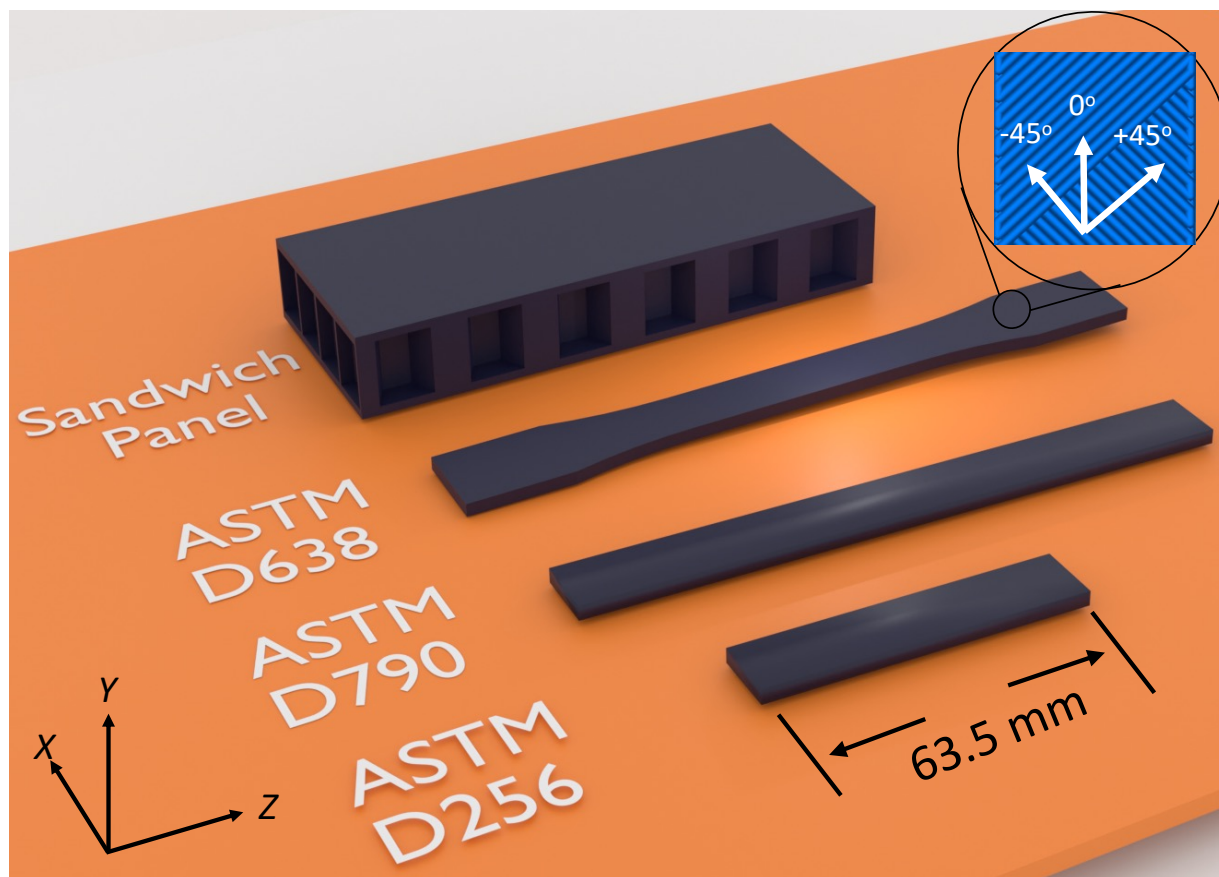


Figure 4.2 Schematic of specimens for mechanical testing, including sandwich panel, ASTM D638 (tensile test), ASTM D790 (flexural test), and ASTM D256 (impact test) geometries. The inset highlights the raster orientation of  $\pm 45^\circ$  used during FFF printing for all specimens.

Table 4.2 FFF printing parameters for PEI and PPS composite formulations were tailored by trial and error, with the trial range determined based on the technical data sheets of the neat PEI and PPS matrices.

Parameters	Trial values	Final PEI parameters	Final PPS parameters
Nozzle Temperature ( $^\circ\text{C}$ )	350-400	400	350
Bed Temperature ( $^\circ\text{C}$ )	160-180	180	160
Chamber Temperature ( $^\circ\text{C}$ )	100-130	130	100
Nozzle Diameter (mm)	0.4	0.4	0.4
Layer Thickness (mm)	0.2, 0.24, 0.3	0.2	0.2
Extrusion Width (mm)	0.4, 0.48, 0.55, 0.65	0.48	0.48
Extrusion Multiplier	0.90, 0.95, 1.00, 1.05, 1.10, 1.20	1	1
Printing Speed (mm/s)	20, 30, 50	20	20
Raster Angle ( $^\circ$ )	$\pm 45$	$\pm 45$	$\pm 45$
Infill Ratio (%)	100	100	100

## **CHAPTER 5      ARTICLE 1: FORMULATION AND CHARACTERIZATION OF POLYETHERIMIDE COMPOSITES REINFORCED WITH RECYCLED CARBON FIBERS AND THERMAL BLACK PARTICLES FOR FUSED FILAMENT FABRICATION**

Dogan Arslan<sup>a,b</sup>, Mihaela Mihai<sup>b</sup>, Daniel Therriault<sup>a</sup>, Martin Lévesque<sup>a</sup>

a: Department of Mechanical Engineering, Polytechnique Montreal, Montreal, QC., H3T 1J4, Canada

b: Advanced Manufacturing, Automotive and Surface Transportation Research Center, National Research Council Canada, 75 de Mortagne, Boucherville, QC., J4B 6Y4, Canada

Submitted to Composite Part A: Applied Science and Manufacturing on April 16, 2024.

### **5.1 Abstract**

The study aims to develop novel polyetherimide (PEI) composite formulations by the incorporation of recycled carbon fibers (rCFs), thermal black (TB) particles, and the combination of rCF/TB hybrids. Thermoplastic composites were prepared by melt compounding of an amorphous PEI, rCFs, and TB particles. Four (4) formulations of composites were prepared, with a maximum loading of 20 wt.% of rCF and a gradual replacement of rCF by TB. These formulations were used to manufacture standard specimens through injection molding (IM) and Fused Filament Fabrication (FFF) after being extruded into filaments. The effect of rCF and TB contents on the mechanical performance, the thermal behaviour, and on the microstructure of injected and FFF printed specimens were evaluated and analyzed. After the incorporation of 20 wt.% rCF, the tensile modulus of IM specimens increased from 3.20 GPa to 6.18 GPa, and the tensile strength increased from 74 MPa to 103 MPa, respectively. FFF printed composite specimens with 20 wt.% of rCF presented a tensile modulus of 4.23 GPa and a tensile strength of 70 MPa, respectively. The heat deflection temperature (HDT) of the IM and FFF printed composite increased from 177 °C to 200 °C with the addition of 20 wt.% of rCF, a common metric for assessing the maximum service temperature. X-ray micro-tomography was carried out to assess the composites' porosity contents and, as well, the rCF average length and orientations. X-ray micro-tomography results illustrated that the presence of rCF leads to a maximum porosity formation of up to 17 % in the FFF printed specimens. As expected, the initial length of the raw rCF was reduced from 6 mm down to approximately 30 µm mainly due to the shear forces applied during the different steps of the manufacturing process, i.e., composites compounding, filament extrusion, and FFF printing.

Scanning electron microscopy (SEM) images obtained on fractured surfaces revealed that the incorporation of TB seemed to improve the fiber matrix adhesion when compared to composites containing only rCF. The obtained results allowed us to understand the thermal and mechanical performance of these novel composites and their potential for FFF 3D printing of parts for aircraft interior or ground transportation applications.

## 5.2 Introduction

Carbon-based fibers and particles are used as reinforcement for developing thermoplastic composites for ground transportation and aerospace components [12-14, 53]. Thermal black (TB) is manufactured by burning natural gas in the absence of oxygen [21]. Unlike carbon black, TB is not electrically conductive due to its surface characteristics and its amorphous structure [22]. The production of TB particles yields hydrogen that is recirculated for reheating the reactor and for electricity generation. Moreover, the market price of TB (~2 \$/kg) is significantly lower than that of virgin carbon fiber (CF) (~60 \$/kg) [22, 101].

The effect of using TB particles and CF on the thermal and mechanical properties of different polymers, such as polyamide (PA6), polypropylene (PP), acrylonitrile butadiene styrene (ABS), and polyphenylene sulfide (PPS), has been studied in the literature [24]. It was reported that the addition of TB could improve the fiber-matrix adhesion by anchoring the mixture of TB-matrix on the surface of CF. The recycling process of CF wastes to manufacture recycled carbon fibers (rCF) was reported to require roughly 5-10 % of the energy expenditure associated with the manufacturing of virgin CF [15, 16]. Using rCF in combination with TB represents a more sustainable approach due to its cost-efficiency and substantially lower energy requirements, when compared to using virgin CF and furnace carbon black.

Fused filament fabrication (FFF) is an open-source three-dimensional (3D) printing technology that uses a filament of a thermoplastic material or its composite, which is heated to its melting point and then extruded through a small nozzle to create a 3D object, layer by layer [9, 10, 102, 103]. The mechanical performance of 3D printed composite parts strongly depends on the fiber content, the inter- and intra-layer porosity, the fiber distribution, the fiber aspect ratio, the fiber-matrix adhesion, and the layer-to-layer adhesion [10, 25]. Liao et al. [38] reported that gradually increasing the weight fraction of CF from 2 wt.% to 10 wt. % in polyamide (PA12) increased the stiffness and strength by up to 260 % and 102 %, respectively. However, they also demonstrated a reduction in



impact strength by 46 % from the nominal value of neat PA12. The tensile modulus and strength of FFF printed specimens made from 30 wt.% reinforced polyetheretherketone (PEEK) along the longitudinal direction showed significant enhancement of up to 500 % and 61 %, respectively, when compared to the neat matrix [104]. The incorporation of CF into PPS and PEEK matrices increased their zero-shear viscosity by up to 3 orders of magnitude. This increase of the viscosity could have a negative impact on the material's flow characteristics during the IM and FFF printing processes [41]. Moreover, filaments containing 15 wt.% of CF have been observed to cause porosity content of 15-25 % in printed parts [47]. The porosity can potentially lead to bonding defects between layers during the printing process, which could promote crack initiation and mechanical failure of the structures [32, 34-36]. The trade-off between the increased mechanical properties, melt viscosity, and porosity is an important consideration when developing composite formulations for FFF printing applications [10, 25].

High-temperature resistant and high-performance thermoplastic polymer families include polyimides, polysulfone, polyaryletherketones, and polyphenylsulfides [4, 51, 54, 105]. Polyetherimide (PEI), also known under the commercial name ULTEM, has a tensile strength of up to 110 MPa, heat deflection temperature (HDT) of up to 175 °C, and inherent flame retardancy. The melt flow properties of PEI allow its melt processing by extrusion, injection molding, and FFF technology, depending on its grade. ULTEM 1040A stands out among ULTEM grades due to its lower melt viscosity, making it a suitable choice for fillers and fibers incorporation at contents up to 30 wt.%. The average molecular weight ( $M_w$ ) of ULTEM 1040A is reported to be 23,100 g/mol, when compared to 33,200 g/mol for ULTEM 1010 and 38,300 g/mol for ULTEM 1000 grades, respectively [106]. The inherently lower melt viscosity and molecular weight of ULTEM 1040A, in comparison to other ULTEM grades, could possibly play a significant role in promoting layer-to-layer adhesion during FFF printing.

ULTEM 9085, 1010, and 1000 based composites and filaments are the most studied from the ULTEM family [66, 105]. On the other hand, there is a noticeable gap between the existing literature and the 3D printing industry regarding the ULTEM 1040A composites and filaments. For example, Chuang *et al.* [48] studied the mechanical properties and printing quality of 10 wt.% CF reinforced ULTEM 1000. It was reported that the printed ULTEM 1000 composites exhibit a tensile performance equivalent to 50 % of the injection molded neat ULTEM 1000. This reduction in mechanical performance was primarily attributed to the relatively high porosity, which was

observed at ~25 % in the printed composite parts. On the other hand, the commercially available ULTEM filaments are limited to a few manufacturers and are very expensive, up to 10-fold, when compared to polymer pellets. Moreover, the commercially available carbon fiber reinforced PEI filaments with a diameter of 1.75 mm are currently limited to the maximum loading of a of 15 wt.% of CF. Neat filaments of ULTEM 9085 and ULTEM 1010 are also commercially available [55]. Hence, there is a strong interest from the FFF community and industry to develop the knowledge on new reinforced ULTEM 1040A FFF feedstock materials. Composites made of this PEI grade have not been investigated yet in terms of their mechanical performance and FFF printing behavior.

This study represents the first publicly available investigation into various PEI ULTEM 1040A composite formulations tailored for the FFF printing process. The research involves developing novel composite formulations by the incorporation of rCF, TB particles, and rCF/TB hybrid combinations at different weight percentages. The evaluation covers the mechanical, thermal, and morphological properties of composites for both injection molded (IM) and FFF printed specimens. This study aims to develop PEI/rCF/TB composites featuring improved specific stiffness and strength of specimens fabricated using FFF, when compared to IM pure PEI and its composites.

## **5.3 Materials and Methods**

### **5.3.1 Materials**

ULTEM 1040A, a low viscosity PEI grade with a melt flow rate (MFR) of 77 g/10 min, was purchased from SABIC (Massachusetts, USA). Recycled short carbon fibers, rCF, (re-Evo<sup>®</sup> HSC) were purchased from Carbon Conversion (Lake City, SC, USA). Thermal Black (Thermax<sup>®</sup> N990, TB) particles were supplied by Cancarb Limited (Medicine Hat, AB, Canada).

### **5.3.2 Methods**

#### **5.3.2.1 Compounding**

The pure PEI pellets were dried before compounding processing at 140 °C for 12 hours. PEI pellets were compounded with rCF and TB by using a Bühler clamshell co-rotating twin-screw extruder (Bühler Group, Gupfenstrasse 5, Uzwil 9240, Switzerland). The temperature profiles of the extruder were set to incrementally rise from 280 °C to 350 °C, from the feeding zone to the die. PEI pellets, TB, and rCF were fed through separate feeders into the forward area of the extrusion

line. The extruded composites were cooled down in the air and pelletized. The pellets were further used in the injection molding step and filament extrusion. **Table 5.1** lists the extruded formulations containing combinations of rCF and TB.

Table 5.1. Formulations of the extruded composites using a twin-screw extruder.

<b>Formulation</b>	<b>PEI (wt.%)</b>	<b>rCF (wt.%)</b>	<b>TB (wt.%)</b>
PEI	100	0	0
PEI/rCF/TB (80/20/00)	80	20	0
PEI/rCF/TB (80/15/05)	80	15	5
PEI/rCF/TB (80/10/10)	80	10	10
PEI/rCF/TB (80/00/20)	80	0	20

### 5.3.2.2 Injection molding (IM)

The compounded pellets of composites were dried as specified before and then injection molded using a 34-ton Boy injection molding press (Boy Machines Inc, Exton, PA, USA). The injection barrel and mold temperatures were adapted as a function of the melting temperature of PEI polymer matrix. Standard specimens were molded according to ASTM D638, ASTM D790, ASTM D256, and ASTM D648 for tensile, flexural, unnotched Izod impact, and heat deflection temperature evaluations, respectively.

### 5.3.2.3 Filaments extrusion

The developed composites were transformed into standard size FFF filaments (**Figure 5.1(a)**) by using a filament-making extruder (Xcalibur, Noztek, Shoreham, England). The filaments were continuously monitored for a constant diameter of  $1.75 \pm 0.05$  mm, and a constant ovality by using a laser controlling system with 1200 scan/s along radial axes (Zumbach-ODAC18XY, Switzerland). The compounded pellets were dried as specified prior to their melt transformation into filaments.

### 5.3.2.4 Fused filaments fabrication

The software Simplify3D (Simplify3D, USA) was used to slice the 3D computer-aided designs of the specimens on the flatwise position based on their shape. The approach was to fabricate similar specimens by FFF and by injection molding, for further characterization using the same ASTM tests. An open-source printer, the AON-M2 (AON3D, Montreal, QC, CA) was used to print the specimens. The parameters used for the printing of the specimens were: nozzle diameter of 0.4 mm (400 °C), heated bed of 180 °C, chamber temperature of 130 °C, a raster angle of  $\pm 45^\circ$  relatively

to the horizontal plane. The specimens were printed with 16 successive layers, each with a thickness of 0.2 mm and a width of 0.48 mm, providing a 100 % infill ratio. Some of the printed specimens are presented in the **Figures 5.1(b)** and **5.1(c)**.

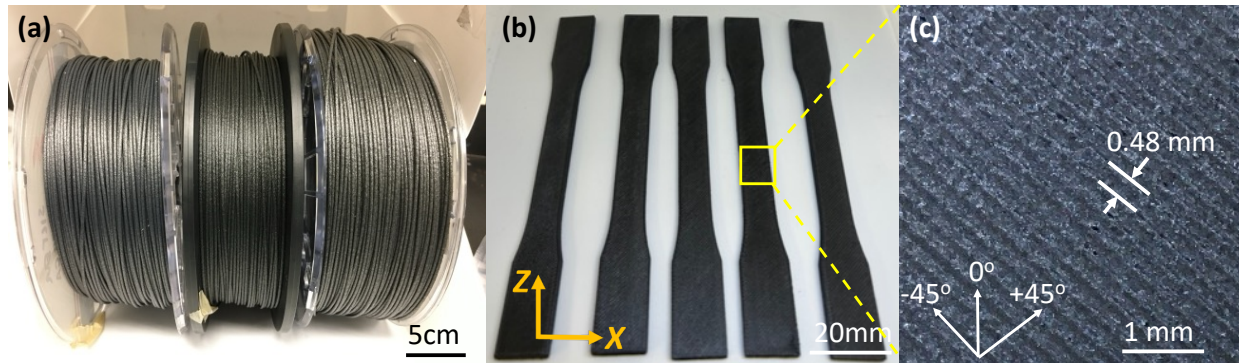


Figure 5.1 Images of extruded composite filaments and of FFF printed ASTM specimens; (a) PEI composite filament spools (from left to right; rCF/TB (20/00), rCF/TB (15/05), and rCF/TB (10/10)), (b) FFF printed Type-1 dogbone specimens (ASTM D638) by using filament containing rCF/TB (20/00) for tensile testing, (c) Optical microscopy images showing details on FFF printed dogbone specimens' surface.

### 5.3.3 Characterization techniques

#### 5.3.3.1 Morphology and microstructural analysis

Scanning electron microscopy (SEM) was used to observe the fractured surfaces of composites using a Hitachi-TM3030Plus (Hitachi High-Tech Corporation, Hitachinaka, Japan) at an accelerating voltage of 15 kV. The surfaces of composite filaments were prepared by fracturing them in liquid nitrogen to provide brittle surface fracture, while the surfaces observed for IM and FFF printed specimens were those resulting from failure during mechanical testing. A chromium coating of 20 nm was applied on the surface of the specimens before SEM observation.

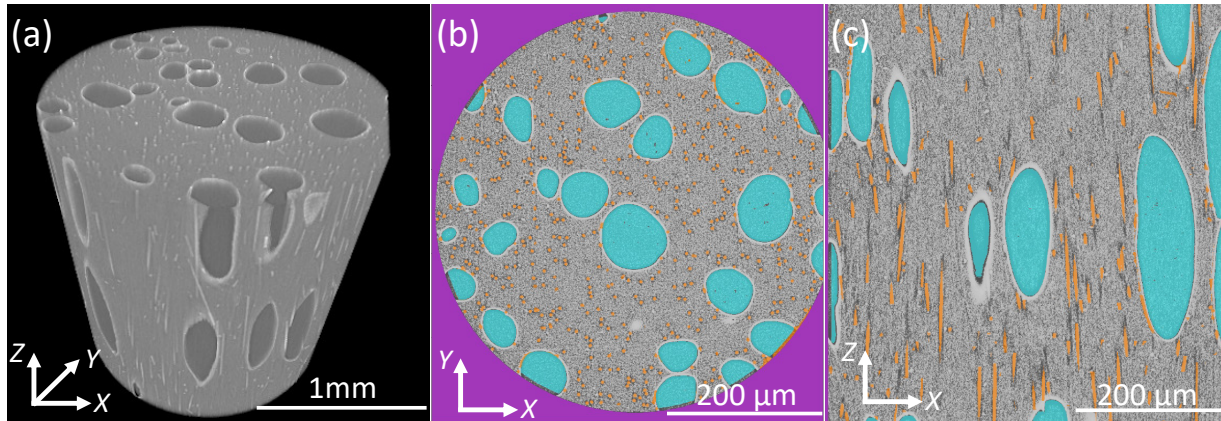


Figure 5.2 Micro-CT analysis of PEI containing rCF/TB (20/00) composite filaments processed with the OpenFiberSeg tool: (a) reconstructed scanned volume, (b)  $XY$  cross-section of the composite filament, (c)  $XZ$  cross-section of the composite filament.

Micro-CT analysis was carried out to observe the porosity and the rCF distribution of orientation with a Zeiss XradiaTM 520 Versa X-ray computed tomography system (Carl Zeiss Microscopy GmbH, Jena, Germany). The applied source voltage and power were 80 kV and 7 W, respectively, with a 10X objective without filter, for an exposure time of 1.2 s. The scans were analyzed with an open-source segmentation tool (OpenFiberSeg) for porosity and fiber distribution analysis [107]. **Figure 5.2** features representative micro-CT images of the extruded composite filament having a diameter of 1.75 mm. **Figure 5.2(a)** represents the reconstructed scanned volume in which the  $Z$ -axis indicates the extrusion direction. **Figure 5.2(b)** and **5.2(c)** represent the processed micro-CT data by using the OpenFiberSeg tool for the  $XY$  and  $XZ$  planes, respectively. The porosities and carbon fibers were successfully detected and labeled in blue and orange, respectively. The aforementioned micro-CT scan was repeated at least twice for each formulation of filaments (1.75 mm), FFF printed, and IM dogbone specimens that have not undergone tensile testing.

### 5.3.3.2 Heat deflection temperature

The HDT was determined using an Instron Ceast HDT-3-Vicat (Instron, Norwood, MA, USA). The rectangular beam specimens, obtained by IM and FFF printing, had a thickness of 3.2 mm, a length of 105 mm and a width of 12.7 mm. The ASTM D648 standard was applied as follows: the cross-section of a rectangular beam was loaded in the edgewise position until stress of 1.82 MPa was reached. The specimens were tested in a heat-transfer medium (silicon oil) in which the temperature was increased by 2 °C/min. The HDT was recorded when test specimens deflected by

0.25 mm under the applied load. At least three (3) specimens were tested for each formulation and the test results are presented as a mean value with a confidence interval (CI) of 95 %, which is reported in parentheses in the sequel.

### **5.3.3.3 Mechanical characterization**

Tensile and flexural specimens made by IM and FFF were tested for each composite formulation. Testing was carried out according to ASTM D638 and ASTM D790 standards using an MTS Insight electromechanical testing machine equipped with a 50 kN load cell at room temperature (MTS Systems, Eden Prairie, MN, USA). Tensile tests were done with a crosshead speed of 5 mm/min. The flexural tests were conducted using a support span of 105 mm for IM specimens and 51.3 mm for FFF printed specimens, with a crosshead speed of 2.6 mm/min. The differing support span lengths were chosen because FFF printed specimens exhibit higher deflection, necessitating adjustment to minimize noise in the data and prevent specimen slipping during testing, in accordance with ASTM standards. Five (5) conditioned specimens for each composite formulation were tested and the mean values are further reported for tensile modulus (TM), tensile strength (TS), flexural modulus (FM), and flexural strength (FS).

The Izod impact strength was measured with a ZwickRoell impact device (ZwickRoell LP, Kennesaw, GA, USA). The unnotched specimens were both IM and FFF printed. The tests were performed according to ASTM D256 using a 2 kg hammer. The impact tests were repeated eight (8) times for each formulation and their mean values are reported with a CI of 95 %. Before mechanical testing, all the specimens were conditioned at 23 °C, 50 % RH for at least 40 hours.

## **5.4 Results and Discussion**

### **5.4.1 Microstructural characterization of the manufactured composites**

#### **5.4.1.1 Micro-CT and SEM analysis of composite filaments**

**Figure 5.3** provides the information obtained through micro-CT scanning of the filaments on the porosity density, as well as graphs depicting the distribution of porosity size. The porosity density images were generated by projecting the three-dimensional porosities onto the axial planes (**Figure 5.3(a)**). *X*, *Y*, and *Z* are representing the axes of the 3D image for the filament, *Z* being aligned along the extrusion direction. The 2D image projections were obtained by summing the pixel values

along an axis. For example, in the  $XY$  plane, the pixel intensity values were summed along the  $Z$  axis for each fixed  $(x,y)$  coordinate in that plane. The pixels that contained pores were assigned a value of 1, while all other pixels were given a value of 0. Subsequently, the cumulative sum of pixels that contains porosity within the volume was provided as a normalized 2D color map of porosity density, with respect to the highest pixel count along the  $XY$  and  $XZ$  planes (**Figures 5.3(b.1)-(d.1)** and **((b.2)-(d.2))**). This ensures that the visualization accurately represents the relative intensities in the original 3D image. These images provide new complementary qualitative information about porosity density and distribution that corroborates the porosity distribution plots. The normalized density levels are indicated by yellow and blue colors, which correspond to the upper and lower bounds on the scale bar, respectively, where high values indicate concentrated porosities and low values indicate the absence of porosities. In **Figures 5.3(b.3)-(d.3)**, the porosity size distribution is reported as a function of radial axis. The volume of porosity was extracted with OpenFiberSeg. Then, the location of centroid of each porosity were determined and their distance from the center of the filament along the radial axis was computed. This allows us to compute the porosity size distribution with a CI of 95 % as a function of the radial coordinate.

**Figures 5.4(a-d)** show SEM micrographs of filament cross-sections for each composite formulation. This qualitative analysis supports the micro-CT data on porosity within filament cross-sections, providing a visual insight into the porosity levels on 2D surfaces of the filaments.



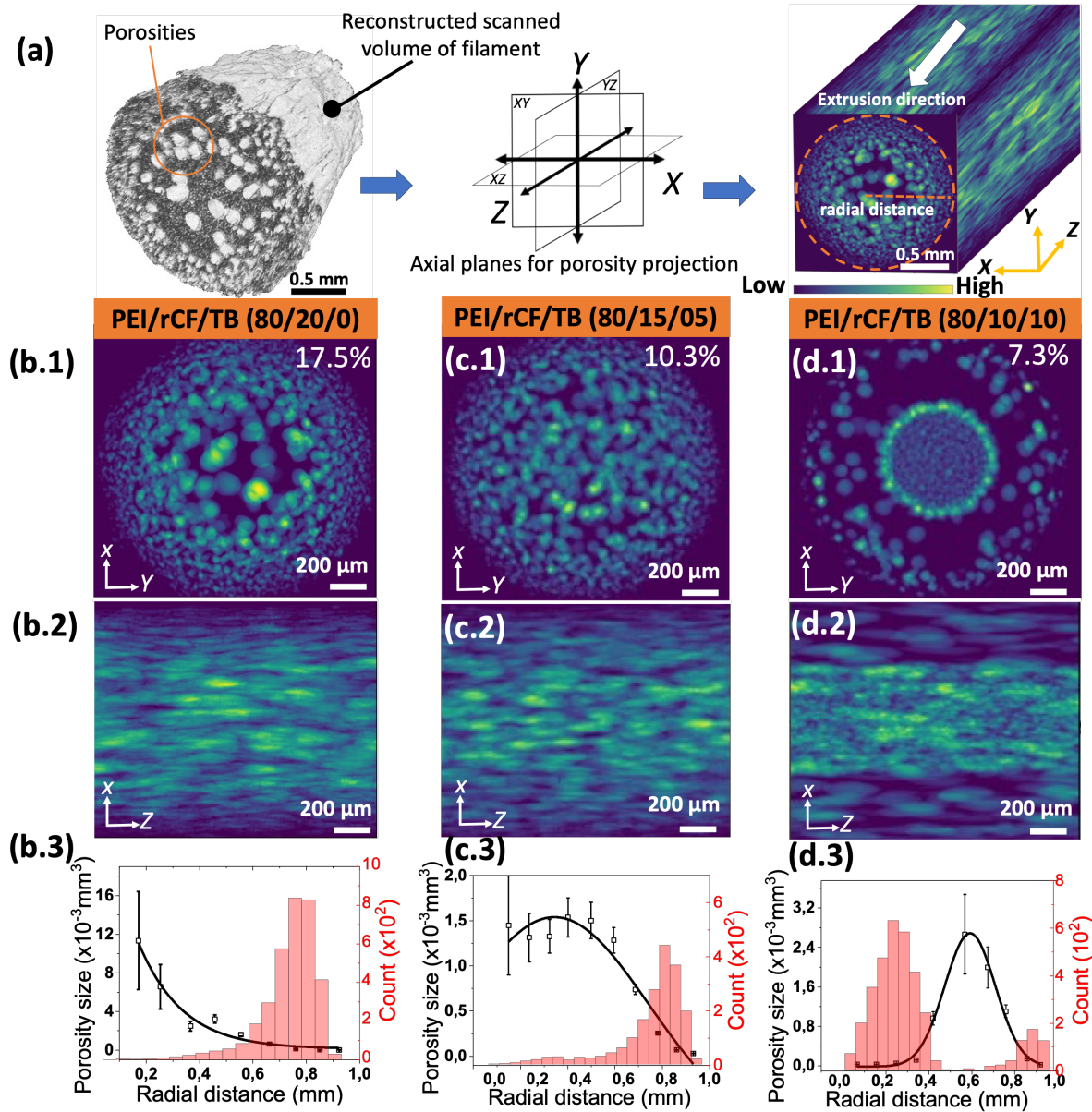


Figure 5.3 (a) Isometric 3D view representing the composite filament volume with porosity projection onto axial planes. Micro-CT images of porosity density and their corresponding porosity content (b.1-d.1, and b.2-d.2), and plots of porosity size distribution (b.3-d.3) computed with a CI of 95 % for the composite filaments, (b.1-b.3) PEI/rCF/TB (80/20/00), (c.1-c.3) PEI/rCF/TB (80/15/05), (d.1-d.3) PEI/rCF/TB (80/10/10).

The incorporation of rCF leads to the formation of porosity of 17.5 (2) % for composite filament containing rCF/TB (20/00). The porosity content is decreased down to 10.3 (1.7) % and 7.3 (1.5) % for composite filament containing rCF/TB (15/05) and rCF/TB (10/10), respectively. There is no detectable porosity inside the filament containing rCF/TB (00/20) (detailed data on this aspect is not presented here).



**Figure 5.3(b.2)** shows the porosities that are present throughout the entire cross-section observed, consisting of small and large porosities for the composites containing rCF/TB (20/00). Smaller porosities, measuring up to  $\sim 0.001 \text{ mm}^3$ , are densely distributed towards the edges as can be verified with SEM images of filament cross-sections (**Figure 5.4(a)**). The variation in the size of the small porosities is very small as they have relatively small standard deviation of  $\sim 10^{-6} \text{ mm}^3$ , when compared to large porosities. The large porosities have higher standard deviation of  $\sim 10^{-2} \text{ mm}^3$ , with the sizes reaching up to  $\sim 0.016 \text{ mm}^3$ . The larger porosities are predominantly located in the central region of the filament. This porosity distribution in the filaments were due to the melt flowing characteristics through the extrusion die, where high shear forces were maximal to the die walls, which caused a reduction in the porosity sizes on the filament's walls. The replacement of rCF by TB not just reduced the porosity content but also reduced the overall size of the porosities. The size of the porosities became relatively finer, reaching a maximum of  $\sim 0.003 \text{ mm}^3$  for the composites containing rCF/TB (15/05) and rCF/TB (10/10), respectively (**Figures 5.3(c.2)** and **(d.2)**). For the composite filaments containing rCF/TB (15/05), the larger porosities are more evenly distributed with average volume of  $\sim 0.0015 \text{ mm}^3$ , when compared to the composite filaments containing rCF/TB (20/00). The larger porosities are mostly located in the central region, with a higher deviation, while the smaller porosities are located near the outer perimeter of the filament with a smaller size deviation at the edges, as can be verified with SEM images of filament cross-sections (**Figure 5.4(b)**). The replacement of rCF with TB significantly changes the porosity distribution for the composite filaments containing rCF/TB (10/10) by introducing in two different small porosity regions. The porosities with a volume of  $\sim 0.0001 \text{ mm}^3$  are located in the center and near the outer perimeter of the filament. There is a region between filament center and perimeter where a small amount of larger porosities are located with a volume of  $\sim 0.003 \text{ mm}^3$ . It seems that the TB incorporation shifted the location of the porosities toward the filament center, which can be clearly observed in SEM images of filament cross-sections (**Figure 5.4(c)**).

The porosity formation is thought to be primarily due to the presence of rCF, as porosity content increases as a function of rCF content. Epoxy based sizing was identified on the rCF surfaces and epoxy starts to degrade at  $\sim 300\text{-}330 \text{ }^\circ\text{C}$ , up to  $470 \text{ }^\circ\text{C}$  [49, 108]. Thus, the epoxy sizing degradation at the filament extrusion temperature could form degradation gases that remained trapped within the volume of the filaments. Consequently, as **Figure 5.4(d)** presents, composites containing

rCF/TB (00/20) exhibit a noticeable reduction in porosity (0.2 %) due to the absence of rCF, and thus, the absence of epoxy and degradation gases during filament extrusion.

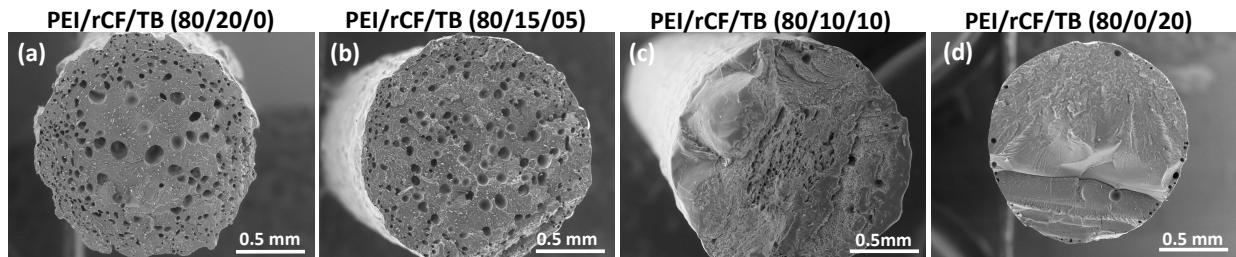


Figure 5.4 SEM images of the fracture surface of composite filaments: (a) PEI/rCF/TB (80/20/00), (b) PEI/rCF/TB (80/15/05), (c) PEI/rCF/TB (80/10/10), (d) PEI/rCF/TB (80/00/20).

#### 5.4.1.2 Micro-CT analysis of IM and FFF printed composite specimens

**Table 5.2** compares statistical values for the fiber length distribution, the orientation, and the porosity content for samples extracted from dogbone specimens prior to mechanical testing. The average fiber length and deviation angle were computed on a sample size of  $\sim 15,000$  individual fibers. The deviation angle represents the angle of the deviation of fibers from the Z-axis which is the injection/extrusion direction. The total porosity, which encompasses both inter-layer and intra-layer porosities in the FFF printed dogbone specimens, is 16.8 % for the composites containing rCF/TB (20/00). As the rCF content was replaced by 5 wt.% and 10 wt.% of TB, the total porosity gradually decreased down to 13.8 % and 7.1 %, respectively. The FFF printed composite containing rCF/TB (00/20) exhibited a total porosity of 2.8 %, consisting solely of inter-layer porosities. The porosity content increased linearly for FFF printed specimens with increasing rCF content, while no detectable porosities were found in the IM specimens for all the formulations. The lack of porosities in IM specimens is due to high injection pressure used to fill-in the mold. When compared at IM, there is no high pressure applied to the melt during FFF printing. The micro-CT results regarding the porosity content demonstrate that the adjusted FFF printing parameters enabled us to obtain low porosity content FFF printed specimens, down to 2.8 %.

Table 5.2 Micro-CT analysis of FFF printed and IM PEI composites: quantitative values regarding porosity content and rCF length distribution and orientation. The average values are reported with CI of 95 % in the parentheses.

Specimen	Composite formulation	Porosity (%)	rCF length ( $\mu\text{m}$ )	Deviation angle ( $^\circ$ )
IM	PEI/rCF/TB (80/20/00)	$\sim 0$	41.1 (0.85)	34.7 (0.38)
	PEI/rCF/TB (80/15/05)	$\sim 0$	22.4 (0.34)	44.7 (0.37)
	PEI/rCF/TB (80/10/10)	$\sim 0$	19.5 (0.22)	47.5 (0.33)
	PEI/rCF/TB (80/00/20)	$\sim 0$	-	-
FFF	PEI/rCF/TB (80/20/00)	16.8 (1.4)	36.6 (0.22)	46.2 (0.22)
	PEI/rCF/TB (80/15/05)	13.8 (0.8)	24.1 (0.41)	39.1 (0.36)
	PEI/rCF/TB (80/10/10)	7.1 (1.9)	30.4 (0.96)	41.3 (0.56)
	PEI/rCF/TB (80/00/20)	2.8 (0.7)	-	-

The FFF printed composite specimens containing rCF/TB (20/00), rCF/TB (15/05), and rCF/TB (10/10) have average fiber lengths of 36.6  $\mu\text{m}$ , 24.1  $\mu\text{m}$ , and 30.4  $\mu\text{m}$ , respectively. In contrast, the IM composite specimens containing rCF/TB (20/00), rCF/TB (15/05), and rCF/TB (10/10) have average fiber lengths of 41.1  $\mu\text{m}$ , 22.4  $\mu\text{m}$ , and 19.5  $\mu\text{m}$ , respectively. The size of rCF with an initial length of 6 mm was significantly reduced due to the shearing effects during compounding, IM, filament extrusion, and FFF printing processes. Considering the diameter of rCF, which is  $\sim 5$   $\mu\text{m}$ , the aspect ratio of rCF in the manufactured composites ranged from 4 to 10 for composite formulations. The aspect ratio of the short fibers significantly affect their orientation in the matrix, thus mechanical performance of the composites [25]. High aspect ratio fibers tend to align more effectively with the flow direction due to shear forces [109].

**Figure 5.5** compares the deviation angle distribution of rCF for each composite formulation. The solid bars represent the deviation angle of the IM specimens while patterned bars represent those of the FFF printed specimens. The average deviation angles for the IM specimens are  $34.7^\circ$ ,  $44.7^\circ$ , and  $47.5^\circ$  for composites containing rCF/TB (20/00), rCF/TB (15/05), and rCF/TB (10/10), respectively. It seems the fibers are randomly distributed on the entire range of angles (i.e.,  $0^\circ$ - $90^\circ$ ), while the fibers are more aligned for composites containing rCF/TB (20/00) (**Figure 5.5(a)**). The relatively longer average fiber length of the composites containing rCF/TB (20/00) might lead to increased fiber alignment, when compared to composites containing rCF/TB (15/05), and rCF/TB (10/10), and considering also the effect of TB particles presence that inhibit the molecular mobility of the matrix. The average deviation angles are  $46.2^\circ$ ,  $39.1^\circ$ , and  $41.3^\circ$  for FFF printed composites containing rCF/TB (20/00), rCF/TB (15/05), and rCF/TB (10/10), respectively. The deviation angle distribution seems to be uniform, pointing to a random orientation distribution, while composites containing rCF/TB (20/00) seem to exhibit higher fiber alignment, as observed for IM specimens (**Figure 5.5(b)**).

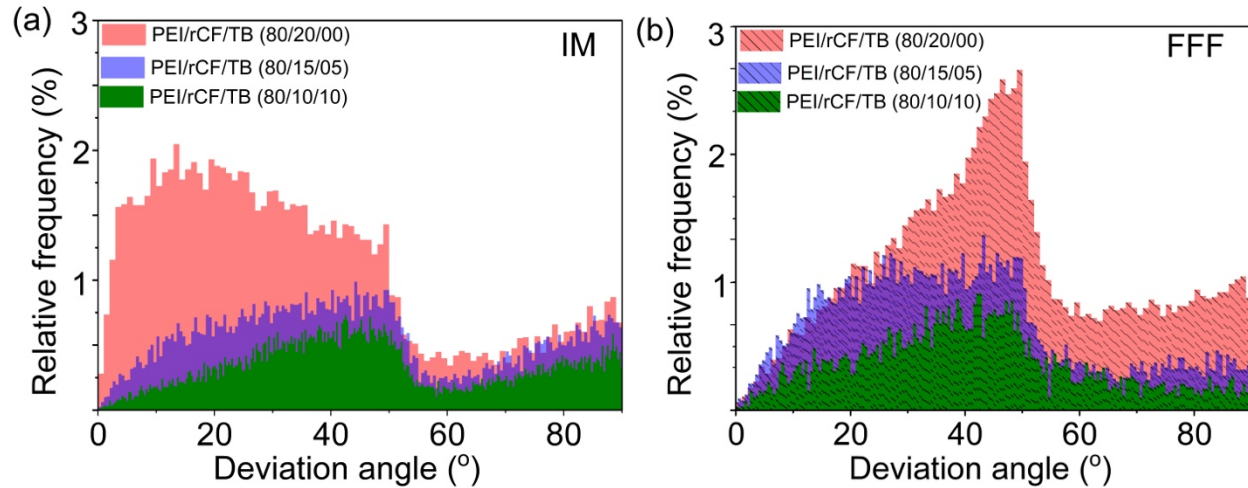


Figure 5.5 Plots of rCF deviation angle distribution for developed composites; (a) IM and (b) FFF printed dogbone specimens.

IM composites containing rCF/TB (20/00) have slightly longer average fiber lengths and are more aligned, when compared to FFF printed parts. The replacement of rCF content by TB particles further reduced the average rCF length and also restricted the rCF alignment through extrusion/injection flow direction for both IM and FFF printed specimens. This could be due to the high number of interactions of nano-scale TB particles with rCF. Consequently, these substantial interactions between rCF-TB, rCF distribution orientation along the matrix, and total porosity content are expected to significantly affect the mechanical performance of IM and FFF printed parts.

#### 5.4.1.3 SEM analysis of fracture surfaces of IM and FFF printed specimens

**Figure 5.6** shows SEM images of the fracture surfaces of Izod impact specimens obtained in IM with three (3) different magnifications for each formulation. From the top to the bottom, the SEM images represent the formulation of composites containing rCF/TB (20/00), rCF/TB (15/05), rCF/TB (10/10), and rCF/TB (00/20), respectively.

**Figure 5.6(a.1)-(a.3)** shows uniform rCF dispersion and distribution in the PEI matrix for the composites containing rCF/TB (20/00), which suggests that the mixing strategy used was appropriate. A mix of fiber breakage, fiber pull-outs, and partially wetted fiber surface that is seen in the SEM images (**Figure 5.6(a.3)**) may indicate a moderate level of adhesion between rCF and the matrix.

**Figures 5.6(b.1)-(b.3)** and **(c.1)-(c.3)** represent the fracture surface of PEI hybrid composites containing rCF/TB (15/05) and rCF/TB (10/10), showing the same uniform fiber distribution. The incorporation of TB seems to enhance the fiber-matrix adhesion since the rCF surfaces were covered by the matrix and by TB particles, as well (**Figures 5.6(b.2)-(b.3)** and **(c.2)-(c.3)**). The similar surface chemistries of rCF and TB, providing carbon-carbon interactions, may improve the affinity between rCF and TB, as well as between the matrix and rCF [24]. The TB particles, attached to the surface of rCF, have possibly increased the surface area of rCF while promoting more bonding sites for the PEI matrix. Such phenomenon is expected to increase the reinforcement efficiency of rCF, with a potential positive effect expected further on the mechanical performance. **Figures 5.6(d.1)-(d.3)** shows a smooth fracture surface of composites containing rCF/TB (00/20). TB particles are finely dispersed along the matrix without significant agglomerations, which indicates a moderate affinity between the matrix and TB particles. Overall, these SEM images of the fracture surfaces reveal a uniform distribution of rCF and TB throughout the matrix. There is also a clear enhancement in fiber matrix adhesion for hybrid composites, which is expected to favor the mechanical performance of these composites.

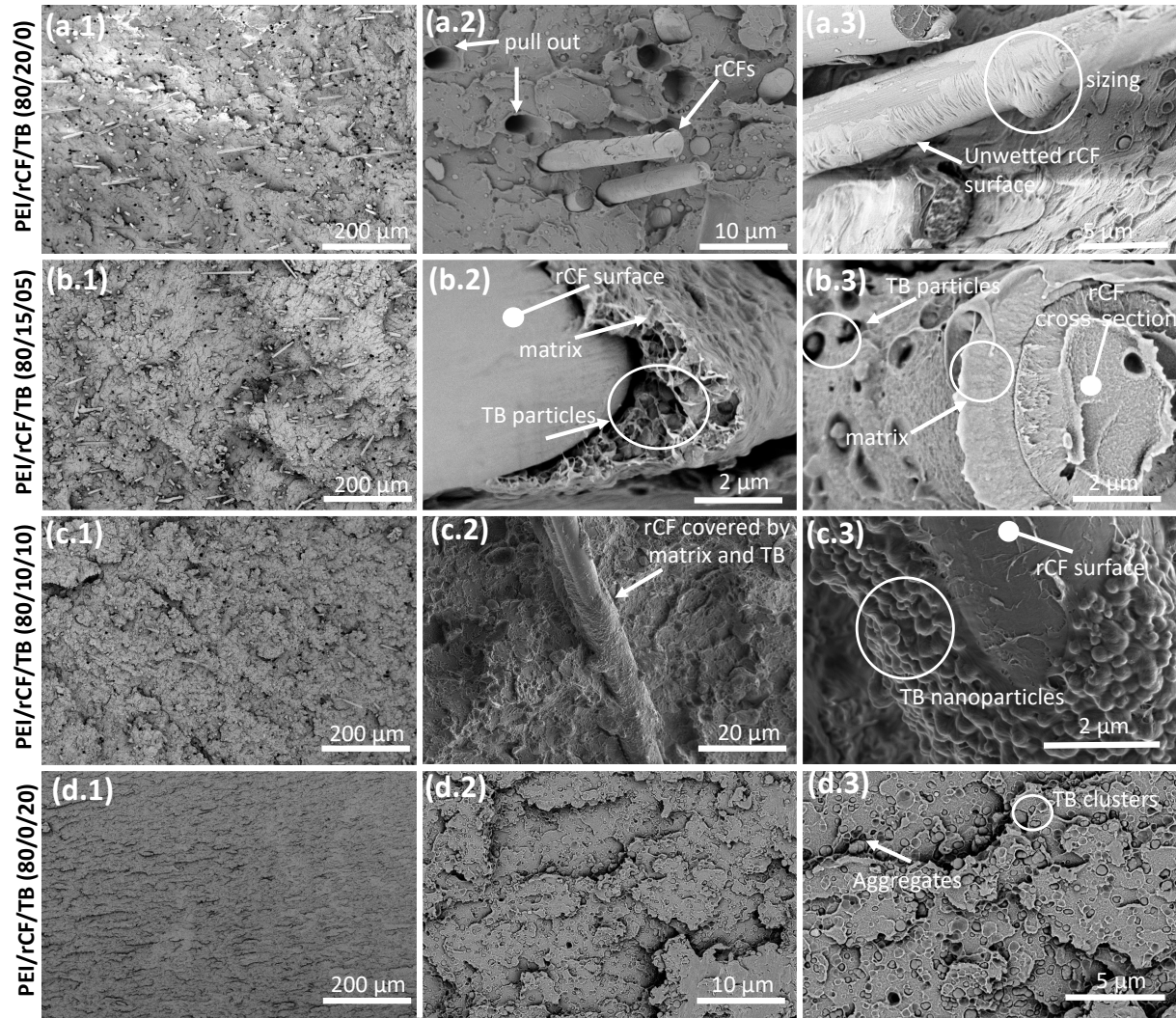


Figure 5.6 SEM images at three different magnifications of the fracture surfaces of the IM Izod impact specimens: (a.1-a.3) PEI/rCF/TB (80/20/00), (b.1-b.3) PEI/rCF/TB (80/15/05), (c.1-c.3) PEI/rCF/TB (80/10/10), (d.1-d.3) PEI/rCF/TB (80/00/20).

**Figure 5.7** shows SEM images of the fracture surfaces of FFF printed PEI composite specimens resulting from Izod impact testing. The SEM images correspond well with the micro-CT findings, revealing qualitative levels of porosity across all formulations. In **Figure 5.7(a)**, two different types of porosities were observed for composites containing rCF/TB (20/00). Intra-layer porosity has a relatively fine size ( $\sim 10\text{-}30\text{ }\mu\text{m}$ ). On the contrary, inter-layer porosity has a diamond-like shape with a larger size ( $\sim 50\text{-}100\text{ }\mu\text{m}$ ), which occurred as a characteristic of FFF printing during the deposition of layers from a circular shape printing nozzle. **Figures 5.7(b)** and **5.7(c)** present the fracture surface of specimens containing rCF/TB (15/05) and rCF/TB (10/10), respectively. Inter-layer and intra-layer porosities were observed on these surfaces as well, due to the presence of rCF.

However, the porosity level decreased when replacing the rCF with TB as the quantitative results reported in **Table 5.2**.

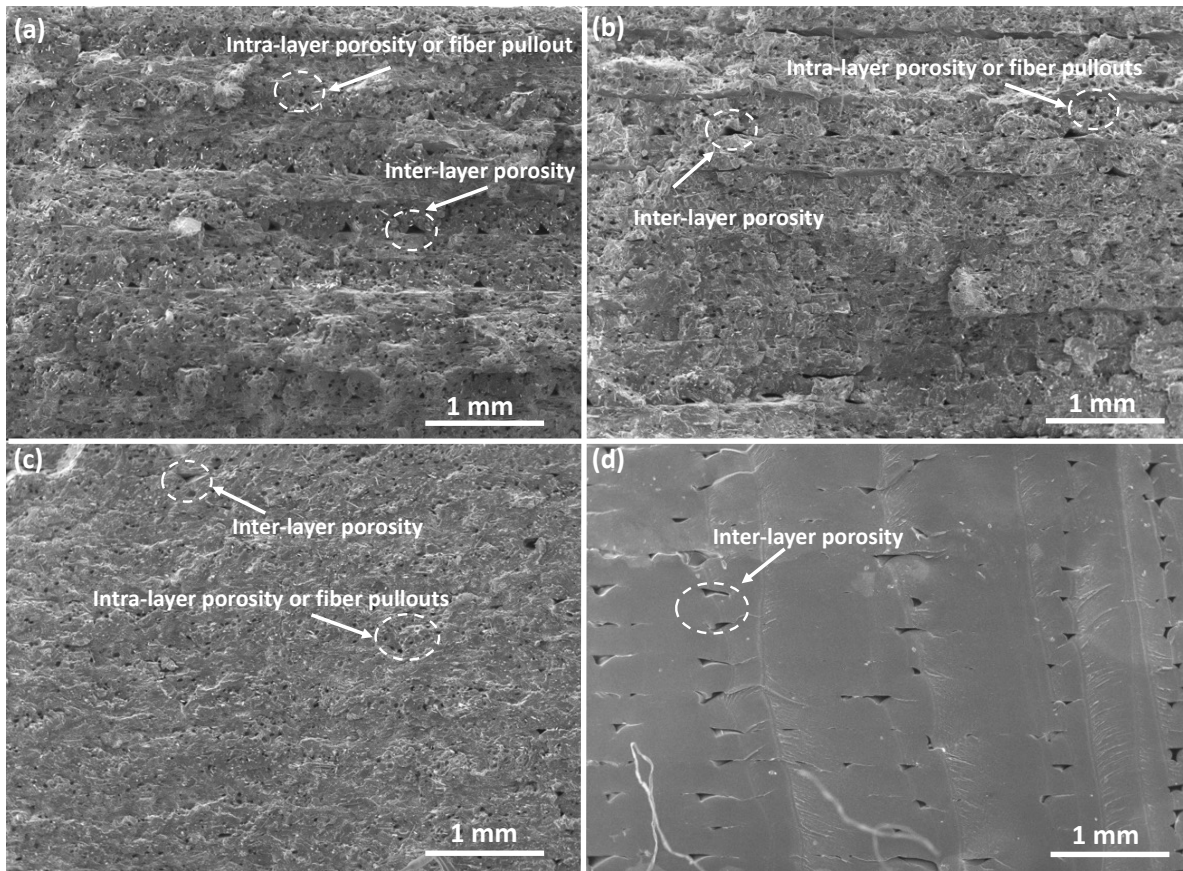


Figure 5.7 SEM images of the fracture surface of FFF printed impact specimens: (a) PEI/rCF/TB (80/20/00), (b) PEI/rCF/TB (80/15/05), (c) PEI/rCF/TB (80/10/10), (d) PEI/rCF/TB (80/00/20).

Finally, **Figure 5.7(d)** shows the fracture surface of composites containing rCF/TB (00/20). There is no intra-layer porosity in this case, while some inter-layer porosities are still present. Overall, the fracture surfaces of FFF printed composites with very low porosity content indicating efficient layer-to-layer adhesion for all formulations. The porosity observed is predominantly attributed to the presence of rCF, leading to the formation of intra-layer porosities. However, for the formulations without rCF, the porosity content remains significantly low (2.8 %), consisting of only inter-layer porosity due to the FFF printing process itself. The low porosity content that promotes layer-to-layer adhesion is expected to favor the mechanical performance of FFF printed parts, when compared to IM composites.

### 5.4.2 Mechanical properties of IM and FFF printed PEI composite specimens

**Figure 5.8** compares the TS and TM of the pure PEI and its composites. The solid bars represent the tensile properties of the IM specimens while patterned bars represent those of the FFF printed specimens. With the incorporation of 20 wt.% rCF, the TM of IM specimens increased from 3.20 GPa up to 6.18 GPa, and the TS increased from 74 MPa up to 103 MPa. Replacing rCF by TB resulted in the reduction of the TM and TS, when compared to the composite containing rCF/TB (20/00). For example, the TS of composites containing rCF/TB (15/05) and rCF/TB (10/10) reduced down to 88 and 82 MPa, respectively. The TS exhibited a 14.5 % reduction, and the TM decreased by 29.5 % for the composite containing rCF/TB (15/05), when compared to composites containing rCF/TB (20/00). However, this reduction was less pronounced for the composite containing rCF/TB (10/10), showing only a 6.8 % decrease in TS and 18 % reduction in TM, when compared to that observed for the composites containing rCF/TB (15/05). In composites containing rCF/TB (00/20), the TS was reduced down to 42 MPa. However, the TM exhibited an improvement, reaching 4077 MPa, when compared to the composite containing rCF/TB (10/10). The trend of tensile properties shows that gradual replacement of rCF with TB does not result in a significant reduction in mechanical properties as composites containing rCF/TB (15/05) and rCF/TB (10/10) almost show similar performance. As shown before in SEM images presented in the **Figure 5.6**, the TB particles attached to the surface of rCF seemed to indicate they helped to increase the surface area of rCF while promoting more bonding sites for the PEI matrix and proving further this positive effect on mechanical performance.

The FFF printed composites containing rCF/TB (20/00), rCF/TB (15/05), rCF/TB (10/10) and rCF/TB (00/20) have a TS of 70 MPa, 69 MPa, 64 MPa, and 42 MPa and a TM of 4.23 GPa, 4.20 GPa, 4.21 GPa, and 4.14 GPa, respectively. The FFF printed composites have comparable TM with those of the IM composites, while their TS is slightly lower. In the case of the composite containing rCF/TB (20/00), FFF printed parts exhibit a 32 % lower TS and a 31 % lower TM, when compared to IM specimens. For the composite containing rCF/TB (15/05), FFF printed parts show a 21 % lower TS and a 3.6 % lower TM than IM specimens. For the composite containing rCF/TB (10/10), FFF printed parts display a 22 % lower TS but an 18 % higher TM, when compared to IM specimens. Composite containing rCF/TB (00/20) show similar performance between IM and FFF printed parts when considering their respective CI values.



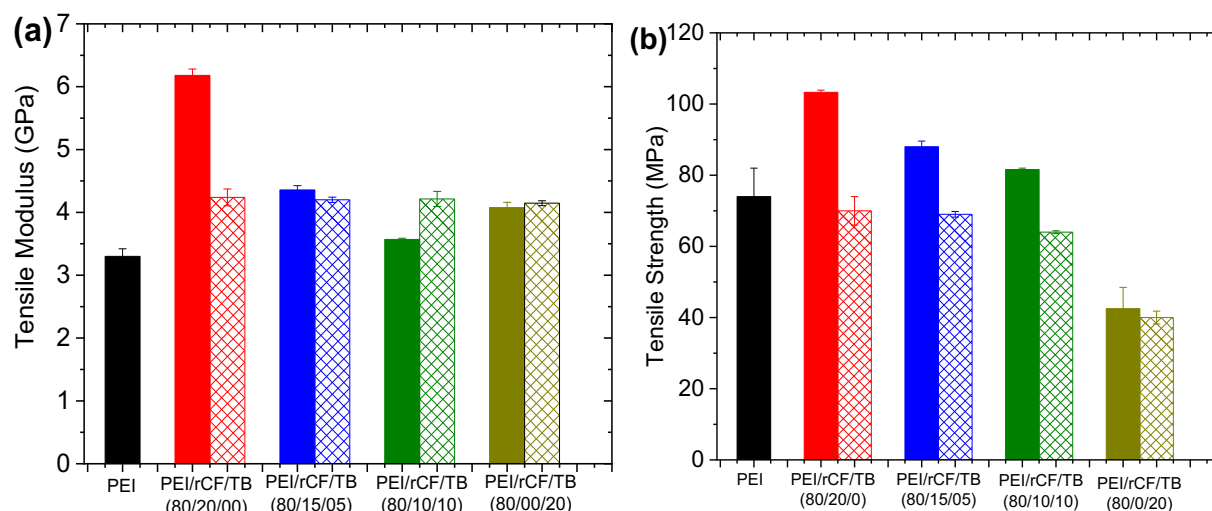


Figure 5.8 Tensile properties of injection molded (solid bars) and FFF printed (patterned bars) composites, showing (a) tensile modulus (TM) and (b) tensile strength (TS) of the various specimens. The results are presented as mean values and a CI of 95 % is provided based on a sample size (n) of 5.

The differences in TS and TM between IM and FFF printed specimens are mainly attributed to the presence of porosity and the fiber lengths and distributions. The reduction observed in mechanical properties of FFF printed specimens is more pronounced for the composite containing rCF/TB (20/00), primarily because of the higher porosity content (16.8 %), when compared to IM. Additionally, in IM parts, the average fiber length is longer ( $\sim 41 \mu\text{m}$ ), and the fibers are more aligned in injection flow direction, when compared to FFF printed parts. This difference is less pronounced for composite containing rCF/TB (15/05) since the total porosity content is reduced to 13.8 % and there is no significant difference in average fiber length and fiber deviation for IM and FFF printed parts. The FFF printed composite containing rCF/TB (10/10) shows slightly higher TM than IM parts, and this could be due to the longer average fiber length and lower fiber deviation along the Z axis with the relatively low porosity content (7.1 %). Composite containing rCF/TB (00/20), have similar mechanical performance for IM and FFF printed parts since porosity content is very low (2.8 %) for FFF printed parts. Finally, all composites have higher tensile modulus and tensile strength (except composite containing rCF/TB (00/20)) when compared to the IM neat PEI.

Table 5.3 Mechanical properties of injection molded and FFF printed PEI composites presented as mean values, and a CI of 95% is provided based on a sample size (n) of 5.

Specimen	Properties	PEI (0/0/0)	PEI/rCF/TB (80/20/00)	PEI/rCF/TB (80/15/05)	PEI/rCF/TB (80/10/10)	PEI/rCF/TB (80/00/20)
IM	TS (MPa)	74 (3.8)	103 (0.3)	88 (0.7)	82 (0.2)	42 (2.6)
	TM (GPa)	3.20 (0.02)	6.18 (0.10)	4.35 (0.07)	3.57 (0.02)	4.07 (0.08)
	IS (kJ/m <sup>2</sup> )	36.9 (5.5)	29.6 (1.2)	23.2 (1.5)	20.5 (1.0)	6.5 (0.3)
	FS (MPa)	127 (3.3)	158 (7.4)	154 (2.0)	127 (3.3)	70 (3.0)
	FM (GPa)	3.59 (0.04)	6.69 (0.30)	4.79 (0.07)	4.17 (0.07)	4.61 (0.06)
	HDT (°C)	177 (1.6)	200 (0.9)	194 (1.1)	186 (1.2)	184 (0.5)
FFF	TS (MPa)	-	70 (4.0)	69 (0.8)	64 (0.4)	40 (1.8)
	TM (GPa)	-	4.23 (0.13)	4.20 (0.04)	4.21 (0.12)	4.14 (0.04)
	IS (kJ/m <sup>2</sup> )	-	9.5 (1.0)	11.6 (1.8)	8.4 (2.7)	6.6 (2.7)
	FS (MPa)	-	112 (2.0)	99 (4.0)	64 (3.5)	84 (1.3)
	FM (GPa)	-	3.36 (0.07)	2.96 (0.06)	2.74 (0.04)	4.25 (0.07)
	HDT (°C)	-	199 (0.6)	197 (0.2)	186 (1.0)	184 (0.8)

**Table 5.3** presents the tensile, flexural, impact, and HDT characterization results for injection molded and FFF printed specimens. The incorporation of 20 wt.% of rCF increased the FS and FM of the IM PEI matrix from 127 MPa to 158 MPa and from 3.59 GPa to 6.69 GPa, respectively. The FS and FM relatively decreased when gradually replacing rCF by TB. The composites containing rCF/TB (15/05), rCF/TB (10/10), and rCF/TB (00/20) have FS and FM of 154 MPa, 127 MPa, 70 MPa and 4.79 GPa, 4.17 GPa, 4.61 GPa respectively. FFF printed PEI containing rCF/TB (20/00), rCF/TB (15/05), rCF/TB (10/10) and rCF/TB (00/20) showed FS of 112 MPa, 99 MPa, 64 MPa, and 84 MPa and FM of 3.36 GPa, 2.96 GPa, 2.743 GPa and 4.25 GPa, respectively. The FS and FM values of the FFF printed composites are relatively lower than those of the IM specimens most likely, as explained before, due to the presence of porosity. The FFF printed composites containing rCF/TB (00/20) has higher FS value and comparable FM value when compared to the IM specimens, as the porosity content is significantly low at 2.8 %.

The impact strength (IS) of neat PEI is 36.7 kJ/m<sup>2</sup>. It must be noted that some neat PEI specimens did not break during testing which were exempted from average IS calculation. The IS was reduced down to 29.6 kJ/m<sup>2</sup> for the composite containing rCF/TB (20/00). The replacement of rCF by TB further reduced the IS down to 20.5 kJ/m<sup>2</sup>. On the other hand, the IS of specimens containing rCF/TB (00/20) is 6.5 kJ/m<sup>2</sup>. The more brittle behavior of composites could be attributed to rCF and TB presence in which the effect of TB is more prominent. The presence of TB inhibits the molecular mobility of the PEI matrix, which would prevent energy absorption during crack propagation. FFF printed composites containing rCF/TB (20/00), rCF/TB (15/05), rCF/TB (10/10), and rCF/TB (00/20) showed an IS of 9.5 kJ/m<sup>2</sup>, 11.6 kJ/m<sup>2</sup>, 8.4 kJ/m<sup>2</sup>, and 6.6 kJ/m<sup>2</sup>, respectively.

The FFF printed composites exhibited similar IS performance when considering standard deviations, most likely due to the presence of porosities, which may suppress the effect of rCF and TB presence. Moreover, the FFF printed composites demonstrated lower IS when compared to the IM specimens. The lower IS values of the printed specimens could be attributed to the presence of porosity as the inter-layer and intra-layer porosity in FFF printed specimens could act as defects and stress concentration points which made printed composites more prone to crack propagation [37, 49]. It can be seen that the composite containing rCF/TB (00/20) with very low porosity has the same IS values as the IM specimens, trend which was also observed for the tensile properties.

Overall, the FFF printed composites have comparable mechanical performance, when compared to IM specimens due to efficient FFF printing parameters used to print the standard specimens that further resulted in low porosity contents. The SEM and micro-CT comprehensive and precise quantitative analysis on the morphology of developed PEI ULTEM 1040A composites allows us to better understand the link between their microstructure and their mechanical performance for IM and FFF printed parts.

### **5.4.3 Thermal resistance of IM and FFF printed PEI composite specimens**

The HDT values of IM neat PEI increased from 177 up to 200 °C for the composite containing rCF/TB (20/00), as shown in **Table 5.3**. Replacing the rCF by TB particles decreased the HDT down to 184 °C. The FFF printed PEI composites containing rCF/TB (20/00), rCF/TB (15/05), rCF/TB (10/10), and rCF/TB (00/20) have HDT of 199 °C, 197 °C, 186 °C, and 184 °C respectively. The HDT was evaluated when the tested specimens deflected by 0.25 mm under the applied load while increasing the temperature. The specimens containing 20 wt.% rCF, due to the rCF network inside the specimens, helped to support higher temperature before deflection than those containing partially or fully TB particles. The HDT is a material formulation characteristic regardless to the manufacturing methods and, as can be concluded, the HDT of FFF printed specimens and of IM specimens are comparable for the same formulation. Therefore, the service temperatures of the PEI ULTEM/rCF/TB composite parts made in FFF printing will be the equivalent to their corresponding parts made in IM process.

## 5.5 Conclusion

In this study, novel formulations of high temperature composites based on PEI ULTEM 1040A containing rCF and TB were for the first time developed, characterized, and analyzed. These novel composites were transformed through extrusion melt-process into filaments of a diameter of 1.75 mm with a high dimensional accuracy. Mechanical testing specimens were obtained in injection molding and, as well, in FFF printing using an open-source 3D printer equipped with a high-temperature closed chamber. The morphology, various mechanical performances, and thermal resistance of PEI reinforced with rCF and TB were evaluated and analyzed for both injection molded and FFF printed parts. The combination of rCF and TB particles revealed an excellent dispersion and distribution quality through the PEI matrix. Moreover, the incorporation of TB particles seems to have improved fiber-matrix adhesion, possibly due to similar carbon surface characteristics of rCF and TB particles, since SEM images showed that the surface of rCF was covered with the mixture of matrix and TB particles. FFF printed specimens disclosed a very low level of porosity, decreasing from 16.8 down to 2.8 % when rCF content was decreased from 20 down to 0 wt.% in the hybrid composites. At the incorporation of 20 wt.% of rCF, the tensile strength and modulus of injection molded specimens were enhanced from 74 MPa up to 103 MPa and from 3.20 GPa up to 6.18 GPa, when compared at pristine PEI. The tensile properties of FFF 3D printed composites were found to be similar to the injection molded specimens due to the relatively low inter-layer and intra-layer porosity contents. The substitution of rCF with TB appears to offset the decline in mechanical properties for certain formulations, such as composites containing rCF/TB (15/05) and rCF/TB (10/10) that shown similar performance. The FFF printed specimens based on these new materials present a good range of mechanical and thermal properties in terms of tensile, flexural, impact, and HDT results. These novel formulations of newly developed PEI ULTEM1040A/rCF/TB composites and hybrids are recommended for FFF 3D printing of interior parts for ground transportation and aerospace industries.

## CHAPTER 6      ARTICLE 2: CRYSTALLINITY, POROSITY, AND MICROSTRUCTURE OF POLYPHENYLENE SULFIDE COMPOSITE PARTS FABRICATED BY FILAMENT-EXTRUSION ADDITIVE MANUFACTURING

Dogan Arslan<sup>a,b</sup>, Mihaela Mihai<sup>b</sup>, Daniel Therriault<sup>a</sup>, Martin Lévesque<sup>a</sup>

a: Laboratory for Multiscale Mechanics, Department of Mechanical Engineering, Polytechnique Montreal, Montreal, QC., H3T 1J4, Canada

b: Advanced Manufacturing, Automotive, and Surface Transportation Research Center, National Research Council Canada, 75 de Mortagne, Boucherville, QC., J4B 6Y4, Canada

Submitted to Composite Part B: Engineering on October 07, 2024.

### 6.1 Abstract

In this study, polyphenylene sulfide (PPS) composites were developed, fabricated by different melt-processes, and characterized for their application in filament-extrusion of high-performance parts. Semi-crystalline PPS matrix was compounded with recycled carbon fibers (rCF), and thermal black (TB) particles, followed by injection molding (IM) and by extrusion of the compounded composites into filaments for Fused Filament Fabrication (FFF). The effect of rCF and TB contents on the microstructure, crystallization kinetic, and mechanical performance of the PPS composites were evaluated and analyzed. At the incorporation of 20 wt.% rCF, the tensile strength of IM specimens increased from 73 MPa up to 151 MPa and the tensile modulus increased from  $\sim 3.5$  GPa up to  $\sim 20$  GPa, respectively. FFF printed specimens with 20 wt.% of rCF showed a tensile strength of 86 MPa and a tensile modulus of 6 GPa, higher when compared to IM neat PPS. Differential scanning calorimetry (DSC) analysis was conducted on extruded pellets, IM, and FFF printed specimens to explore the crystallization kinetic of PPS composites. The analysis of DSC results revealed that the incorporation of rCF and TB significantly hindered the crystallization of PPS. The microstructural characterization of the PPS composites performed by scanning electron microscopy (SEM) and micro-computed tomography (micro-CT) provided quantitative results for porosity content, and of length distribution and deviation angle of rCF. These characterizations helped to analyze the mechanical performance of IM and FFF printed parts, and providing quantitative results to explain the differences in mechanical properties of specimens fabricated through the two methods.

## 6.2 Introduction

Polyphenylene sulfide (PPS) is a semi-crystalline thermoplastic polymer consisting of an aromatic ring connected to a sulfide atom that forms the basic unit of polymerization [69, 70]. PPS, as a function of its grade and its manufacturer, can present a tensile strength up to 90 MPa, a tensile modulus approximately 3.8 GPa [5]. Moreover, PPS is classified flame retardant due to its distinctive chemical configuration and its innate capacity to undergo charring upon exposure to an open flame [69]. The inherent properties of PPS gave rise to its particular use in parts manufacturing for aerospace and ground transportation applications. PPS-based composites have been successfully used in a number of aircraft components, including the main landing gear door, the rudders, the keel beams, and ailerons, all manufactured using conventional methods [110].

The PPS matrix has been modified with fillers, fibers, and other polymers to be used in a variety of industries [69, 111]. Recycled carbon fibers (rCF) are sourced from end-of-life composite products or manufacturing wastes and are considered being more environmentally responsible materials, including the benefits of cost-effectiveness, energy consumption, emissions reduction, and mechanical performance, when compared to virgin CF [16]. The rCF is priced at approximately 21 USD/kg, while virgin CF costs can go up to 66 USD/kg [101]. The rCF generally exhibits a similar modulus as virgin CF, while its tensile strength might be only 10 to 20 % below than of the virgin CF [16, 112]. On the other hand, thermal black (TB) is derived from the combustion of natural gas in the absence of the oxygen (no emissions) resulting in the production of one of the purest and cleanest carbon black grade from the industry, while being a low-cost material (~ 2 \$/kg) [16, 21, 24]. The PPS composite formulations developed and studied in this work are benefiting from the presence of these environmental-friendly materials, rCF, TB, and their combinations, while bringing cost reductions and increased performance, as well.

Fused Filament Fabrication (FFF) is an extrusion-based additive manufacturing (AM) technology that employs a thermoplastic material in the form of a filament and subjects it to controlled heating until it reaches its melting point. Then, the molten material is extruded through a nozzle enabling the layer-by-layer construction of a three-dimensional (3D) object [9, 10]. The mechanical performance of FFF printed composite parts depends, among many other parameters, on the innate matrix performance and its thermal behaviour, the filler and reinforcements types and concentrations, the 3D printing conditions, the porosity content, the fibers average length and

distribution, and, not the last, the layer-to-layer adhesion. FFF printed parts are reported to generally have lower mechanical performance than composite parts manufactured using conventional melt-processes (e.g., injection molding) due to specific defects induced by the extrusion-based 3D printing technology itself [48, 80]. Structural defects mainly consist of different types of porosity that emerge during FFF printing [113]. The presence of intra-layer and inter-layer porosities induces a reduction in toughness, strength, modulus, and fatigue performance of the FFF printed structures [49]. For the same specimen geometry and material, the tensile and flexural strengths of extrusion-based additive manufactured commercial PPS composites pellets reinforced with 50 wt.% of short carbon fiber were  $\sim 2$  and 3 times lower of that of injection molded specimens. The total volume of porosities was measured to be of 15.5 % in additively manufactured specimens while it was almost 0 % in the injection molded specimens [80].

In contrast to conventional melt-processes such as injection or compression molding, the FFF 3D printing operates under significant thermal variation conditions, such as fast cooling of the melt from the nozzle down to the deposition, of the deposited layers etc., phenomena that involve various heat transfer mechanisms [114, 115]. The cooling rate is affected by several factors, including the nozzle temperature, bed temperature, environmental temperature, layer thickness, and nozzle diameter [29, 116]. Depending on these factors, the cooling rate of the printed material can vary significantly and would attain a loss of temperature as rapid as 500 °C/s during the FFF printing [117]. The crystallinity content and morphology of the PPS composites are affected by distinct factors such as filler/reinforcement contents and non-isothermal processing environments [118-121]. The crystalline structure of PPS also plays an important role in the interfaces formed between sequentially FFF deposited layers, which holds significance for mechanical performance [29, 75, 116].

The crystal size and morphology of CF reinforced PPS composites fabricated through large scale extrusion-based AM were investigated [122]. The very rapid cooling rates inherent to the extrusion-based AM process were found to obstruct the innate PPS crystal growth, leading to a comparatively less ordered crystal structure, when compared to injection molding process. The isothermal crystallization characteristics of neat PPS and PPS composites incorporating different types of fibers were also investigated [123, 124]. It was found that the presence of fibers as reinforcements accelerates the crystallization rate. However, the resulting crystallinity content remains lower than that of the neat PPS. In another study, it was observed that the presence of CF had a minor impact

on the overall crystal growth mechanism in a PPS matrix, but it reduced the crystallinity content [125].

The existing studies on PPS material-extrusion 3D printing were done mainly on commercial filaments and pellets to investigate the effect of 3D printing parameters on the mechanical properties and crystallinity of printed PPS specimens. The effect of nozzle temperature, chamber temperature, and layer height on the mechanical properties of FFF printed parts were studied. It was found that increasing the nozzle temperature from 310 °C to 340 °C decreased the melt viscosity that helped the printing and led to tensile strength reaching 93 % of that of compression-molded counterparts [72]. The 3D printing temperatures variations were explored in terms of their impact on crystallinity and mechanical properties of PPS printed specimens. It was found that increasing the temperature of the nozzle from 320 up to 340 °C raised crystallinity from 23 % to 37 %, but it declined again to 33 % when the nozzle was set at 350 °C [76]. In another study, the impact of a post-processing temperature of 180 °C for 24 h on 3D printed neat PPS proved an important impact on the crystallinity content and mechanical properties. Heat-treated specimens achieved a tensile strength of 60 MPa, a modulus of 2.3 GPa, and 48.4 % of crystallinity, compared to untreated samples that showed lower values. The heat-treated specimens in ideal conditions reached 80 % of the tensile strength and 72 % of the tensile modulus of compression-molded PPS, indicating the important role of the crystallinity of printed parts on their mechanical performance [79]. Despite these existing studies done on commercial neat PPS and PPS composites filaments, no publication exists on the development of new formulations of PPS composites specially designated for FFF printing and on the effect of the FFF printing temperatures on the thermal behavior of PPS composites.

Therefore, investigating the relationship between the PPS composite formulations, the fast temperature variations encountered in FFF printing, and their combined effects on the crystallization behavior and crystallinity evolution of PPS, are of interest in understanding mechanical performance of PPS composite parts printed by FFF. The effect of microstructure, considering porosity, fiber length distribution, and crystallization kinetics on the mechanical performance of FFF printed composite parts made of rCF has been scarcely studied, especially for semi-crystalline PPS composites. This study investigates the in-process behaviour and the performance of PPS composite formulations and hybrids reinforced with rCF and combinations of rCF and TB nanoparticles, respectively, specifically designed for use in FFF 3D printing. A



framework has been created to understand formulation-process-performance relationships for injection molded (IM) and FFF printed PPS composite parts, where IM composites are considered as the benchmark with respect to FFF 3D printed composites. The framework encompasses an extensive analysis of PPS/rCF/TB composites, processed by IM and FFF 3D printing, in terms of their morphology and microstructure, crystallization kinetics, and mechanical performance that were comparatively used with the intent to bring a full understanding of the behavior of PPS composites when used in FFF additive manufacturing technology.

## **6.3 Materials and Methods**

### **6.3.1 Materials**

PPS Fortron 0214P1 grade in a pellet form was purchased from Celanese (Celanese Corporation, Fortron Industries LLC., Wilmington, NC, USA). Thermal Black (Thermax<sup>®</sup> N990, TB) particles were supplied by Cancarb Limited (Medicine Hat, AB, Canada). The TB spherical particles have an average size of 280 nm. Recycled short carbon fibers (re-Evo<sup>®</sup> HSC, Phenix 0.25) were purchased from Carbon Conversion (Lake City, SC, USA). According to the manufacturer, the rCF have an initial length of 6 mm, an average diameter of 4.9  $\mu\text{m}$ , and the sizing content ranges between 1.5 and 3.5 wt.%. The sizing type and chemistry are not disclosed by the manufacturer.

### **6.3.2 Melt-processing methods**

#### **6.3.2.1 Compounding**

The neat PPS and its composites were dried before each processing step (i.e., compounding, IM, filaments extrusion, and FFF printing) at 100 °C for 12 h. PPS pellets were compounded with rCF and TB by using a Bühler clamshell co-rotating twin-screw extruder (Bühler Group, Gupfenstrasse 5, Uzwil 9240, Switzerland). The temperature profiles of the extruder were set to incrementally rise from 280 °C to 330 °C, from the feeding zone to the die. PPS pellets, TB, and rCF were fed through separate feeders in the first zone of the extrusion line. The extruded composites were cooled down in the air and pelletized. The pellets were further used in the IM and filament extrusion. **Table 6.1** lists the five (5) PPS composite formulations studied in this work.

Table 6.1 Formulations of the extruded composites using a twin-screw extruder.

Formulation	PPS (wt.%)	rCF (wt.%)	TB (wt.%)
PPS	100	0	0
rCF/TB (20/00)	80	20	0
rCF/TB (15/05)	80	15	5
rCF/TB (10/10)	80	10	10
rCF/TB (00/20)	80	0	20

### 6.3.2.2 Injection molding (IM)

The compounded pellets were dried as specified before and then injection molded using a 34-ton Boy injection molding press (Boy Machines Inc., Exton, PA, USA). The injection barrel temperatures were set to incrementally rise from 280 °C to 330 °C with an injection pressure of 110 bar. Specimens were molded according to ASTM D638, ASTM D790, and ASTM D256 standards, corresponding to tensile, flexural, and unnotched Izod impact, respectively.

### 6.3.2.3 Filament extrusion

The composites pellets were dried at 100 °C for 12 h before their extrusion into filaments. **Figure 6.1(a)** shows filament spools of PPS reinforced with rCF/TB (20/00) and rCF/TB (10/10), respectively. The filaments were manufactured by using a filament-making extruder (Xcalibur, Noztek, Shoreham, England). The temperature profiles of the extruder were set to incrementally rise from 310 °C to 330 °C, from the feeding zone to the die, with a screw rotation speed of 25 rpm. The filaments were continuously monitored for a constant diameter of  $1.75 \pm 0.05$  mm, and a steady ovality by using a laser controlling system with 1200 scan/s along radial axes (Zumbach-ODAC18XY, Switzerland).

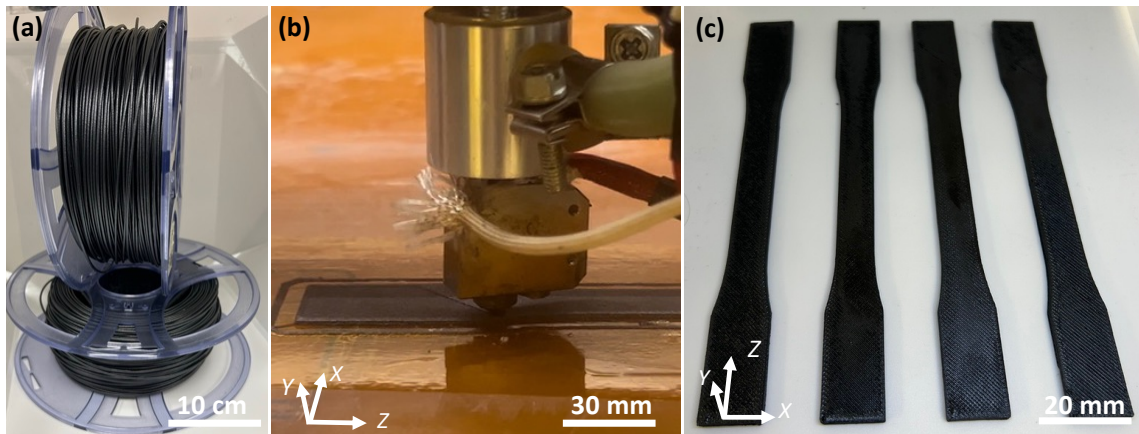


Figure 6.1 Images of: (a) PPS composite filament spools (top: PPS/rCF/TB (80/20/00) and bottom: PPS/rCF/TB (80/10/10)), (b) FFF printing of a Type-1 dogbone specimen, (c) FFF printed Type-1 dogbone specimens using filament PPS/rCF /TB (80/20/00).

### 6.3.2.4 Fused filament fabrication (FFF)

Simplify3D software (Simplify3D-4.1.2, Cincinnati, OH, USA) was used to slice the 3D models of the specimens on the flatwise position based on their shape as defined in the aforementioned ASTM standards. The approach chosen was to fabricate specimens having the same geometry by FFF and by IM, for comparison purposes. An open-source printer, AON-M2 (AON3D, Montreal, QC, CA), equipped with a 0.4 mm nozzle (350 °C), heated bed (160 °C), and a heating chamber (100 °C), was used to print the various specimens (**Figure 6.1(b) and 6.1(c)**). The specimens were printed relative to the longitudinal axis of the specimens with an in-plane raster angle of +45°/-45°, 16 successive 0.2 mm thick layers, a width of 0.48 mm, and an infill ratio of 100 %. The filaments were dried at 100 °C for 12 h before their FFF printing. These printing parameters were found to yield optimal mechanical properties after a number of preliminary printing trials where the purpose was to reduce the degree of anisotropy, to make the mechanical properties more consistent in different directions, and to reduce the porosity content.

## 6.3.3 Characterization methods

### 6.3.3.1 Differential scanning calorimetry (DSC)

Non-isothermal and isothermal tests of neat PPS and PPS composites were performed using a Q2000 DSC apparatus (TA Instruments, New Castle, DE, USA). For the non-isothermal analysis, the samples were first heated from room temperature up to 350 °C at a heating rate of 10 °C/min and dwelled for 5 min to completely remove their thermal history. They were then cooled down to 25 °C at a rate of 5 °C/min and reheated up to 350 °C at a rate of 10 °C/min. The glass transition temperature ( $T_g$ ), the temperature of crystallization ( $T_c$ ), and the melting temperature ( $T_m$ ) of the samples were extracted from the obtained curves. The crystallinity content ( $X_c$ ) was computed based on the enthalpy of crystal melting ( $\Delta H_m$ ) for the heating cycles and the enthalpy of crystallization ( $\Delta H_c$ ) during the cooling by using the equations (6.1) and (6.2):

$$X_c^{\text{heating}} = \frac{(\Delta H_m) \times 100}{w_{\text{PPS}} \Delta H_m^0}, \quad (6.1)$$

$$X_c^{\text{cooling}} = \frac{(\Delta H_c) \times 100}{w_{\text{PPS}} \Delta H_m^0}, \quad (6.2)$$

where  $w_{PPS}$  is the weight fraction of the PPS and  $\Delta H_m^O$  is the ideal heat of fusion of 100 % crystalline PPS, which was considered as 76.5 J/g [126].

**Figure 6.2** presents a combination of isothermal and non-isothermal cycles that was also applied to neat PPS and its composites to determine their crystallization kinetics, i.e., crystallinity formed under isothermal conditions and the corresponding crystallization half-time ( $t_{1/2}$ ). The samples were each heated from room temperature up to 350 °C at a heating rate of 10 °C/min, and dwelled for 5 min to completely remove the thermal history. The specimens were cooled down to temperatures of 190, 200, 210, 220, 230, 240, 250, and 260 °C at a rate of 70 °C/min and dwelled under isothermal conditions for 60 min. These eight (8) temperatures used for the isothermal steps were selected considering the optimal crystallization temperature during cooling of the PPS and its composites (observed in the range of 200 – 240 °C during the cooling cycles from previous non-isothermal analysis) but, as well, at the left and the right of these temperatures. Then, the samples were cooled down to ambient temperature at rate of 70 °C/min. These combinations of non-isothermal and isothermal steps were used with the intention to replicate the temperature variations that the PPS melt materials would encounter during their normal FFF printing. The final purpose was to understand the crystallization behaviors of PPS materials in thermal conditions variations as near as possible to their FFF printing. Finally, the specimens were heated up again to 350 °C at a rate of 10 °C/min to evaluate their total crystallinity.

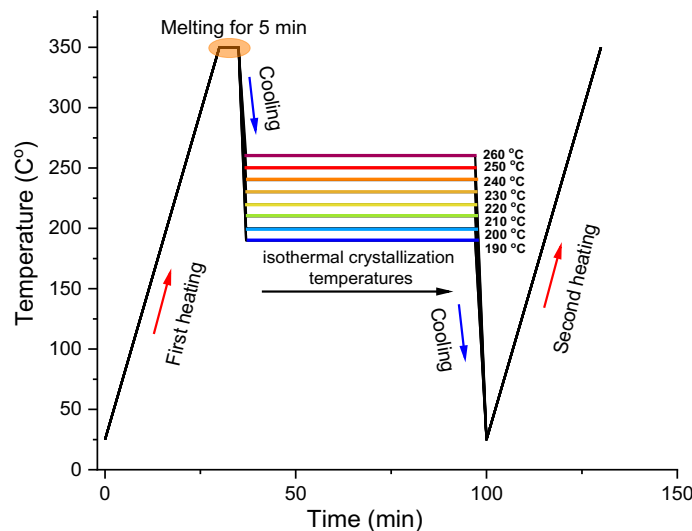


Figure 6.2 DSC plot illustrating the combination of isothermal and non-isothermal cycles applied to the studied PPS composites to observe their crystallization behaviors in thermal conditions variations mimicking the temperature variations met in FFF printing.

### 6.3.3.2 Avrami model

The Avrami's model was used to describe isothermal crystallization kinetics of PPS composites according to the equation (6.3):

$$X(t) = 1 - \exp(-k_a t^n), \quad (6.3)$$

where  $X(t)$  is the crystallization content as a function of time  $t$ ,  $k_a$  is Avrami's rate constant related to nucleation and crystal growth rate,  $n$  is Avrami's exponent related to the geometry of the formed crystals, and  $t$  is time. The Avrami's equation parameters can be computed by plotting a rearranged form of equation (6.3), as per the equation (6.4):

$$\log(-\ln(1 - X(t))) = \log k_a + n \log t. \quad (6.4)$$

The plot of the  $\log(-\ln(1 - X(t)))$  with respect to  $\log(t - t_0)$  is linear and yields the Avrami equation parameter of  $k_a$  and  $n$ . The crystallization half-time ( $t_{1/2}$ ) refers to the time at which the crystallinity of a composites reaches the half of its maximum crystallinity, which was calculated according to the equation (6.5):

$$t_{1/2} = \left(\frac{\ln 2}{k_a}\right)^{1/n}. \quad (6.5)$$

### 6.3.3.3 Morphology and microstructural analysis

Scanning electron microscopy (SEM) was used to observe the fractured surface of composite using a Hitachi-TM3030Plus SEM (Hitachi High-Tech Corporation, Hitachinaka, Japan) at a 15 kV accelerating voltage. A coating of 20 nm of chromium was applied on the surface of the specimens.

X-ray microtomography (micro-CT) was carried out to observe the porosity and the rCF orientation and length with a Zeiss XradiaTM 520 Versa X-ray computed tomography system (Carl Zeiss Microscopy GmbH, Jena, Germany). The applied source voltage and power were 50 kV and 4 W, respectively, with a 10× objective without filter, for an exposure time of 20 s. **Figure 6.3** shows a schematic representation of the method for measuring the porosity and the fibers length distribution for IM and FFF printed dogbone specimens. Only untested dogbone specimens were analyzed by micro-CT since the size and content of porosity can be affected during mechanical testing. The scan was first applied to the entire cross-section for observing the inter-layer porosities. Then, a small portion FFF printed part, that includes only a few layers were isolated by cutting and

polishing excessive layers for a high-resolution micro-CT scan which has a field of view (FOV) of 900  $\mu\text{m}$ . Similarly, for IM specimens to accurately represent the distribution of fibers, samples with a thickness and width of  $\sim 1$  mm were extracted from an area between the core and shell regions, approximately 0.3 mm away from the skin and mid-plane, in the IM specimens for micro-CT analysis. The OpenFiberSeg tool was used to segment individual rCF and determine porosities (inter-layer and intra-layer) by using high-resolution micro-CT scan data [107]. This tool allowed to label the porosity regions and to segment the rCF. The computation of fiber length distributions and orientations was achieved by treating a dataset including up to 15,000 individual fibers. Moreover, the average aspect ratio which refers to ratio of the fiber length to its diameter was computed from the data of fiber length distribution by considering average rCF diameter of 4.9  $\mu\text{m}$ . The obtained results provided insights into the effect of the used melt-processing on the porosity and fiber length and orientation distributions values.

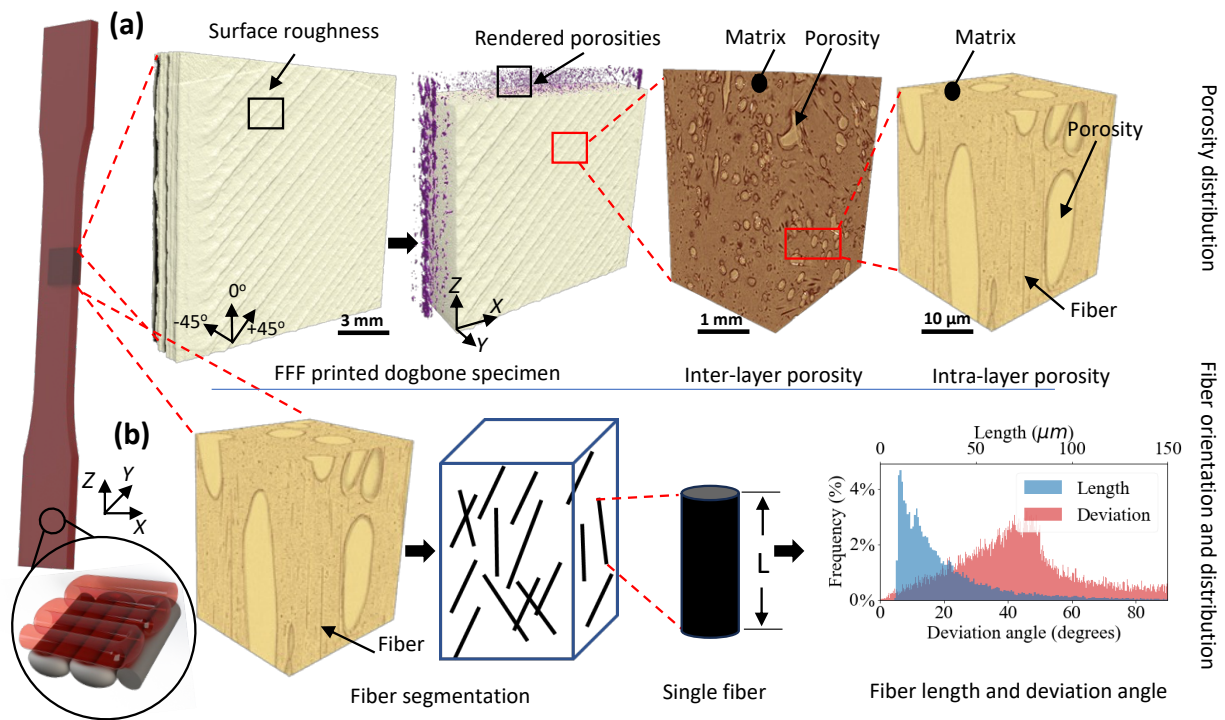


Figure 6.3 Micro-CT procedure to assess porosity and fiber distribution for IM and FFF printed dogbone specimens: (a) inter-layer porosities were measured from scans of the entire cross-section of dogbone specimens, followed by higher resolution scans for intra-layer porosities. The porosities, matrix and fibers are highlighted with arrows. (b) rCF were tracked and labeled by using OpenFiberSeg software, allowing for the computation of fiber length distributions and deviation angles from the extrusion direction.

### 6.3.3.4 Mechanical characterization

Tensile and flexural testing specimens were manufactured by IM and FFF printing for each PPS composite formulations. The testing was carried out according to the ASTM D638 and the ASTM D790 standards using an MTS Insight electromechanical testing machine (MTS Systems, Eden Prairie, MN, USA) equipped with a 50 kN load cell. The tensile tests were done with a crosshead speed of 5 mm/min and the flexural tests were done using a support span of 105 mm with a crosshead speed of 2.6 mm/min. Five (5) specimens for each formulation were tested and the mean values and their confidence intervals (CI) of 95 % are reported for tensile modulus (TM), tensile strength (TS), flexural modulus (FM), and flexural strength (FS).

The Izod impact strength was evaluated with a ZwickRoell impact device (ZwickRoell LP, Kennesaw, GA, USA). The unnotched specimens were obtained by IM and FFF printing. The tests were performed according to the ASTM D256 using a 2 kg hammer. At least eight (8) specimens from each formulation were tested. Before tensile, flexural, and impact testing, all the specimens were conditioned at 23 °C, 50 % RH for at least 40 hours.

## 6.4 Results and Discussion

### 6.4.1 Crystallization kinetics of PPS and its composites

#### 6.4.1.1 Non-isothermal behaviors

**Figure 6.4** shows DSC thermograms for the cooling cycles and second heating cycles of compounded pellets of neat PPS, PPS composites, and PPS hybrids. The first heating cycles are not reported here because they were very similar to those of the second heating cycles. **Figure 6.4(a)** shows the cooling cycles applied after a 5 min dwell at 350 °C, that was meant to melt all existing crystals and erase the thermal history. The neat PPS exhibited a  $T_c$  of 239.5 °C. The rCF/TB (20/00), rCF/TB (15/05), rCF/TB (10/10), and rCF/TB (00/20) composites exhibited a  $T_c$  of 233.9, 240.3, 241.5 °C, and 225.1 °C, respectively. These values show that the incorporation of 20 wt.% of rCF slightly decrease the  $T_c$  by 6 °C while the presence of 20 wt.% TB particles shifted the  $T_c$  to lower temperatures, by 15 °C. The 20 wt.% TB presence seems to modify the crystallization behaviour of the PPS in a more important manner than the 20 wt.% rCF. TB has nanometric dimensions ( $\sim 280$  nm), much lower than the rCF dimensions (4.9  $\mu\text{m}$  in diameter), and, at the same 20 wt.% concentration in PPS, the number of TB particles is much more important than the

number of rCF, while considering that they have similar densities. It seems that TB particles would impede the PPS molecular chains mobility, therefore their crystallization, more than rCF. Surprisingly, the two hybrids containing rCF/TB (15/05), rCF/TB (10/10) presented  $T_c$  very similar to PPS a slightly higher. These hybrid combinations seem to not affect in an important way the crystallizing of PPS during the cooling. This is due, possibly, to a potential TB-rCF synergism explained by their common C-structures that brought them together and reduced the number of nucleation sites.

Neat PPS presented a crystallinity content of 71.7 % during cooling. PPS composites shown crystallinity contents of 62.5, 58.3, 61.3, and 56.9 % for the rCF/TB (20/00), rCF/TB (15/05), rCF/TB (10/10), and rCF/TB (00/20) composites, respectively. Globally, the incorporation of rCF and TB particles slightly hindered the PPS matrix's ability to crystallize as indicated by a lower  $T_c$  and lower crystallinity levels achieved during the cooling. The lower crystallinity was observed, as expected, for PPS containing rCF/TB (00/20).

**Figure 6.4(b)** shows the second heating cycles of neat PPS and its composites. The absence of crystallization peaks suggests that the PPS matrix was already fully crystallized during the previous cooling cycles (**Figure 6.4(a)**). Therefore, the PPS composites proved to be able to completely crystallize rapidly, using a cooling rate of 5 °C/min. Consequently, all crystalline structures formed during cooling cycles were melted in this heating cycle, with a similar calculated crystallinity content.

The  $T_m$  of neat PPS and rCF/TB (20/00), rCF/TB (15/05), rCF/TB (10/10), and rCF/TB (00/20) composites were found to be similar, e.g., 281.7, 280.7, 282.5, 281.9, and 279.8 °C, respectively. This similar  $T_m$  values possibly indicate that the presence of rCF, rCF/TB and TB did not significantly change the type of crystal structure and growth with respect to the cooling rate applied during the cooling cycles [125].

This non-isothermal study suggests that the PPS composites achieved their full-crystallinities during a cooling process of 5 °C/min and their thermal behaviours were fingerprinted by different rCF and TB loadings and their combinations.



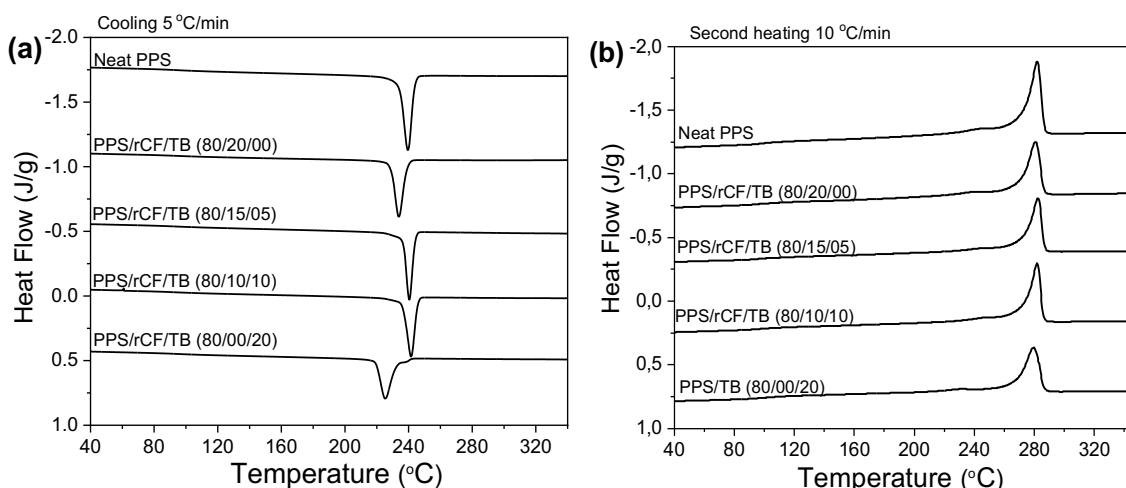


Figure 6.4 Non-isothermal DSC curves of cooling and second heating cycle in which the heat flow is given with respect to increasing temperature (a) exothermic crystallization peaks during cooling, (b) endothermic melting peaks during second heating cycle.

#### 6.4.1.2 Isothermal crystallization kinetics of PPS and its composites

**Figures 6.5(a) and 6.5(b)** present DSC thermograms of isothermal steps done at temperatures of 190 °C to 260 °C and their subsequent heating cycles. The heat flow was plotted as a function of time for isothermal steps and as function of temperature for non-isothermal heating steps. The plots were provided only for the rCF/TB (20/00) composites for conciseness. **Table 6.2** reports all quantitative data extracted from isothermal and heating steps for all formulations, including the crystallinity content computed from isothermal curves ( $X_{c-iso}$ ), crystallization half time ( $t_{1/2}$ ), Avrami index ( $n$ ), and melting temperatures ( $T_{m1}$  and  $T_{m2}$ ).

In **Figure 6.5(a)**, the exothermic crystallization peaks were not observed for the 190 °C and 200 °C isothermal steps. However, in **Figure 6.5(b)**, the minor endothermic melting peaks,  $T_{m1}$ , observed at 200.5 and 210.5 °C during the heating cycles, would suggest that some very rapid crystallization possibly occurred during the 70 °C/min cooling, while the material was passing rapidly by its optimal crystallization temperatures, e.g., ~ 240 °C, before reaching the isothermal conditions of 190 °C and 200 °C. On the other extreme, for the isothermal at 260 °C, also the isothermal crystallization is not present on the curve. In this case, 260 °C is above the optimal crystallization temperature and gave a high mobility to macromolecular chains and inhibited their isothermal crystallization for the 60 min of the isothermal step. A minor melting peak  $T_{m1}$  at 267.8 °C is still observed in **Figure 6.5(b)** and it might be explained by a rapid crystallization that happened after the 60-min isothermal at 260 °C while the material is cooling down at -70 °C/min

while passing through the optimal crystallization temperature. Two different melting peaks,  $T_{m1}$  and  $T_{m2}$ , were also observed during the heating cycles applied after the isothermal treatments at 210, 220, 230, 240, and 250 °C. The lower melting peak ( $T_{m1}$ ) shifted to higher temperatures and approached to the main melting peak ( $T_{m2}$ ) as the temperature of the isothermal step increased. As can be observed in the **Table 6.2**, the values of  $T_{m1}$  and  $T_{m2}$  did not show variations in respect to the PPS material formulation but varied only as a function of the temperature of the isothermal step. For example, after isothermal steps at the temperature of 190 °C,  $T_{m1}$  and  $T_{m2}$  are approximately 201 °C and 283 °C, of 220 °C  $T_{m1}$  and  $T_{m2}$  are approximately 230 °C and 283 °C, etc., for all PPS formulations.  $T_{m2}$  remained the same at 283 °C for all testing conditions and it is the normal melting temperature of the pure PPS (see **Figure 6.4(b)**). However,  $T_{m2}$  shifted up to 288 °C when the isothermal crystallization temperature was 260 °C. The two different melting temperature suggests that a lower isothermal condition may result in the formation of smaller and less perfect crystal structures with differing average crystal sizes that melt at lower temperatures ( $T_{m1}$ ). However, with increasing temperatures, there is more time for molecular mobility and rearrangement, which resulted in more uniform and larger crystal structure which melts at higher temperatures ( $T_{m2}$ ) [127, 128].

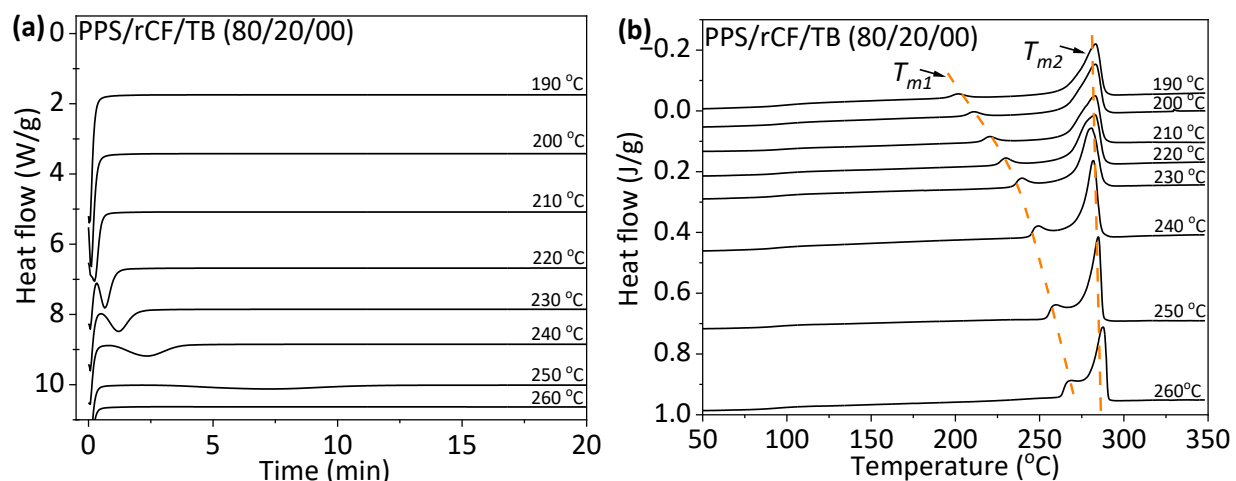


Figure 6.5 DSC plots from the combination of isothermal and non-isothermal DSC procedure show crystallization behavior of PPS/rCF/TB (80/20/00) for different isothermal conditions: (a) exothermic crystallization peaks during isothermal steps for different isothermal crystallization temperatures, (b) endothermic melting peaks during heating cycle after isothermal steps.

The Avrami's model was used to theoretically explain the observation of different melting peaks during heating cycles. The computation of Avrami's constant  $n$  allows to appreciate the mechanism of nucleation and the geometry of growth. A values of  $n$  ranging from 0 to 1 are typical of 1D

growth, values ranging from 1 to 2 are typical of 2D growth, while values of  $n$  ranging from 2 to 4 are typical of 3D growth [129].

**Table 6.2** presents the computed values of the Avrami's exponent,  $n$ , and the melting temperatures for all the studied PPS formulations. The pristine PPS presents  $n$  values between  $\sim 2.6$  up to  $\sim 3.7$ , very similar to the  $n$  values calculated for all the PPS composite formulations, e.g., from  $\sim 2.1$  to 3.8. Therefore,  $n$  value was in between 2 and 4 for the PPS composites. It should be concluded that all studied materials presented the typical pristine PPS 3D growth of the crystals and the presence of rCF and TB did not change this 3D growth. The value of  $n$  slightly increased with the isothermal crystallization temperature used during the 60 min of isothermal crystallization, which suggests that the higher temperatures for crystallization facilitate the 3D crystal growth due to providing higher molecular mobility and time for crystal formation. This was proven by the increment of crystallinity content with the temperature used in the isothermal step. An exception is the decrease of the crystallinity content obtained for the 260 °C isothermal step, for all the formulations. At this very high temperature, superior to the optimal crystallization temperature of PPS composites, induced a higher mobility than necessary for the macromolecular chains and decreased their speed of crystallization at such high temperature.

The crystallization half time with respect to crystallinity content for different isothermal steps were computed for each formulation. Neat PPS has a  $t_{1/2}$  of 0.15 min for  $X_{c-iso}$  of 29.4 %, evaluated from the isothermal curve obtained at 210 °C. The  $t_{1/2}$  increases up to 13.8 min for  $X_{c-iso}$  of 42.7 % with increasing isothermal crystallization temperature up to 260 °C. The rCF/TB (20/00) composites have a longer  $t_{1/2}$  of 0.29 min for  $X_{c-iso}$  of 35.1 % at 210 °C, when compared to neat PPS. The  $t_{1/2}$  of rCF/TB (20/00) increases up to 36.4 min for  $X_{c-iso}$  of 41.6 % with increasing temperatures up to 260 °C. It seems that incorporating rCF reduced the molecular mobility which resulted in longer crystallization half time with respect to relatively similar crystallinity content. The rCF/TB (15/05), rCF/TB (10/10), and rCF/TB (00/20) composites follow the same trend. Replacing rCF with TB reduced the  $t_{1/2}$  by 30-40 % in the rCF/TB (15/05) and rCF/TB (10/10) composites at temperature ranges of 210-260 °C, when compared to rCF/TB (20/00) composites. On the contrary, the rCF/TB (00/20) composites have relatively higher  $t_{1/2}$  at temperatures ranging from 210 to 260 °C, when compared to rCF/TB (20/00) composites. It seems that the nucleating effect of TB particles are outweighed by restricted molecular mobility due to the significantly increasing number of TB particles (see **Figure 6.5(a)**). The incorporation of rCF and TB reduced the crystallization rate of

PPS matrix in the range of 1 to 2-fold at an isothermal crystallization temperature of 210 °C. The crystallization rate of PPS matrix reduced  $\sim 100$ -fold when isothermal crystallization temperature was 260 °C. It seems that the effect of isothermal crystallization temperature is more prominent than the effects of rCF and TB in terms of crystallization half time and crystallinity content.

It is important to observe as well from the **Table 6.2** and **Figure 6.5(a)**, that the highest crystallinities were developed during 3 isothermal steps, e.g., the ones at 230, 240, and 250 °C. The corresponding crystallinities were evaluated in the range  $\sim 42$  to  $\sim 59$  %. These are high contents of crystals formed during short times of  $0.35 \times 2$  up to  $5 \times 2$  minutes. One exception can be observed, e.g.,  $19 \times 2$  minutes for PPS rCF/TB (00/20) composites, that needs more time to fully crystallize because the high number of TB particles. When considering the thermal dynamic of FFF printing process, this important crystallization steps would start immediately after the deposition of a composite melt layer on an already deposited layer. When the environmental printing temperature and the temperature of the two successive layers that have just come into contact are at least 230 - 240 °C or higher, a significant crystallization phenomenon will occur within and through two successive layers. Those can be considered ideal FFF temperatures that will help to increase the PPS composites layers adhesion.

The crystallization kinetic results yield insights on the crystallization mechanism during FFF printing, in which crystallization kinetics are expected to affect the layer-to-layer adhesion and mechanical properties of printed parts. The isothermal printing temperature (chamber temperature) should be adjusted based on crystallization kinetics to allow adequate inter-layer adhesion while the molecular mobility of the amorphous phase is still dominant [130]. Isothermal crystallization analysis conducted in this work at temperatures ranging from 190 °C to 260 °C suggest that the printing chamber temperature of 100 °C used in this study seems to be insufficient for adequate PPS composite crystallization. Therefore, a steady temperature of  $\sim 240$ -250 °C of the printing environment and of printed PPS composites, for times between 1 to 40 minutes, would significantly contribute to layers adhesion and on improving mechanical properties.

Table 6.2 Crystallinity content during isothermal step ( $X_{c-iso}$ ), crystallization half-time ( $t_{1/2}$ ), Avrami's parameter ( $n$ ), and melting temperature ( $T_{m1}$ ,  $T_{m2}$ ) data obtained from the combination of isothermal and non-isothermal DSC procedure for each formulation. The  $X_{c-iso}$ ,  $t_{1/2}$ , and  $n$ , were computed from isothermal curves, while  $T_{m1}$  and  $T_{m2}$  were obtained from the data for heating cycle after isothermal steps.

Isothermal crystallization temperatures (°C)		190	200	210	220	230	240	250	260
PPS	$X_{c-iso}$ (%)	-	-	29.4	32.1	45.3	52.2	56.6	42.7
	$t_{1/2}$ (min)	-	-	0.15	0.25	0.35	1.15	3.15	13.8
	$n$	-	-	2.63	2.65	3.18	3.56	3.59	3.74
	$T_{m1}/T_{m2}$	200.5/ 283.4	210.5/ 283.2	219.8/ 283.0	230.0/ 282.6	238.6/ 281.6	248.8/ 282.1	257.6/ 284.9	267.8/ 288.0
PPS/rCF/TB (80/20/00)	$X_{c-iso}$ (%)	-	-	35.1	37.4	45.8	51.2	55.3	41.6
	$t_{1/2}$ (min)	-	-	0.29	0.40	0.75	1.59	5.26	>30
	$n$	-	-	2.01	2.56	2.71	2.84	3.04	3.22
	$T_{m1}/T_{m2}$	201.0/ 283.2	211.0/ 283.3	220.0/ 283.3	229.5/ 283.0	239.0/ 280.8	248.8/ 281.9	258.3/ 285.0	268.0/ 287.8
PPS/rCF/TB (80/15/05)	$X_{c-iso}$ (%)	-	-	29.9	36.8	48.8	49.4	55.3	48.3
	$t_{1/2}$ (min)	-	-	0.16	0.22	0.35	0.93	3.45	21.4
	$n$	-	-	2.38	2.4	2.58	3.19	3.31	3.83
	$T_{m1}/T_{m2}$	200.7/ 282.7	210.0/ 283.0	220.0/ 283.0	230.0/ 282.6	239.3/ 281.3	249.0/ 282.3	258.5/ 284.5	268.0/ 287.8
PPS/rCF/TB (80/10/10)	$X_{c-iso}$ (%)	-	-	32.8	30.2	41.1	49.3	52.8	43.5
	$t_{1/2}$ (min)	-	-	0.20	0.22	0.49	1.28	4.86	23.8
	$n$	-	-	2.27	2.53	2.66	2.81	3.14	3.77
	$T_{m1}/T_{m2}$	200.0/ 282.7	210.5/ 283.0	220.0/ 283.0	230.0/ 282.1	239.0/ 280.6	248.8/ 282.0	258.3/ 284.7	268.0/ 287.6
PPS/rCF/TB (80/00/20)	$X_{c-iso}$ (%)	-	-	28.9	35.6	43.5	49.7	59.4	-
	$t_{1/2}$ (min)	-	-	0.22	0.57	1.46	4.97	19.3	>30
	$n$	-	-	2.55	2.69	2.66	2.77	2.96	-
	$T_{m1}/T_{m2}$	201.0/ 283.0	211.0/ 283.0	215.0/ 283.0	230.0/ 282.0	239.0/ 281.0	246.8/ 282.0	258.8/ 284.3	None/ 283.8

#### 6.4.1.3 Crystallinity of IM and FFF printed PPS and its composites

**Table 6.3** encloses the heat enthalpy, the crystallinity content, and the melting temperature values obtained from the first heating cycle for the FFF printed and IM dogbone specimens. The purpose of this DSC test was to evaluate how the thermal dynamic encountered by the materials during both the FFF printing and injection molding processes would fingerprint the thermal behaviors of PPS/rCF/TB composite parts. The IM neat PPS exhibits 93.5 % crystallinity, while the crystallization content for IM composite specimens was found to be lowered down to 40 %, 40.6 %, 42.4 %, and 37 % for the rCF/TB (20/00), rCF/TB (15/05), rCF/TB (10/10), and rCF/TB (00/20), respectively. The crystallinity content of the FFF printed rCF/TB (20/00) composite was found to be 31.1 %, lower when compared to 40 % observed for its corresponding injection molded specimen. The gradual replacement of rCF by TB kept the crystallinity contents at relatively similar

lower values, e.g., of 34.1 %, 36.2 %, and 33.3 % for the FFF printed rCF/TB (15/05), rCF/TB (10/10) and rCF/TB (00/20) composites, respectively. These seems to indicate that the thermal dynamic encountered in injection molding would favor the crystal formation in PPS composites more than the thermal dynamic specific to FFF process.

In the process of injection molding, the PPS composite melt having a temperature of 320 - 330 °C in the barrel was injected using a high injection speed and high pressure into a heated mold at 140 °C and kept there for 5 seconds. This resulted in the orientation of the melt flow and of the macromolecular chains along the injection direction, the mold walls. The process encountered during IM promotes the pure PPS and PPS composites crystallization, but still limited by temperature and time when compared to higher crystallinity contents obtained during 60 minutes iso-thermal steps (**Table 6.2**). A different temperature dynamic takes place in the FFF process, where the temperature difference of approximately 200 - 250 °C could be between the nozzle (at 350 °C) and the deposition plane (possibly between 100 - 160 °C). This represents a very short distance, as less as 5 to 7 mm. This important cooling gradient may support the lower crystallization contents calculated for FFF printed part when compared to IM ones. The more severe cooling rates during FFF printing brings evidence for a lower crystal formation in FFF printed parts.

To further demonstrate that is a remaining crystallization capacity of PPS composites after their FFF processing, the FFF printed dogbones containing rCF/TB (20/00) were annealed for 12 h at 235 °C in a vacuum oven. The annealing temperature was selected based on the  $T_c$  during cooling of the composite containing rCF/TB (20/00), which was presented in Section 6.4.1.1. The crystallinity content of the FFF printed samples increased from 31.1 % up to 58 % after annealing. The crystallization of PPS composites occurred in the range of 225-240 °C during cooling, depending on rCF and TB contents. The cooling rates in FFF 3D printing could reach several hundred degrees per second, while the critical cooling rate of PPS was reported to be 40 °C/s [75, 119]. Considering the fast-cooling rates of PPS composites, after their melting in the printer extruder and passing through a heated nozzle at 350 °C, down to the heated plateau at 160 °C and the heated chamber at 100 °C, there is not enough time for composites to complete their crystallization [131, 132]. The experimentally acquired crystallinity content values demonstrate that the PPS composites require a much higher temperature than that encountered in the FFF printer heating chamber, and in the FFF process in general. For the PPS composites, as discussed before (**Table 6.2** and **Figure 6.5(a)**), a temperature of 240 - 250 °C of their melt depositions and of layers

already deposited would be necessary to properly fully crystallize these composites, to fine-tune the formation of the crystals ideally after the layer deposition, to further help the crystal formation in between two successive layers and, therefore, to increase the layer-to-layer adhesion and the mechanical performance of PPS composites FFF parts.

Table 6.3 Heat enthalpy, crystallinity content, and melting temperature data obtained from the first heating DSC thermograms of the PPS composite samples for FFF printed and IM dogbone specimens.

Formulations	IM			FFF printed		
	$\Delta H_m$ (J/g)	$X_m$ (%)	$T_m$ (°C)	$\Delta H_m$ (J/g)	$X_m$ (%)	$T_m$ (°C)
PPS	71.0	93.5	298.7	-	-	-
PPS/rCF/TB (80/20/00)	24.5	40.0	280.1	19.1	31.1	281.9
PPS/rCF/TB (80/15/05)	24.9	40.6	281.6	21.0	34.3	282.6
PPS/rCF/TB (80/10/10)	25.9	42.4	282.1	22.2	36.2	281.7
PPS/rCF/TB (80/00/20)	22.6	37.0	282.5	20.4	33.3	282.1
PPS/rCF/TB (80/20/00) annealed at 235 °C	-	-	-	35.5	58.0	282.9

## 6.4.2 Microstructural characterization of PPS composites

### 6.4.2.1 SEM and micro-CT analysis of PPS composite filaments

**Figures 6.6(a.1) - (d.1)** show the SEM cross-section images of the composite filaments that were fabricated by extrusion with a uniform diameter of 1.75 mm. The uniformity of the filament diameter enhances printing quality by limiting extruded volume variation during FFF printing. Moreover, it can be seen that the incorporation of rCF comes along with porosity presence, which could be due to the degradation of their sizing materials during the melt-processing [49, 108]. **Figures 6.6(a.2) - (d.2)** illustrate micro-CT images of the composite filaments obtained with the purpose to evaluate the porosity ratio in the filaments. The rCF/TB (20/00) composites presented 9.6 (1.6) % of porosity. Porosity content was slightly reduced down to 8.5 (0.9) % and 6.6 (1.2) % for the rCF/TB (15/05), and rCF/TB (10/10) composites, respectively. No significant porosity was observed inside the rCF/TB (00/20) composite filaments. These observations suggest that the porosity content of the filaments declined when the content of rCF decreased.

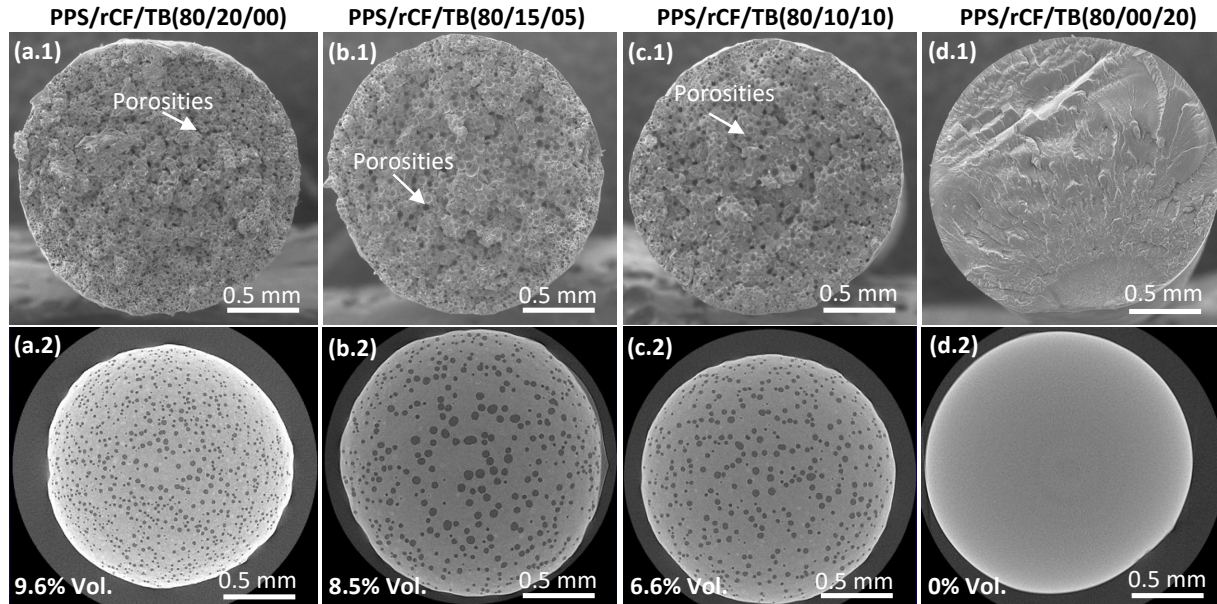


Figure 6.6 SEM (a.1-d.1) and micro-CT (a.2-d.2) images of the fracture surface of PPS composite filaments used to determine the porosity level with a CI of 95 %. (a.1-a.2) PPS/rCF/TB (80/20/00), (b.1-b.2) PPS/rCF/TB (80/15/05), (c.1-c.2) PPS/rCF/TB (80/10/10), (d.1-d.2) PPS/rCF/TB (80/00/20).

#### 6.4.2.2 SEM and Micro-CT analysis of IM and FFF printed PPS and its composites

**Figure 6.7** shows SEM images along with micro-CT images of the FFF printed PPS composites. The SEM images were observed on fracture surfaces resulted from Izod impact testing of specimens, while untested dogbone specimens were used for micro-CT scans, respectively. The SEM and micro-CT images of IM specimens were not presented here, since no detectable porosity was evaluated in their volume. The observed porosity encompasses both inter-layer and intra-layer ones and were indicated by white arrows on SEM micrographs (left column) and black arrows on the micro-CT images (right column). A common characteristic of SEM images is that the reinforcements and the fillers present a good dispersion and distribution in the PPS matrix for all the formulations.

**Figure 6.7(a)** shows the SEM and micro-CT images of the rCF/TB (20/00) composites that helped to quantify the level of porosity inside FFF printed dogbone specimens. A brittle fractured surface, partial wetting of the rCF surface by PPS matrix, some rCF fiber pull-outs, and presence of porosity can be observed in the SEM image. Intra-layer porosity, which is formed due to the addition of



rCF, can be observed through the matrix. The average total porosity content was computed to be 9.2 (2.7) %. The porosity content is mostly dominated by intra-layer types of porosity with dimensions that varied in 10-30  $\mu\text{m}$  range.

**Figures 6.7(b) and 6.7(c)** present SEM and micro-CT images of the rCF/TB (15/05) and rCF/TB (10/10) composites, respectively. The porosity content decreased when replacing the rCF by TB. The average total porosity content for rCF/TB (15/05) and rCF/TB (10/10) composites was found to be 8.1 (2.0) % and 6.9 (2.9) %, respectively. The size of intra-layer porosities is also similar to the former case, which deviates between 10-30  $\mu\text{m}$ . Moreover, the incorporation of TB particles seems to help in fiber-matrix adhesion since the surface of rCF is covered by a mixture of TB and matrix. The enhanced fiber-matrix adhesion phenomenon could be explained by the similar carbon-based surface characteristics of TB and rCF, which possibly favor their chemical affinity to each other, when compared to their chemical affinity for the neat PPS matrix. This clear findings from SEM analysis of rCF/TB (15/05) and rCF/TB (10/10) formulations would confirm the observations resulted from DSC analysis (**Figure 6.4(a)**), e.g., that the common C-structures of rCF and TB brought them together and possibly reduced the number of nucleation sites.

**Figures 6.7(d)** presents the rCF/TB (00/20) composites presenting the lowest computed porosity content of 2.2 (0.9) %. This porosity content consists of only inter-layer porosity, while there was no detectable intra-layer porosity. This observation can also be supported and explained by the previous images presented in **Figure 6.6(d.1)** and **Figure 6.6(d.2)** where, again, no significant porosity was observed inside the rCF/TB (00/20) composite filaments, the precursor of the 3D printed the specimen analysed here.

It can be concluded that the source of intra-layer porosity comes from rCF incorporation, while the inter-layer porosity may result from the deposition of successive layers of melted material that is specific to FFF technology and to its rapid temperature variations. As mentioned before, the cooling of PPS composite melt going out from the nozzle (set at 350  $^{\circ}\text{C}$ ) can be as rapid as 500  $^{\circ}\text{C}/\text{s}$ . The layers of PPS composites already deposited might have temperatures in between 160  $^{\circ}\text{C}$  (for the heated plateau) and 100  $^{\circ}\text{C}$  (for the heated chamber). This is an indication that the PPS composite materials passed through their optimal temperature for crystallization while cooling down, e.g., while being between the nozzle and the existing deposited layers. This should prove that PPS composites crystallized partially or fully before their deposition, which would freeze their shape,

would impeach a complete melt relaxation, and, in consequence, the fulfillment of spaces between deposited layers.

Moreover, as reported previously in **Figure 6.4(a)**, the  $T_c$  of PPS composites during cooling are 233.9, 240.3, 241.5, and 225.1 °C, for composites containing rCF/TB (20/00), rCF/TB (15/05), rCF/TB (10/10), and rCF/TB (00/20), respectively. Therefore, both the melt in deposition and the deposited layers need to be at least 225 - 242 °C or higher to avoid material crystallization before its deposition, to permit an adequate relaxation of the melt and, finally, to avoid the formation of inter-layer porosity. When these temperatures will be encountered, the composites crystallization will take place after the melt deposition while reinforcing the layers adhesion, the inter-layer porosity will be completely reduced while bringing an enhancement of final performance of FFF printed PPS composites.

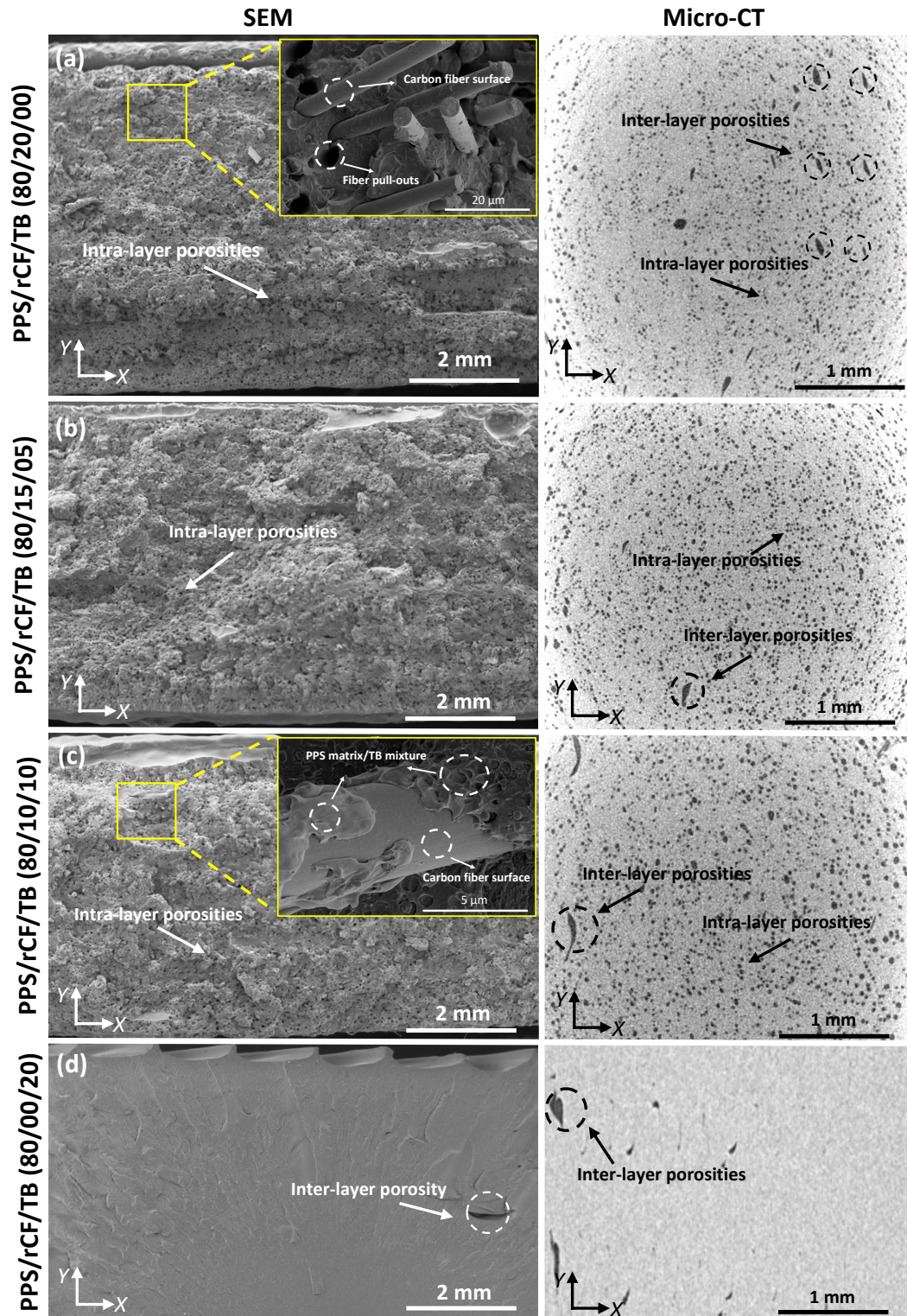


Figure 6.7 SEM images of the fracture surfaces (left column) and micro-CT images of FFF printed specimens (right column): (a) PPS/rCF/TB (80/20/00), (b) PPS/rCF/TB (80/15/05), (c) PPS/rCF/TB (80/10/10), and (d) PPS/rCF/TB (80/00/20).

### 6.4.2.3 Fiber length distribution and orientation of IM and FFF printed PPS composites

**Table 6.4** presents the numerical results for the fiber length distribution, aspect ratio and deviation angle obtained from the micro-CT images for IM and FFF printed specimens. The rCF/TB (20/00), rCF/TB (15/05), and rCF/TB (10/10) IM composite specimens have average fiber lengths of  $\sim 42.5$  (0.34)  $\mu\text{m}$ ,  $56.1$  (0.77)  $\mu\text{m}$ , and  $56.8$  (0.99)  $\mu\text{m}$ , respectively. FFF printed rCF/TB (20/00), rCF/TB (15/05), and rCF/TB (10/10) composites have average fiber lengths of  $\sim 34.3$  (0.39)  $\mu\text{m}$ ,  $34.1$  (0.43)  $\mu\text{m}$ , and  $34.6$  (0.49)  $\mu\text{m}$ , respectively. The IM composites have slightly longer average fiber lengths, with an average aspect ratio up to 11.3, when compared to those from FFF printed parts, which have an average aspect ratio up to 6.9. It should be noted that the presence of TB particles did not affect the rCF length when compare the formulations resulted from the same melt-process, e.g., for the same thermal history. The initial length of rCF of  $\sim 6$  mm was significantly reduced, as expected, due to the important shearing stresses during the composites compounding, the molding, the filament extrusion, and the FFF printing processes. This length reduction of rCF was slightly higher in the FFF printed specimens, most likely because the composites passed through more melt processes when compared to IM specimens, e.g., the filaments extrusion and extrusion through the small nozzle of the printer. Due to thermal history and rCF length differences, but also to the presence of porosities in FFF printed specimens (**Figure 6.7**), it can be expected that the mechanical performance of FFF printed specimens to be lower than of IM specimens.

Table 6.4 Micro-CT analysis results, along with the 95 % CI, on average rCF length, the corresponding aspect ratios, and rCF deviation angles of IM and FFF printed PPS composites.

Composite formulation	Average rCF length ( $\mu\text{m}$ )	Aspect ratio ( $\mu\text{m}/\mu\text{m}$ )	Deviation angle ( $^\circ$ )
IM specimens			
PPS/rCF/TB (80/20/00)	42.5 (0.34)	8.5 (0.05)	19.1 (0.21)
PPS /rCF/TB (80/15/05)	56.1 (0.77)	11.2 (0.15)	35.1 (0.37)
PPS /rCF/TB (80/10/10)	56.8 (0.99)	11.3 (0.20)	32.1 (0.42)
PPS /rCF/TB (80/00/20)	-	-	-
FFF printed specimens			
PPS /rCF/TB (80/20/00)	34.3 (0.39)	6.8 (0.07)	42.7 (0.24)
PPS /rCF/TB (80/15/05)	34.1 (0.43)	6.8 (0.09)	41.8 (0.30)
PPS /rCF/TB (80/10/10)	34.6 (0.49)	6.9 (0.10)	40.8 (0.34)
PPS /rCF/TB (80/00/20)	-	-	-

**Figure 6.8** compares the deviation angle distributions (**Figure 6.8(a) and (b)**) and the cumulative distribution functions (**Figure 6.8(c) and (d)**) of rCF for each PPS composite formulation. The deviation angle indicates the angle of the deviation of fibers from the Z-axis which is the injection and extrusion through the FFF nozzle directions, respectively. The solid bars and lines represent the deviation angles and the distribution functions of rCF in the IM specimens (**Figure 6.8(a) and (c)**) while patterned bars and dashed lines represent those of the FFF printed specimens (**Figure 6.8(b) and (d)**). The IM parts exhibit a core-shell structure for the fiber orientation along the thickness direction. The fiber alignment is more prominent in the shell region adjacent to the skin, due to high extensional flow, when compared to the core region adjacent to the mid-plane [133, 134]. Therefore, the presented results represent the fiber distribution from an area between the core and shell regions for IM specimens. In **Figure 6.8(a)**, the average deviation angles are 19.1, 35.1, and 32.1° for the IM rCF/TB (20/00), rCF/TB (15/05), and rCF/TB (10/10) composites, respectively. In **Figure 6.8(c)**, the fibers seem to be more aligned and uniform in the Z direction for the rCF/TB (20/00) composites with cumulative probability of 0.9 at approximately 45°, indicating that 90 % of the fibers have deviation angles less than or equal to 45°. The rCF/TB (15/05) and rCF/TB (10/10) composites have cumulative probability of 0.7 and 0.75 at approximately 45°, respectively. It seems that a uniformly random orientation distribution is observed with incorporation of TB particles for IM specimens, probably due to restricted mobility of rCF which prevents them from being aligned in the flow direction due to the increasing of the number of TB nanoparticles.

Additionally in **Figures 6.8(b) and 6.8(d)**, the deviation angle distribution of FFF printed specimens seems to be more uniform, pointing to a random orientation distribution as expected considering the raster angle of + 45° / - 45°. The average deviation angles are 42.7, 41.8, and 40.8 for the FFF printed rCF/TB (20/00), rCF/TB (15/05), and rCF/TB (10/10) PPS composites, respectively. All FFF printed specimens have a cumulative probability of 0.6 at 45°. The cumulative probability slope is steeper at 30° up to 50°, indicating fibers are more likely to be aligned closer to a particular direction. The slope is decreasing at 50°, indicating fewer fibers aligned beyond 50°.

The mechanical performance of FFF printed short fiber-reinforced composites is significantly influenced by the length and orientation of the fibers within the polymer matrix. Therefore, the IM PPS composites are expected to have higher mechanical performance owing to their longer fiber length distribution and alignment, when compared to those of FFF printed.

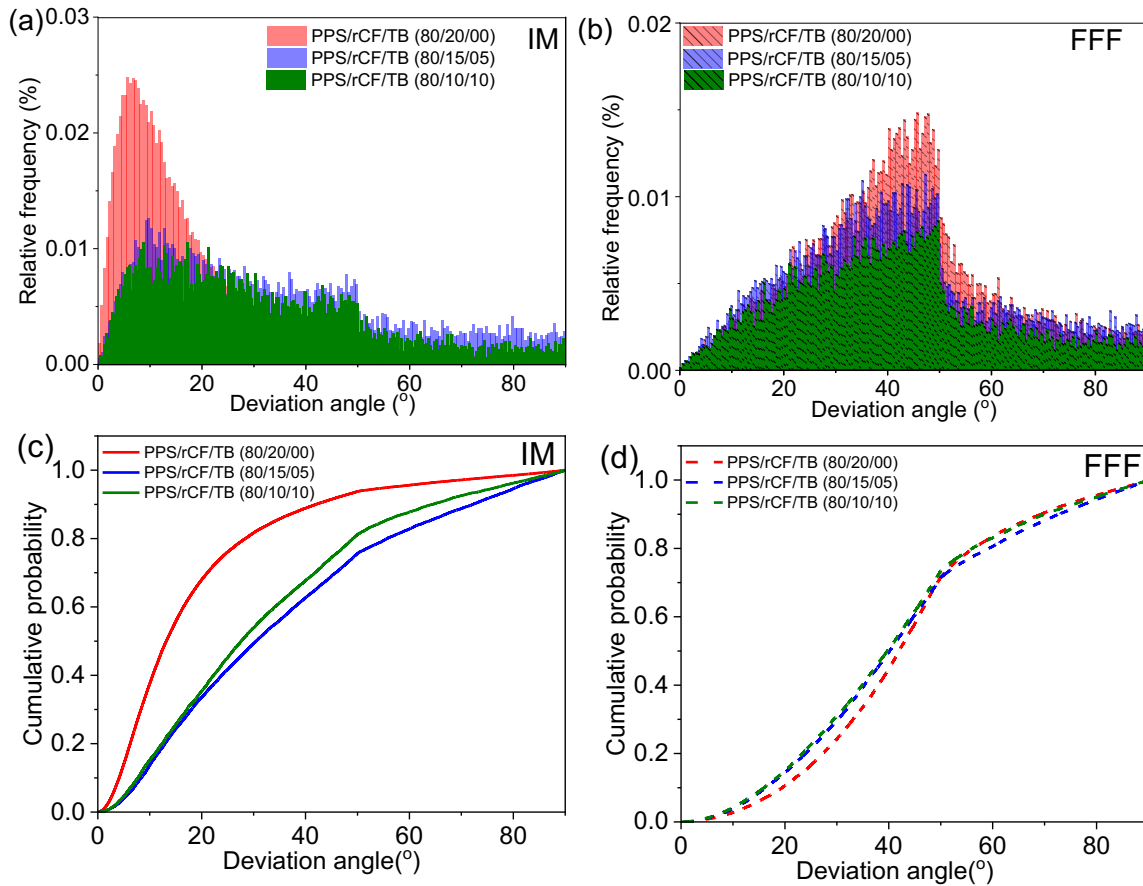


Figure 6.8 Plots of rCF of; (a) and (b) represent deviation angles that ranges from  $0^{\circ}$  to  $90^{\circ}$  with respect to their relative frequency for IM and FFF printed specimens, respectively; (c) and (d) the cumulative probability as a measure of fibers that have an angle less than or equal to a given values of  $0^{\circ}$  to  $90^{\circ}$ .

### 6.4.3 Mechanical properties of IM and FFF printed PPS composites

**Table 6.5** presents the quantitative values resulted from tensile, flexural, and unnotched Izod impact test for IM and FFF printed specimens. The TS and TM of the IM specimens of the neat PPS were evaluated at 73.0 MPa and 3.5 GPa, respectively. The rCF/TB (20/00), rCF/TB (15/05), rCF/TB (10/10), and rCF/TB (00/20) IM composites showed a TS of 151.0 MPa, 130.0 MPa, 105.0 MPa, and 62.0 MPa and a TM of 20.0 GPa, 17.3 GPa, 13.4 GPa, and 5.0 GPa, respectively. On the other hand, FFF printed rCF/TB (20/00), rCF/TB (15/05), rCF/TB (10/10), and rCF/TB (00/20) composites presented a TS of 68.5 MPa, 66.5 MPa, 65.2 MPa, and 45.0 MPa, and a TM of 6.0

GPa, 5.7 GPa, 5.4 GPa, and 5.3 GPa, respectively. FFF printed composites have, as expected, lower TM and TS, when compared to those of the IM composites.

The incorporation of 20 wt. % of rCF increased the FS and FM, while the IS was reduced. The flexural and impact properties followed the same trend with the replacement of rCF by TB. Moreover, FFF printed composites presented lower flexural and impact properties than IM specimens, which were slightly reduced with TB incorporation.

The TS, TM, FS, and FM of IM composites increased up to 2-fold and 7-fold with the incorporation of rCF and TB particles. The FFF printed composites have comparable TS (up to 68.5 MPa), and higher TM (up to 70 %) to that of neat IM PPS. However, there is a clear difference between the mechanical performance of IM and FFF printed composite counterparts, for example the rCF/TB (20/00) IM composites have 2- and 3-fold higher TS and TM respectively, when compared to FFF printed specimens. This expected difference between the mechanical performance of IM and FFF printed specimens may be attributed to the combined effects of the PPS crystallization (**Table 6.3**), porosity (**Figure 6.7**), and fiber length distribution and orientation (**Figure 6.8**, and **Table 6.4**) as discussed previously.

Table 6.5 Mechanical performance of injection molded and FFF printed PPS composites. The results are presented as mean values and a CI of 95 %.

Properties	PPS	PPS/rCF/TB (80/20/00)	PPS/rCF/TB (80/15/05)	PPS/rCF/TB (80/10/10)	PPS/rCF/TB (80/20/00)
IM specimens					
TS (MPa)	73 (4)	151 (14)	130 (4)	105 (3)	62 (8)
TM (GPa)	3.48 (0.07)	19.99 (1.06)	17.25 (1.14)	13.44 (1.18)	4.99 (0.14)
FS (MPa)	110 (4)	204 (2)	182 (2)	144 (1)	55 (0,5)
FM (GPa)	3.65 (0.03)	17.51 (0.14)	14.19 (0.02)	10.78 (0.05)	3.20 (0.03)
IS (kJ/m <sup>2</sup> )	40.3 (2)	34.7 (1.2)	29 (0.8)	24.8 (0.6)	17.8 (0.6)
FFF printed specimens					
TS (MPa)	-	68,5 (2,5)	66,2 (3)	65,5 (1,5)	45 (4)
TM (GPa)	-	5.96 (0.25)	5.73 (0.09)	5.39 (0.07)	5.26 (0.12)
FS (MPa)	-	114 (1.4)	105 (1.5)	102 (1.3)	79 (4)
FM (GPa)	-	5.43 (0.09)	5.10 (0.05)	5.08 (0.12)	4.76 (0.05)
IS (kJ/m <sup>2</sup> )	-	19.7 (2.7)	17.5 (1.1)	15.3 (1.9)	8 (1.8)
FFF printed specimens annealed at 235 °C					
TS (MPa)	-	81 (2)	-	-	-
TM (GPa)	-	6.53 (0.13)	-	-	-



## 6.5 FFF applied to high performance composites: current challenges vs. required improvements

This study demonstrated that when trying to adapt the PPS/rCF/TB composites to the existing FFF technology, the encountered challenges need to be solved such as reduce porosity formation, increase the crystal formation, improve the layer-to-layer adhesion. The industry objective would be that the parts fabricated using FFF technology to be as similar as possible in performance to those fabricated using IM technology.

As explained in Section 6.4.1.3, the IM and FFF printed specimens underwent very different thermal histories, resulting in IM specimens having higher crystallinity contents than FFF printed specimens. The crystallinity content and crystallization kinetic directly affected the mechanical performance of FFF printed semi-crystalline composite parts, as they might lead to weak layer adhesion due to the formation of crystals before layers deposition, preventing from a complete welding between successive layers [31]. Moreover, crystallization kinetic results suggest that the FFF printing temperature fluctuations might not be appropriate to induce a complete crystallization during FFF printing. For example, after annealing, the crystallinity content of PPS/rCF/TB (20/00) composites increased up to 58 % (**Table 6.3**), similar to 55 – 59 % crystallinity calculated from DSC 60-minutes isothermal testing at 250 °C that mimicked an ideal FFF cycle (**Table 6.2**). The annealed composite exhibited 18 % and 10 % higher TS and TM, respectively, when compared unannealed specimens (**Table 6.5**). The results showed that differences in crystallization levels observed between IM and FFF specimens were reflected on mechanical properties of the final parts. Moreover, to be able to modify the crystallization kinetic of a PPS composite during its FFF printing, it was demonstrated that the environmental temperature needs to be higher than the one that FFF technology offers currently. For PPS/rCF/TB composites, an ideal environmental temperature during FFF printing would be between 240 – 250 °C.

Porosity could act as defects and stress concentration points, which make 3D printed composites more susceptible to crack propagation, so weaker in terms of their mechanical performance. It was observed that as the porosity content of FFF printed specimens reduces, the difference in mechanical performance between IM and FFF printed PPS specimens reduces accordingly. The inter-layer porosity in PPS composites is attributed to the rapid cooling of the melt during deposition. The cooling occurs below the  $T_g$  or  $T_c$ , which solidifies the melt prematurely, preventing



melt relaxation and hindering the bonding between the deposited layers. Crystallization study results suggest that FFF printing of PPS composites in higher environmental temperature (240 - 250 °C) could contribute to reduce inter-layer porosities owing to enhanced molecular mobility and relaxation of deposited layer.

The characterization results for PPS composites indicated that improvements in the temperature dynamics of the FFF 3D printing process are necessary to compete with the performance of conventionally manufactured parts. The printing chamber temperature must be adjusted based on the  $T_g$ ,  $T_c$ , and  $T_m$  to ensure strong adhesion between consecutive deposited layers. However, current FFF technology is limited because the chamber temperature of printers typically falls below the critical  $T_g$  or  $T_c$  values required for high-performance thermoplastic composites, such as PEI, PPS, PEEK etc. In this context, the challenge of optimizing printing temperatures is increasingly being addressed by both the scientific community and 3D printer manufacturers.

## 6.6 Conclusion

In this study, formulations of composites based on the semi-crystalline PPS with rCF and TB were successfully developed and used in compounding, injection molding, filaments extrusion, and in FFF printing. IM and FFF printed composites were characterized and compared in terms of microstructural, crystallization, and mechanical properties.

The crystallinity content of PPS composites was evaluated to decrease from 71.7 % down to 56.9 % in compounded composite pellets, and from 93.5 % down to 37 % in IM specimens, when compared to neat PPS. Furthermore, it was found that addition of rCF and TB increased the crystallization half time. The increased crystallization half time can be attributed to the interactions between the growing crystals and the fillers, demonstrating the effect of rCF and TB incorporation on the composite's crystallinity development. Similarly, increasing isothermal crystallization temperatures favored the crystallinity content and increased the crystallization half time.

The microstructural properties of PPS composites were examined for both IM and FFF printed components. The porosity content of FFF printed PPS specimens with rCF/TB (00/20) is ~ 2.2 %, while IM specimens shows ~ 1 % of porosity. The porosity content goes up to 9.2 % for PPS containing rCF/TB (20/00), due to rCF incorporation. The average fiber length of IM composites is longer than that observed in FFF printed specimens and more aligned in the Z direction. The IM

rCF/TB (20/00), rCF/TB (15/05), and rCF/TB (10/10) composites have 25 %, 65 %, and 65 % longer average fiber lengths, when compared to their FFF printed counterparts. Moreover, fibers are more aligned in the Z direction for IM composites, since FFF printed specimens have a raster angle of  $+45^{\circ}$  /  $-45^{\circ}$ .

Incorporating 20 wt. % of rCF led to a significant enhancement in the tensile strength and modulus of IM PPS specimens, increasing from 82 MPa to 151 MPa and 3.48 GPa up to  $\sim 20$  GPa, respectively. FFF printed specimens showed approximately 60 % higher tensile modulus when compared to IM neat PPS. Such level of enhancement in the mechanical properties of IM specimens is a clear indication of efficient load transfer that resulted from longer fiber length and alignment with the combination of a higher crystallinity content and the absence of porosity, when compared to FFF printed specimens.

Moreover, developing different formulations of PPS composites by the utilization of rCF combined with TB particles provided environmentally friendly aspect to the developed composites, when compared to utilizing virgin CF and furnace carbon black particles, along with a cost reduction. The mechanical performance of the FFF printed composites was compared with IM specimens, and the effect of the printing process on the microstructure and its impact on mechanical performance was extensively characterized and explained. The developed composite formulations were found to be promising candidates for various FFF applications in interior aerospace and ground transportation, such as sandwich panels, air ducts, and ventilation systems.

## CHAPTER 7      ARTICLE 3: FLEXURAL MECHANICAL PROPERTIES OF SANDWICH PANELS FABRICATED BY FILAMENT-EXTRUSION OF HIGH- TEMPERATURE THERMOPLASTIC COMPOSITES

Dogan Arslan<sup>a,b</sup>, Mihaela Mihai<sup>b</sup>, Daniel Therriault<sup>a</sup>, Martin Lévesque<sup>a</sup>

a: Department of Mechanical Engineering, Polytechnique Montreal, Montreal, QC., H3T 1J4, Canada

b: Advanced Manufacturing, Automotive, and Surface Transportation Research Center, National Research Council Canada, 75 de Mortagne, Boucherville, QC., J4B 6Y4, Canada

Submitted to Additive Manufacturing on October 07, 2024.

### 7.1 Abstract

This study investigated the flexural properties of sandwich panel structures fabricated by the filament-extrusion 3D printing technology using novel high-temperature thermoplastic polymer composites of polyetherimide (PEI) and polyphenylene sulfide (PPS). Various formulations of PEI and PPS composites, combined with recycled carbon fiber (rCF) and thermal black (TB) particles, were manufactured. The flexural properties were assessed through a three-point bending test, comparing the performance of sandwich panels printed with these filaments and those printed with commercially available filaments. Dimensional accuracy was evaluated using a 3D scanner, revealing that 90 % of scanned points deviated a maximum of 0.2 mm from the CAD model. X-ray micro-tomography measured porosity, finding up to ~ 12 % in PEI and ~ 8 % in PPS skins. The microstructural analysis of the composites revealed a level of adhesion deemed acceptable between successive layers of printed parts and adequate dimensional accuracy. A digital image correlation (DIC) system assessed full-field strain and crack propagation during flexural testing, showing crack initiation due to strain concentration in the core region, consistent across all specimens. The sandwich panels printed with developed filaments exhibited comparable flexural properties to that of panels printed with commercial filaments, with a bending load capacity of up to 3.0 kN for approximately 50 g specimens. The printing quality and mechanical performance of the novel PEI and PPS composite formulations demonstrated in this study suggested that they could serve as viable alternatives to commercial filaments.

## 7.2 Introduction

Sandwich panels consist of two outer layers (skin) with lightweight core structures in which the core increases the bending stiffness of the structure by enhancing the moment of inertia. Conventional production of sandwich structures includes the separate manufacturing of the skin (e.g., laminates, prepreg) and the core, and the subsequent joining of the skin to the core with adhesive or fusion bonding methods [2, 3]. Moreover, the machining of the core can lead to significant material waste [135, 136]. The most used core types are corrugated, honeycomb, balsa wood, and cellular foams. Honeycomb cores, primarily used in aerospace applications, are made of aramid fiber impregnated with phenolic resin, known commercially as Nomex. Nomex is widely used because its mechanical properties are comparable to those of aluminum honeycombs. Nomex cores with a density of  $129 \text{ kg/m}^3$  have a shear modulus of 112 MPa and a core shear strength of 3.2 MPa in the longitudinal direction [83].

Fused Filament Fabrication (FFF) is an open-source three-dimensional (3D) printing technology for processing thermoplastic feedstocks and their composites to manufacture 3D structures [9, 10]. FFF additive manufacturing would enable fabricating sandwich panel structures in a single step with a higher flexibility in the design, when compared to conventional manufacturing methods. However, there are some limitations to the adoption of the FFF technology in industrial manufacturing. These include the difference in mechanical properties between a FFF printed component and a conventionally manufactured component (e.g., injection molded), as well as the limited material choices available for FFF printing, when compared to other processes.

Studies dealing with 3D printed sandwich panel structures in the literature are mostly focused on mechanical and acoustic performance based on different core structure designs with commercially available filaments. Commodity polymer feedstocks like polylactic acid (PLA) [92, 93, 137] and acrylonitrile butadiene styrene (ABS) [87-89] have been used to print sandwich panel structures, when process tuning and mechanical properties were studied. For example, Castro et al. [92] investigated the mechanical properties of printed PLA sandwich panels with different hexagonal honeycomb core designs, including core printed out-of-plane and in-plane direction. It was reported that the out-of-plane honeycomb sandwich panels exhibited 29 % and 55 % higher flexural modulus and strength, respectively, when compared to those made of in-plane honeycomb cores. Pierre et al. [138] compared the acoustic capabilities and mechanical properties of sandwich panels

with hexagonal honeycomb cores and Trapezoidal Compact cores that were printed with PLA. The authors reported that the sandwich panels with a Trapezoidal Compact core exhibited 90 % absorption within the acoustic range of 643 Hz and 1160 Hz and 10 % higher flexural stiffness, when compared to sandwich panels with a hexagonal core.

High-temperature and high-performance thermoplastic polymers have superior thermal and mechanical properties, when compared to commodity polymers [51, 54]. Polyetherimide (PEI) has a tensile strength of up to 110 MPa, and a tensile modulus of 3.2 GPa with inherent flame retardancy, chemical and UV resistance, and service temperature of up to 175 °C for selected grades [4]. Polyphenylene sulfide (PPS) is a semi-crystalline thermoplastic polymer that has a tensile strength of up to 90 MPa, and a tensile modulus of 3.5 GPa. PPS is inherently flame-retardant owing to its chemical configuration and its innate capacity to undergo charring upon exposure to an open flame [5]. Commercially available FFF filaments of PEI and PPS composites are limited to a few manufacturers and are up to 10-fold more expensive, when compared to their conventional pellet form.

There are limited studies on the FFF of printed sandwich panels with high-temperature composite filaments. For example, Pierre et al. [96] compared the flexural properties of sandwich panels with different core designs and materials using commercial neat polyether ether ketone (PEEK) and PEEK reinforced with 30 wt.% carbon fibers (CF). The study features sandwich panels with honeycomb cores printed entirely from PEEK/CF, as well as panels with hexagonal honeycomb and Trapezoidal Compact cores printed from neat PEEK, with skins printed from PEEK/CF. The authors demonstrated that the sandwich panels of hexagonal honeycomb and Trapezoidal Compact cores with their skins printed from PEEK/CF and cores printed from neat PEEK exhibited an 18 % and 66 % higher flexural stiffness, respectively, when compared to the honeycomb sandwich panels printed entirely from PEEK/CF. The studies dealing with PEI based commercial filament of ULTEM 9085 analyzed the effect of building direction, structure width, wall, and top layer thickness on the mechanical performance of sandwich panels [94, 95]. For example, Bagsik et al. [95] studied the effect of build direction (side, flat, and upright) on the mechanical properties of sandwich panels printed with commercial ULTEM 9085 filaments. The results showed that specimens printed in the side and flat positions exhibited higher flexural stresses, ranging from 60 to 75 MPa, when compared to those printed in the upright position (25–35 MPa).

In the literature, the printing quality, including dimensional stability, layer adhesion, porosity, as well as damage and failure behaviors of honeycomb sandwich panels, is mostly studied by observing the failed or broken specimens after testing. However, significant information about the fracture mechanism of sandwich panels can be obtained by characterizing the microstructure and observing the failure process during testing. X-ray micro-tomography allows to observe porosity, layer adhesion between successive layers, and the core of the sandwich panel. The digital image correlation (DIC) system, equipped with high-speed cameras, enables *in situ* observation of various failure and damage mechanisms, such as skin-core debonding and local buckling. In a few studies, the 3D DIC technology provided an observation of the deformation process, damage modes, and strain fields of sandwich structures [100, 139-142]. However, to the best of our knowledge, no study focused on sandwich panels 3D printed using high-temperature resistant composites.

In this study, we developed composite filaments of ULTEM 1040A grade of PEI and PPS by the incorporation of recycled carbon fiber (rCF) and thermal black (TB) particles. Using rCF and TB is a sustainable approach that contributes to eco-responsibility by significantly reducing the environmental impact and manufacturing costs, a key advantage over commercial filaments. We investigated the FFF printing of honeycomb sandwich panels using these composite filaments and evaluated their flexural properties. We also compared the performance of these composite filaments with commercially available filaments as a benchmark. The FFF printed sandwich panels were characterized in terms of dimensional stability, porosity analysis, and fracture detection. The originality of this study lies in its focus on FFF printing sandwich panels using developed high-temperature composites and on the detailed failure analysis presented herein.

## **7.3 Materials and Methods**

### **7.3.1 Materials**

PEI composite filaments were manufactured by using ULTEM 1040A pellets, a low-viscosity PEI grade that was purchased from SABIC Americas (USA). PPS composite filaments were manufactured using Fortron 0214P1 grade pellets that were purchased from Celanese (Celanese Corporation, Fortron Industries LLC., Wilmington, NC., USA).

The developed composites were reinforced with recycled carbon fibers (rCF) and thermal black (TB) particles. re-Evo<sup>®</sup> HSC (Phenix 0.25), the short rCFs used in this study, were purchased from

Carbon Conversion (Lake City, SC, USA). TB Thermax<sup>®</sup> N990 (TB N990) particles were supplied by Cancarb Limited (Medicine Hat, AB, Canada).

Commercial filaments of PEI and PPS composites were used as benchmarks in this work. A 1.75 mm diameter commercial spooled filament of PEI (ULTEM 9085 grade) reinforced with 15 wt.% short CF (CARBONX<sup>™</sup> PEI+CF15, 3DXTECH<sup>®</sup>, USA) and PPS reinforced with 15 wt.% short CF (Essantium PPS-CF, VisionMiner, USA) were purchased. The commercial PEI and PPS composites containing 15 wt.% CF called as PEI-commercial, and PPS-commercial, respectively, in this study.

## 7.3.2 Manufacturing of composite filaments

### 7.3.2.1 Compounding

The neat PEI and PPS were dried before each processing step (i.e., compounding, filaments extrusion, and FFF) at 140 °C and 100 °C for 12 hours, respectively. PEI and PPS pellets were compounded with rCF and TB by using a Bühler clamshell co-rotating twin-screw extruder (Bühler Group, Gupfenstrasse 5, Uzwil 9240, Switzerland). The temperature profiles of the extruder were set to incrementally rise from 280 °C to 350 °C, and 280 °C to 330 °C from the feeding zone to the die, respectively. Polymer pellets, TB, and rCF, were fed through separate feeders in the first zone of the extrusion line. The extruded composites were cooled down in the air and pelletized. The pellets were further used in filament extrusion by using a filament-making extruder (Xcalibur, Noztek, Shoreham, England). The filaments were continuously monitored for a constant diameter of  $1.75 \pm 0.05$  mm and a steady ovality by using a laser controlling system with 1200 scan/s along radial axes (Zumbach-ODAC18XY, Switzerland). **Table 7.1** lists the extruded composites formulations containing combinations of rCF and TB developed for this work and the commercial filaments.

Table 7.1 Formulations of PEI and PPS based filaments from this work and of the commercial filaments. The CF content for commercial filaments is reported based on the manufacturer's technical datasheet.

Formulation	Matrix (wt.%)	rCF (wt.%)	TB (wt.%)
PEI/rCF/TB (80/20/00)	80	20	0
PEI/rCF/TB (80/10/10)	80	10	10
PPS/rCF/TB (80/20/00)	80	20	0
PPS/rCF/TB (80/10/10)	80	10	10
Commercial	Matrix (wt.%)	CF (wt.%)	
PEI-commercial	85	15	-
PPS-commercial	85	15	-

### 7.3.2.2 Design and Fused Filament Fabrication of sandwich panels

**Figure 7.1(a)** presents the schematic of the hexagonal honeycomb sandwich panel annotated with some common variables, which were designed using SolidWorks (SolidWorks2022, Dassault Systèmes, France) for flexural testing purposes. The hexagonal filling pattern is symmetrical, which allows homogeneous load distribution during flexural testing. The number of core cells, core thickness, and skin thickness were determined considering the ASTM standards ASTM D7250 and ASTM C393. The sandwich panel had a dimension of 20 mm in height, 49 mm in width, and 125 mm in length. The core and skin had a height of 16 mm and 2 mm, respectively. The hexagonal core had a cell wall width of 6.5 mm and a cell wall thickness of 0.8 mm, respectively. The width of the sandwich panel was chosen to be greater than least twice the sandwich height and three times the cell size. The core cell width was chosen to fit at least three cells in the width direction based on the ASTM standards, while the skin thickness was selected to provide adequate stiffness. The cell wall thickness was selected to ensure that at least two layers could be printed in the thickness direction using a 0.4 mm nozzle. This choice was made because it was found by trial and errors that sandwich panels printed with single-layer walls exhibited poor layer adhesion and delamination during printing.

Simplify3D software (Simplify3D, Cincinnati, OH, USA) was used to slice the 3D models of the specimens on the flatwise position. An open-source printer, AON-M2 (AON3D, Montreal, QC, CA), equipped with a 0.4 mm nozzle, heated bed, and a heating chamber, was used to print sandwich panel specimens with the developed composites filaments, as depicted in (**Figure 7.1(b)**). **Table 7.2** presents the main printing parameters for sandwich panels printed with PEI and PPS composites, respectively. The sandwich panel skins were printed with a raster angle of  $+45^\circ / -45^\circ$  with respect to the  $X$  axis in the  $XY$  plane with a 100 % infill ratio. Three (3) sandwich panel specimens were printed for each formulation.



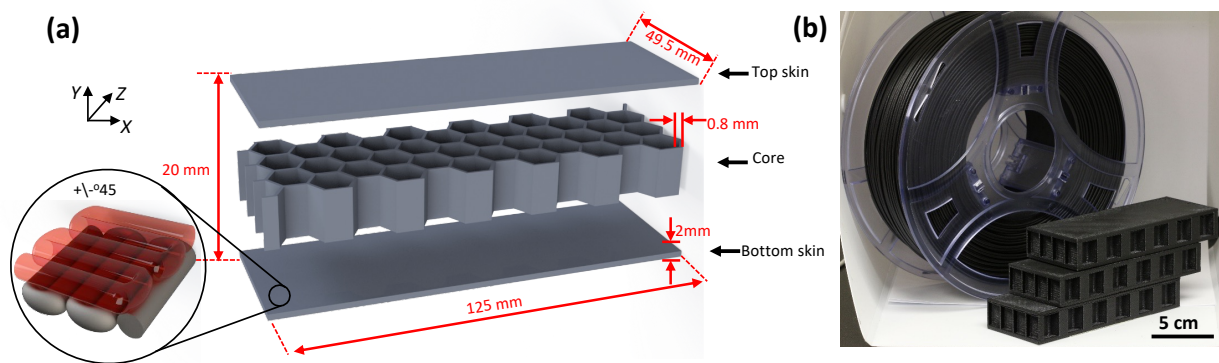


Figure 7.1 Images of CAD design of sandwich panels and FFF printed sandwich panel specimens: (a) rendered images of sandwich panel CAD file with dimensional parameters, (b) FFF printed sandwich panel specimens and composite filament spool based on PEI/rCF/TB(80/10/10).

Table 7.2 FFF printing parameters used for the sandwich panel printing of developed and commercial PEI and PPS composite filaments.

FFF parameters	PEI composites	PPS composites
Nozzle temperature (°C)	400	350
Bed temperature (°C)	180	160
Chamber temperature (°C)	135	100
Fill-in (%)	100	100
Extrusion multiplier	1	1
Extrusion width (mm)	0.48	0.48
Layer thickness (mm)	0.3	0.3
Printing speed (mm/s)	50	50
Support	None	None

### 7.3.3 Characterization methods

#### 7.3.3.1 Optical 3D Scanner

The sandwich panel surfaces were scanned using an optical 3D scanner (GOM Atos Core 200, GOM Metrology, Germany). The scanned points on the surface were reconstructed as a mesh and converted to an STL file. The scanned volumes of the sandwich panels were compared with the CAD file by using CloudCompare software (version 2.12.4), which allows for quantifying the distance between the scanned surface and the CAD file. The CAD-to-mesh data were presented as cloud-to-mesh (C2M) signed distance, which could be positive or negative with respect to the reference point.

### 7.3.3.2 X-ray microtomography

X-ray microtomography (micro-CT) was carried out to observe the porosity using a Zeiss Xradia™ 520 Versa X-ray computed tomography system (Carl Zeiss Microscopy GmbH, Jena, Germany). The applied source voltage and power were 50 kV and 4 W, respectively, with a  $0.4\times$  objective without filter, for an exposure time of 20 s.

Dragonfly software (Object Research Systems ORS Inc, Montreal, QC, Canada) was used to analyze micro-CT scan data. The quantitative data on the thickness of the top skin, bottom skin, and core walls were obtained through volume distance mapping of micro-CT images using Dragonfly software, which provided thickness distribution for individual sections.

### 7.3.3.3 Digital image correlation (DIC)

A digital image correlation (DIC) setup (Correlated Solutions, Irmo, SC, USA) was used for measuring the full-field strain distribution during mechanical testing. The DIC setup includes two high-resolution cameras (Grasshopper3 GS3-U3-50S5M) and a light system. **Figure 7.2** presents the DIC images of sandwich panel specimens with a spackle pattern. The speckle patterns were created by first spraying the specimens with matte white paint (Rust-Oleum Canada, Concord, ON, Canada), followed by applying a black speckle pattern using black paint (Rust-Oleum Canada, Concord, ON, Canada). The images were acquired at a frame rate of 300 FPS during flexural testing with the software VicSnap (Correlated Solutions, Inc., Columbia, SC, USA). The speckle images were analyzed using Vic-3D v9 software for local correlation. The analysis parameters were chosen to maximize the correlation surface for each test while enhancing spatial resolution. The subset size ranged from 50 to 90 pixels, and the step size varied from 5 to 7 pixels.

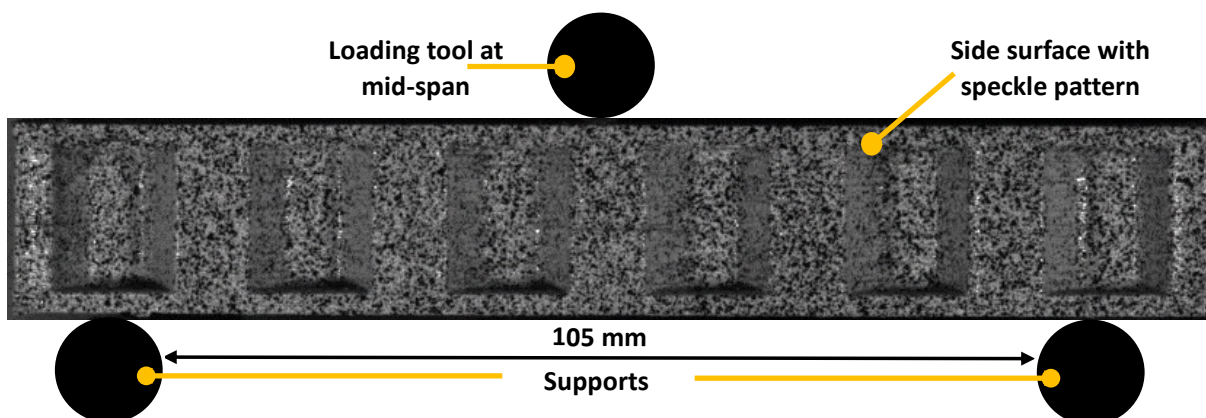


Figure 7.2 DIC image of FFF printed sandwich panel (PEI/rCF/TB (80/20/00)) with spackle pattern and three-point bending test setup with support span distance and loading tool position on the specimen equidistant from the two end supports.

### 7.3.3.4 Three-point bending testing

Three-point bending testing was carried out using an MTS Insight electromechanical testing machine (MTS Systems, Eden Prairie, MN, USA) equipped with a 50 kN load cell. Testing was performed using a support span length  $S$  of 105 mm with a crosshead speed of 2.6 mm/min. Three (3) specimens for each formulation were tested, and the mean values and their confidence intervals (CI) of 95 % were reported. Before testing, all the specimens were conditioned at 23 °C, 50 % RH for at least 40 hours.

### 7.3.3.5 Computation of flexural and shear properties

The flexural and shear properties were computed based on ASTM D7250 and ASTM C393 standards by using the dimensional parameter shown in **Figure 7.3**. The effective flexural stiffness (N/mm) was computed through a linear regression of the load/displacement curves. The sandwich panel's flexural rigidity, transverse shear rigidity, core shear modulus, and core shear stress were computed according to

$$D = \frac{E_f(d^3 - c^3)b}{12}, \quad (7.1)$$

$$U = \frac{P(S - L)}{4[\Delta - \frac{P(2S^3 - 3SL^2 + L^3)}{96D}]}, \quad (7.2)$$

$$G_c = \frac{U(d - 2t)}{(d - t)^2b}, \quad (7.3)$$

$$F = \frac{P_{max}}{(d + c)b}, \quad (7.4)$$

where  $D$  is the flexural rigidity in N-mm<sup>2</sup>,  $U$  is the transverse shear rigidity in N,  $G_c$  is the core shear modulus in MPa,  $F$  is the core shear ultimate strength in MPa,  $P$  is the total applied force in N,  $E_f$  is the elastic modulus of the skin in GPa,  $S$  is the support span length of 105 mm,  $L$  is the load span length in mm which is 0 for this configuration,  $\Delta$  is the displacement in mm,  $d$  is the sandwich thickness of 18 mm,  $c$  is the core height of 16 mm,  $b$  is the sandwich width of 49.5 mm, and  $t$  is the skin thickness of 2 mm.

The orthotropic skin and core properties were assumed to be as isotropic. **Table 7.3** presents the bulk properties of the composites that were used for printing the sandwich panels. The elastic

modulus of developed composites were determined experimentally [143, 144] , whereas, for commercial filaments, the values were obtained from the product' technical datasheets [55].

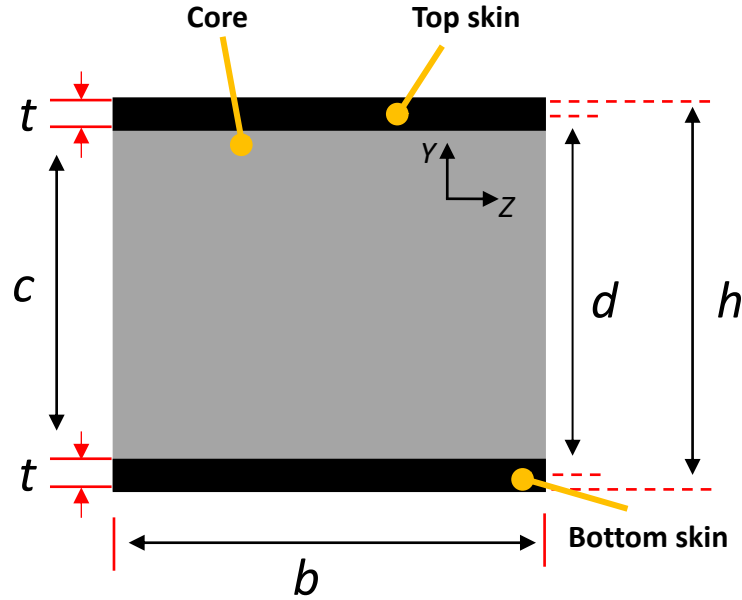


Figure 7.3 The sandwich beam cross-section with the dimensional parameter for the calculation of the flexural mechanical properties.

Table 7.3 Elastic modulus values used for the analytical calculation of sandwich panel properties for developed and commercial composite filaments.

Composite formulation	Elastic modulus (GPa)
PEI/rCF/TB (80/20/00)	4.23 (0.13)
PEI/rCF/TB (80/10/10)	4.21 (0.12)
PEI-commercial	8.60 (N/A)
PPS/rCF/TB (80/20/00)	5.96 (0.25)
PPS/rCF/TB (80/10/10)	5.39 (0.07)
PPS-commercial	4.55 (0.12)

## 7.4 Results and Discussion

### 7.4.1 Dimensional accuracy of FFF printed sandwich panels

The dimensional accuracy of the specimens with respect to the designed CAD model was assessed by 3D scanning and micro-CT analysis. **Figure 7.4** presents the 3D images of the scanned surface of sandwich panels and their corresponding cloud-to-mesh (C2M) distance distribution. **Figure 7.4(a)** depicts the surface roughness of the sandwich panels, which was visualized by rendering the surface mesh obtained from 3D scanning analysis. **Figure 7.4(b)** shows the 3D scanned surface of sandwich panels with a color map of C2M distance. The color map illustrates the surface roughness

on the bottom and top skins, indicated by red areas, which could be due to the over-extrusion or the sagging during bridging. **Figure 7.4(c)-(d)** shows the comparison of C2M distance distribution for each formulation in which the solid and dashed lines represent the PEI and PPS composites, respectively.

**Table 7.4** gives the quantitative data extracted from the distribution of the C2M distance, including the mean values of C2M distance and full width at half maximum (FWHM) of the peaks. Additionally, the table reports the average weight and density of the sandwich panels. The PEI composite formulations of rCF/TB (20/00), rCF/TB (10/10), and commercial filaments had a mean C2M distances of 0.08, 0.02, and 0.01 mm, respectively. The PEI composite formulations of rCF/TB (20/00), rCF/TB (10/10), and commercial filaments also had a FWHM values of 0.10, 0.23, and 0.26 mm, respectively. The PPS composite formulations of rCF/TB (20/00), rCF/TB (10/10), and commercial filaments had a mean C2M distances of -0.08, 0.12, and -0.01 mm, and a FWHM values of 0.22, 0.19, and 0.25 mm, respectively. Over 90 % of the scanned points fell within a C2M distance range of -0.2 and 0.2 mm for all specimens. The mean values of C2M distance and FWHM of the peaks indicated that the PEI and PPS sandwich panels printed with developed composites had adequate dimensional accuracy, and the results were similar to those obtained with commercial filaments.

The sandwich panels were expected to weigh approximately 53 g on average, estimated by the SolidWorks CAD software using a bulk material density of approximately 1400 kg/m<sup>3</sup>. However, all printed panels exhibited a lower weight, as listed in **Table 7.4**, when compared to the expected weight. Sandwich panels made of developed PEI and PPS composites also exhibited a lower weight, when compared to those printed with commercial filaments. The deviation in the weight of the sandwich panels led to specimens printed with developed composite filaments having lower densities, when compared to those printed with commercial filaments, as listed in **Table 7.4**. The observation regarding the weight and density of sandwich panels could be due to the presence of porosity, as the higher filler content of developed composite filaments is expected to cause higher porosity, when compared to commercial filaments, which have lower filler content.

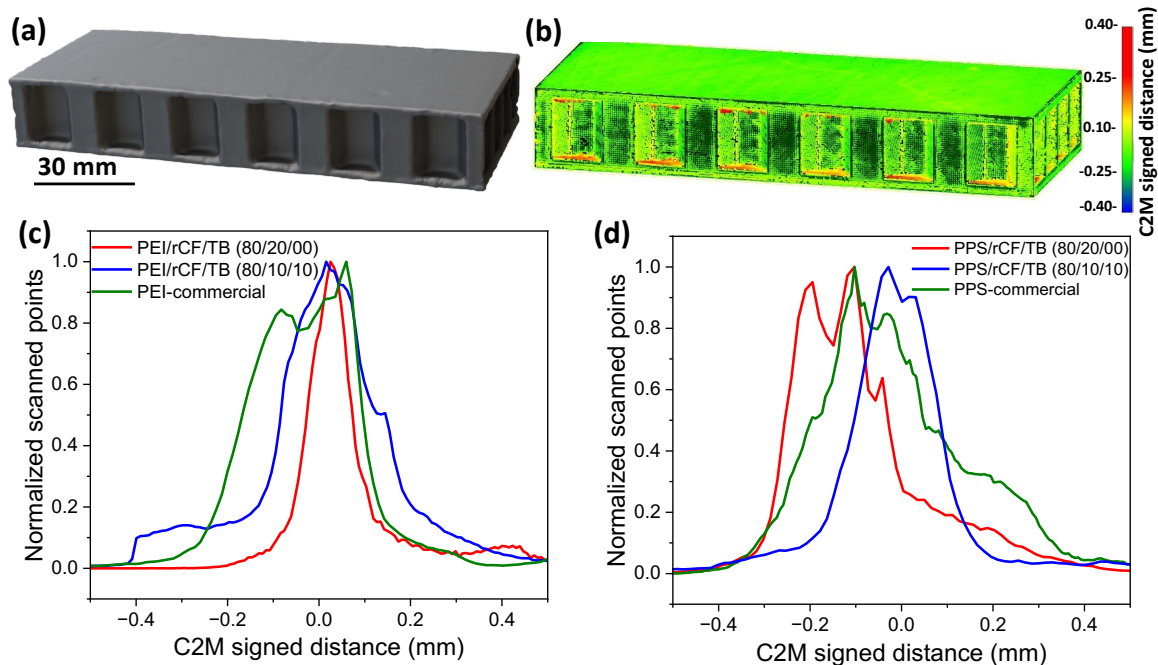


Figure 7.4 3D images of the scanned surface of a sandwich panel made of PEI/rCF/TB (80/20/00) developed composite filament for measuring the dimensions and comparison dimensional accuracy: (a) rendered 3D scanned surface of sandwich panel, (b) 3D scanned surface of sandwich panel processed with a color map of C2M signed distance with respect to their CAD model, (c) C2M distance distribution for PEI composites, (d) C2M distance distribution for PPS composites.

Table 7.4 Mean distance values of C2M signed distance extracted from a comparison of the 3D scanned volume of the sandwich panel with respect to the CAD model, FWHM of peaks, average weight, and density of sandwich panels. The average values are reported with CI of 95 % in the parentheses.

Sandwich panel formulation	Mean distance (mm)	FWHM (mm)	Average weight (g)	Panel density (kg/m <sup>3</sup> )
PEI/rCF/TB (80/20/00)	0.08 (0.02)	0.10	47.1 (0.6)	384
PEI/rCF/TB (80/10/10)	0.02 (0.16)	0.23	45.1 (0.3)	368
PEI-commercial	0.01 (0.19)	0.26	49 (0.2)	400
PPS/rCF/TB (80/20/00)	-0.08 (0.16)	0.22	47.4 (0.4)	386
PPS/rCF/TB (80/10/10)	0.12 (0.13)	0.19	47.8 (0.4)	390
PPS-commercial	-0.01 (0.17)	0.25	52.5 (0.2)	428

#### 7.4.2 Microstructure analysis of FFF printed sandwich panels

The core cell dimensions were measured using non-destructive micro-CT scans, which allowed to observe through the volume. Micro-CT scans also provided quantitative data on the porosity content within the sandwich panels. **Figure 7.5(a)** displays the reconstructed volume obtained from micro-CT images of the sandwich panel structure for PEI containing rCF/TB (20/00). **Figure**

**7.5(b)** shows a top-view cross-section of the sandwich panel, revealing the hexagonal core. **Figure 7.5(c)** illustrates a side-view cross-section, highlighting the top skin, bottom skin, and core wall cross-sections of rCF/TB (20/00) composites of PEI and PPS, respectively. The PEI composites exhibited more stable bridging than PPS composites, as highlighted in **Figure 7.5(c)**, where the PPS composites' top skin shows significant sagging. The bridging quality difference between PEI and PPS might be due to the glass transition temperature ( $T_g$ ) of PEI ( $\sim 215^\circ\text{C}$ ), which is  $80^\circ\text{C}$  higher than that of the printing chamber temperature ( $\sim 135^\circ\text{C}$ ), allowing PEI composites to solidify quickly after extrusion. In contrast, PPS composites have a much lower  $T_g$  ( $\sim 90^\circ\text{C}$ ), which is  $10^\circ\text{C}$  lower than the printing chamber temperature ( $\sim 100^\circ\text{C}$ ), causing a delay in solidification. **Figure 7.5(d)** shows 3D images of segmented porosity in the top and bottom skins, indicated in yellow. The porosities mainly consisted of inter-layer porosities, as the scan resolution did not allow for the detection of intra-layer porosities within the expected size range of  $10\text{--}30\ \mu\text{m}$ .

**Table 7.5** presents the average porosity content in the bottom and top skins, along with the average thickness values for the bottom skin, top skin, and core wall, as extracted from the micro-CT image processing. The porosity content in the bottom skin of the PEI composites of rCF/TB (20/00), rCF/TB (10/10), and commercial filaments was 9.4 %, 6.3 %, and 1.9 %, respectively. The porosity content on the top skin was evaluated to be higher, e.g., 12.7 %, 9.4 %, and 6.2 %, respectively, for the same formulations. The commercial PEI filament also exhibited lower porosity, when compared to the developed filament. The lower porosity content of sandwich panels printed with commercial filaments can be attributed to the lower  $T_g$  ( $186^\circ\text{C}$ ) of commercial PEI (ULTEM 9085 grade) matrix that promoted layer adhesion and resulted in lower porosity, when compared to developed PEI composites with  $T_g$  of  $\sim 215^\circ\text{C}$ . Additionally, the commercial filament includes a lower filler content, reported to be 15 wt. % of carbon fiber which could lead to lower porosity, when compared to developed filaments with filler content of 20 wt.%.

The porosity content in the bottom skin of the PPS composites of rCF/TB (20/00), rCF/TB (10/10), and commercial filaments was 5.0 %, 3.0 %, and 4.6 %, respectively. The porosity content on the top skin increased to 8.3 %, 8.4 %, and 8.1 %, respectively, for the same formulations. The porosity content in the bottom skin was relatively reduced with the replacement of rCF with TB particles. The sandwich panels printed with developed PPS composite filaments exhibited similar porosity content, when compared to those printed with commercial PPS filaments.

The top skin of the sandwich panels had a higher porosity than the bottom skin, which could be due to inconsistent bridging since no support structure was used during printing, and the printer used lacks the air-cooling system for suspended structures like the bridging of the top skin. Moreover, the bottom skin had more consolidation of the deposited layer due to the pressure of built volume, when compared to the top skin. No significant detectable porosity was found in the sandwich panel core for both PEI and PPS composites. The observation regarding the porosity in the core could be due to the fact that the core consisted only two-layer in the thickness direction, which reduces inter-layer porosities, unlike observed in the skins. However, intra-layer porosities were present within the printed beads, but the micro-CT resolution was insufficient to quantify them.

In the CAD model, the skin and core thickness of sandwich panels were designed as 2 mm and 0.8 mm, respectively. The sandwich panels of PEI composites made of rCF/TB (20/00) had average thickness values of 2.2 mm for the bottom skin, 2.3 mm for the top skin, and 1.2 mm for the core wall. The sandwich panels made of rCF/TB (10/10) composites had an average thickness value of 1.85 mm for the bottom skin, 1.81 mm for the top skin, and 0.97 mm for the core wall. The sandwich panels made of commercial PEI composites had average thickness values of 2.21 mm for the bottom skin, 1.85 mm for the top skin, and 1.12 mm for the core wall.

The sandwich panels printed with PPS composites also had a deviation in skin and core thickness, when compared to CAD files. It was found that the sandwich panels of PPS composites made of rCF/TB (20/00) had average thickness values of 1.97 mm for the bottom skin, 2.08 mm for the top skin, and 1.13 mm for the core wall. The sandwich panels made of rCF/TB (10/10) composites had average thickness values of 1.87 mm for the bottom skin, 1.83 mm for the top skin, and 1.02 mm for the core wall. The sandwich panels made of commercial PPS composites had average thickness values of 2.13 mm for the bottom skin, 2.12 mm for the top skin, and 1.15 mm for the core wall. The sandwich panels printed with PEI and PPS composites exhibited deviation in skin thickness, when compared to the CAD design, which was specified as 2 mm. This discrepancy could be due to the presence of porosities that caused extrusion inconsistency, while poor bridging could also lead to deviation in dimensions. Moreover, considering long printing times of up to 5 hours for each specimen, the loss of 3D printer calibration might result in a change in the nozzle and printing bed distance that affected the dimensions of the printed part. The core thickness was also greater than the CAD design, which was specified as 0.8 mm. The layer width during slicing was adjusted



to 0.48 mm, and the core wall consisted of two layers in the thickness direction. In this context, considering the effect of over-extrusion, the core wall thickness resulted in being greater than the CAD design.

The micro-CT analysis, represented by the images shown in **Figure 7.5** along with the numerical values enclosed in **Table 7.5**, offered a more detailed understanding of dimensional accuracy throughout the panel's volume, including individual skins or core thicknesses. These characterization results discussed here are crucial for better interpreting the flexural testing outcomes, as deviations in dimensions could lead to variations in mechanical properties, especially in sandwich panels. For instance, if the thicknesses of the top and bottom skins differ, it could affect the rigidity of the panel or lead to uneven deformations, as the structures would no longer be symmetrical.

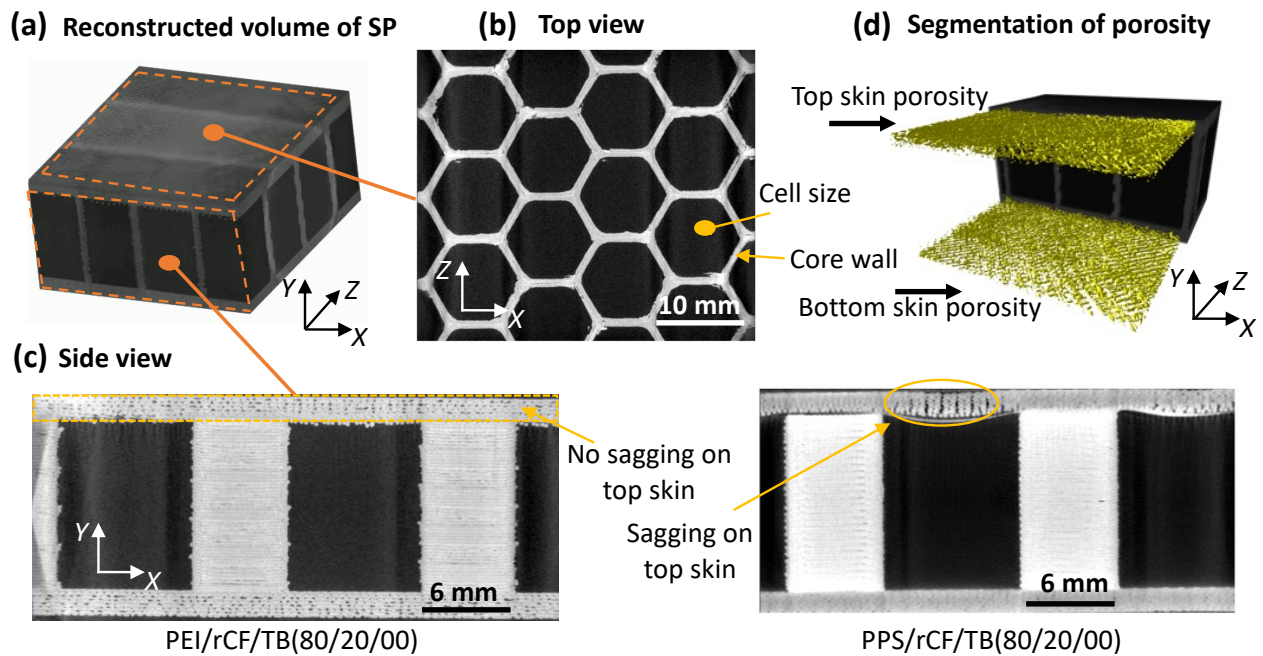


Figure 7.5 Micro-CT images of FFF printed sandwich panel structure: (a) reconstructed 3D volume of sandwich panel made of PEI/rCF/TB(80/20/00), (b) top view cross-section of sandwich panel that shows hexagonal core, (c) side views of sandwich panels showing cross-sections of top skin, bottom skins, and core walls for sandwich panels printed with PEI/rCF/TB(80/20/00), and PPS/rCF/TB(80/20/00) composite filaments, respectively, (d) rendered image of segmented inter-layer porosity in the top and bottom skin of sandwich panel, respectively.

Table 7.5 Quantitative values regarding average porosity content, including inter-layer porosity on the bottom and top skins, and the average dimensional length values, including bottom skins, top skins, and core wall thicknesses, were extracted from the processing of micro-CT images. The average values are reported with CI of 95 % in between parentheses.

Sandwich panel formulation	Porosity content (%)		Dimensions (mm)		
	Bottom skin	Top skin	Bottom skin thickness	Top skin thickness	Core wall thickness
PEI/rCF/TB(80/20/00)	9.4 (0.5)	12.7 (1.3)	2.20 (0.15)	2.30 (0.14)	1.20 (0.15)
PEI/rCF/TB(80/10/10)	6.3 (0.3)	9.4 (1.7)	1.85 (0.13)	1.81 (0.16)	0.97 (0.06)
PEI-commercial	1.9 (0.2)	6.2 (2.0)	2.21 (0.21)	1.85 (0.25)	1.12 (0.07)
PPS/rCF/TB(80/20/00)	5.0 (0.5)	8.3 (1.2)	1.97 (0.09)	2.08 (0.13)	1.13 (0.07)
PPS/rCF/TB(80/10/10)	3.0 (0.3)	8.4 (0.8)	1.87 (0.14)	1.83 (0.15)	1.02 (0.06)
PPS-commercial	4.6 (0.4)	8.1 (1.0)	2.13 (0.13)	2.12 (0.18)	1.15 (0.07)

### 7.4.3 Full-field strain measurement during flexural testing

**Figure 7.6(a)** shows the DIC images of one of the sandwich panels printed with PEI/rCF/TB(80/20/00) prior to the application of bending force and location of virtual extensometers. **Figure 7.6(b)** displays the strain values recorded in the top skin, bottom skin, and core region based on the location of virtual extensometers, respectively. The lower half of the sandwich panel, including the bottom skin, experienced tensile loading during flexural testing, resulting in positive tensile strain, while the upper half of the panel, including the top skin, experienced compressive loading, resulting in compressive strain. The strain values on the top and bottom skins were measured by applying a virtual strain gauge with the DIC setup on the skins and recording the strain changes during the testing period. Virtual strain gauges were also applied horizontally through the  $Y$  axis to measure strain deformation in the core. The strain values in the core region deviated from 0.001 to  $-0.001$  mm/mm with respect to the neural axis. The strain values approached zero near the neutral axis, as expected. The strain values recorded from virtual strain gauges located in the core region appeared to be symmetric, with a negligible deviation in the strain values. However, this symmetry was reduced as the deviation in strain values of the skins increases. The top skin had a compressive strain of up to  $-0.010$  mm/mm, while the bottom skin exhibited a tensile strain of up to  $0.007$  mm/mm. The different strain values in the top and bottom skins during loading could be due to different dimensions of skin thicknesses, as discussed in the previous section. These findings indicated that the skins resisted the in-plane normal stresses resulting from transverse loading, while the core region resisted shear stresses. These findings would help to understand the crack initiation and propagation mechanisms during flexural testing,

as axial stress concentration near load application points or shear stress in the core region could initiate different fracture mechanisms, such as skin failures, core failures, or core-to-skin failures.

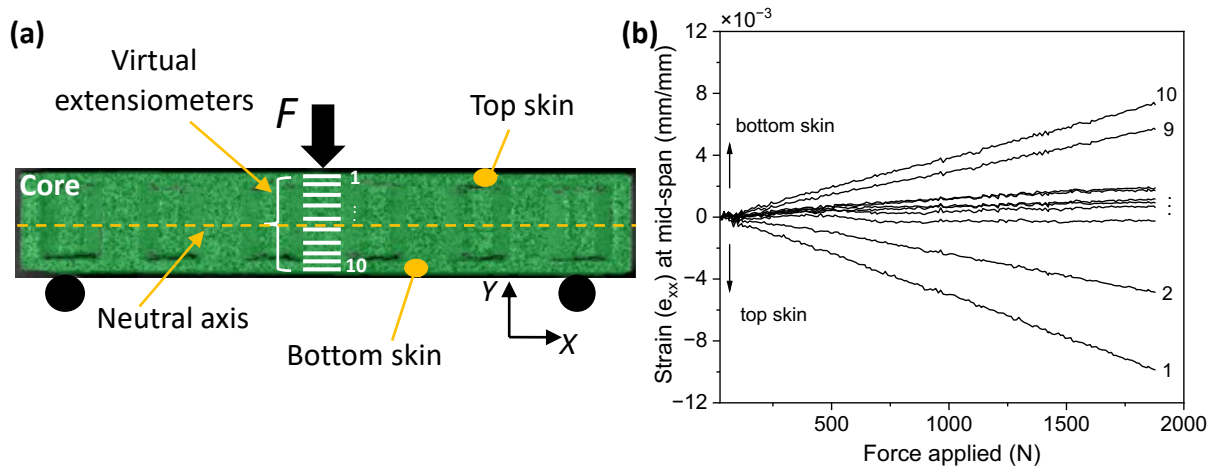


Figure 7.6 (a) DIC strain map of a sandwich panel printed with PEI/rCF/TB(80/20/00) prior to the application of the bending force in which the color scale indicates the magnitude of strain, (b) corresponding strain graph after applied bending force, showing the value of compression strain in the top skin and tensile strain in the bottom skin.

#### 7.4.4 Flexural properties of FFF printed sandwich panels

**Figure 7.7** presents the DIC analysis of the three-point bending results for sandwich panels printed with PEI/rCF /TB (80/20/00) composite filament. **Figure 7.7(a)** shows a series of DIC images showing full-field strain measurement of  $e_{yy}$  with respect to the applied load. The first image, indicated by green color, shows no strain at zero load, while the DIC system detected strain measurement through the surface with increasing load. **Figure 7.7(b)** shows the typical force-displacement curve of the sandwich panel specimens during flexural testing. In **Figure 7.7(a)** and **7.7(b)**, the DIC images correspond to specific force values indicated on the force-displacement curve. Each image is labeled from I to VII, matching its position on the curve. **Figures 7.7(c)** and **7.7(d)** show the DIC image indicating the crack initiation and strain concentration at the core prior to crack formation with an image of the failed sandwich panel after testing, respectively. Analyzing the shape of the force-displacement curves and the full-field strain recorded with the DIC system allowed the detection of damage phenomena during flexural testing. It can be seen that the sandwich panel body experienced a negative strain due to displacement in the  $Y$  axis. With the increment of the load, there was a strain concentration near the neutral axis symmetrically on two sides of the sandwich panel. This positive strain concentration could be due to shear forces that

reached a maximum value at the core region near the neutral axis. This strain concentration was becoming more severe with increasing load and resulted in crack initiation in the core region. In **Figure 7.7(e)**, when the load reached the maximum value, the crack propagated between the layers and resulted in the failure of this panel specimens.

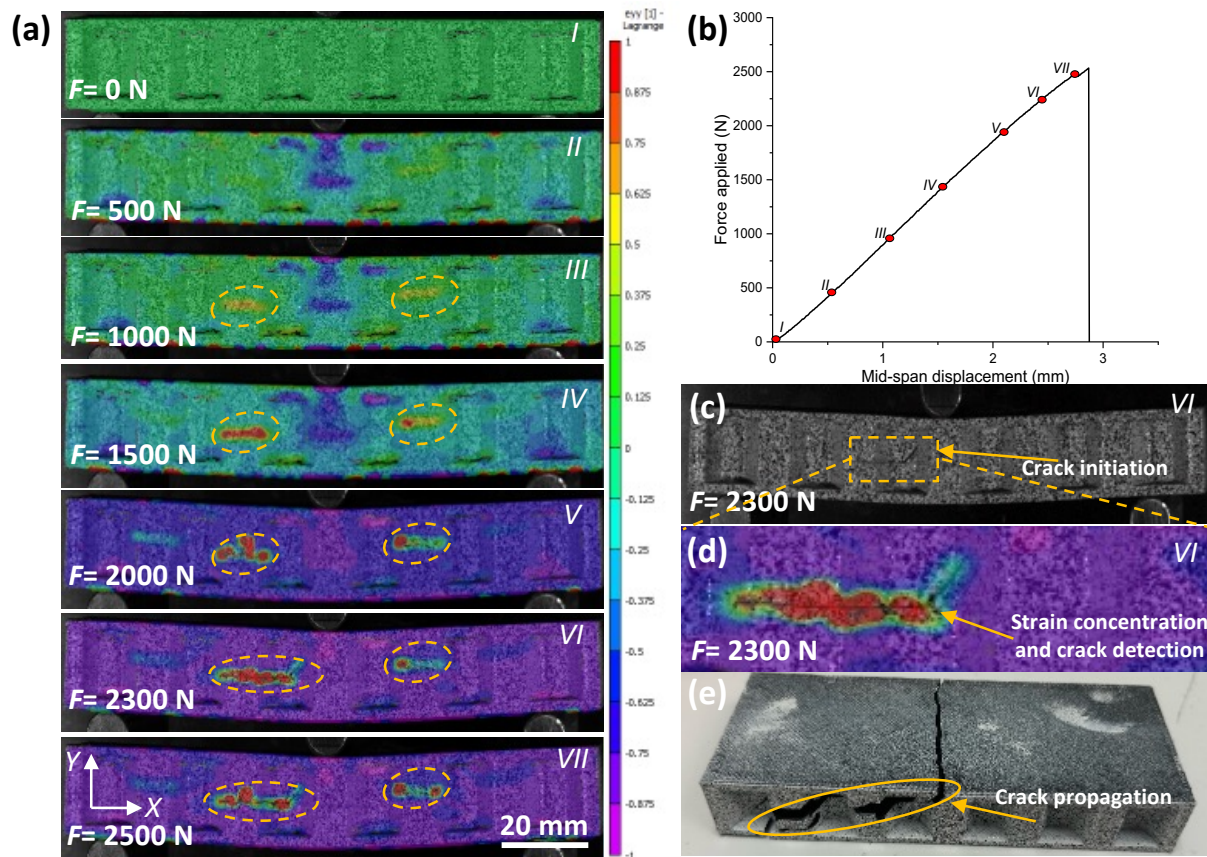


Figure 7.7 DIC analysis of three-point bending results of sandwich panel printed with PEI/rCF/TB (80/20/00) composite filament: (a) a series of DIC images showing the evolution of strain with respect to the applied load, (b) load-displacement curve showing the mechanical response of the sandwich panel during flexural testing. (c) DIC raw image for crack initiation, which is indicated by the yellow circle, (d) DIC image presenting the strain concentration at the core prior to the crack formation (e) post-mortem analysis of crack propagation in the sandwich panel core.

**Figure 7.8** shows the typical force-displacement curve during flexural testing which reflects the mechanical response of at least three sandwich panel specimens printed under the same conditions and materials. All specimens exhibited linear behavior up to the maximum load point, followed by failure. The trend of these experimental curves indicated the repeatability of the tests. The force-displacement curve showed linear behavior up to the maximum load, indicating that the core and skin experienced elastic deformation at this stage. The observed linear behaviour suggests the

absence of debonding between the core and skin or inter-layer debonding within the core. The observation regarding the absence of debonding was also in agreement with the DIC measurements where no strain concentration was observed at the core-skin interface, which would have been observed should there was any debonding.

As the deflection increased with loading, strain concentration was detected in the core, leading to crack initiation and subsequent catastrophic failure, evidenced by the sudden drop in load. The failure after maximum load was catastrophic, resulted in brittle fracture and the specimen's explosion. The crack initiation was detected with the DIC system, and post-mortem analysis revealed the crack propagation pattern, which propagated diagonally through the core, jumping between layers and leading to the failure of the top skin as well. The main reason for the failure was crack formation due to strain concentration in the core for all specimens. The similar crack propagation patterns of failed specimens are indications of repeatable printing parameters, which allows a predictable failure mechanism of the printed sandwich panels. According to the experimentally determined force-displacement curves and damage evolution examinations, the failure behavior of the sandwich panels indicates a good level of layer adhesion in the core regions. There is adequate adhesion at the skin and core interface, which is evident by no debonding between the core and skins. However, enhancing adhesion between the core layers could shift the failure to the skin, thus maximizing the efficiency of the panel.

**Table 7.6** presents the mechanical properties of the sandwich panels extracted from the force-displacement curves. The FFF printed sandwich panels showed repeatable flexural testing results for all formulations, indicated by the confidence interval of the results. Sandwich panels printed with developed PEI composites of rCF/TB (20/00) and rCF/TB (10/10) had average maximum loadings of 2.3 kN and 1.7 kN, respectively. The sandwich panel printed with commercial PEI filaments showed a relatively higher maximum loading capacity of 3.0 kN. However, sandwich panels made of rCF/TB (20/00) composites had a similar flexural stiffness value of 0.94 kN/mm as the sandwich panels printed with commercial PEI filaments. The sandwich panels printed with rCF/TB (20/00) and rCF/TB (10/10) PEI composites exhibited a core shear modulus that is up to twice as high as those made with commercial filaments, but their core shear strength values were relatively lower.



Sandwich panels printed with PPS composites of rCF/TB (20/00) and rCF/TB (10/10) presented average maximum loadings of 2.8 kN and 2.9 kN, respectively. The sandwich panel printed with commercial PPS filaments showed a relatively higher maximum loading of 3.3 kN. Sandwich panels printed with PPS composites of rCF/TB (20/00) and rCF/TB (10/10) had higher flexural stiffness values of 1.44 kN/mm and 1.38 kN/mm, respectively, when compared to specimens printed with commercial PPS composites which had flexural stiffness value of 1.28 kN/mm. The sandwich panels printed with rCF/TB (20/00) and rCF/TB (10/10) composites presented a core shear modulus that is more than two-fold, when compared to those made with commercial filaments, while their core shear strength values remained slightly lower.

The developed composite filaments used in this study present a strong alternative to commercial filaments for engineering applications. They presented higher stiffness and shear modulus, while also offering sustainable characteristics that enhance their appeal for environmentally responsible manufacturing.

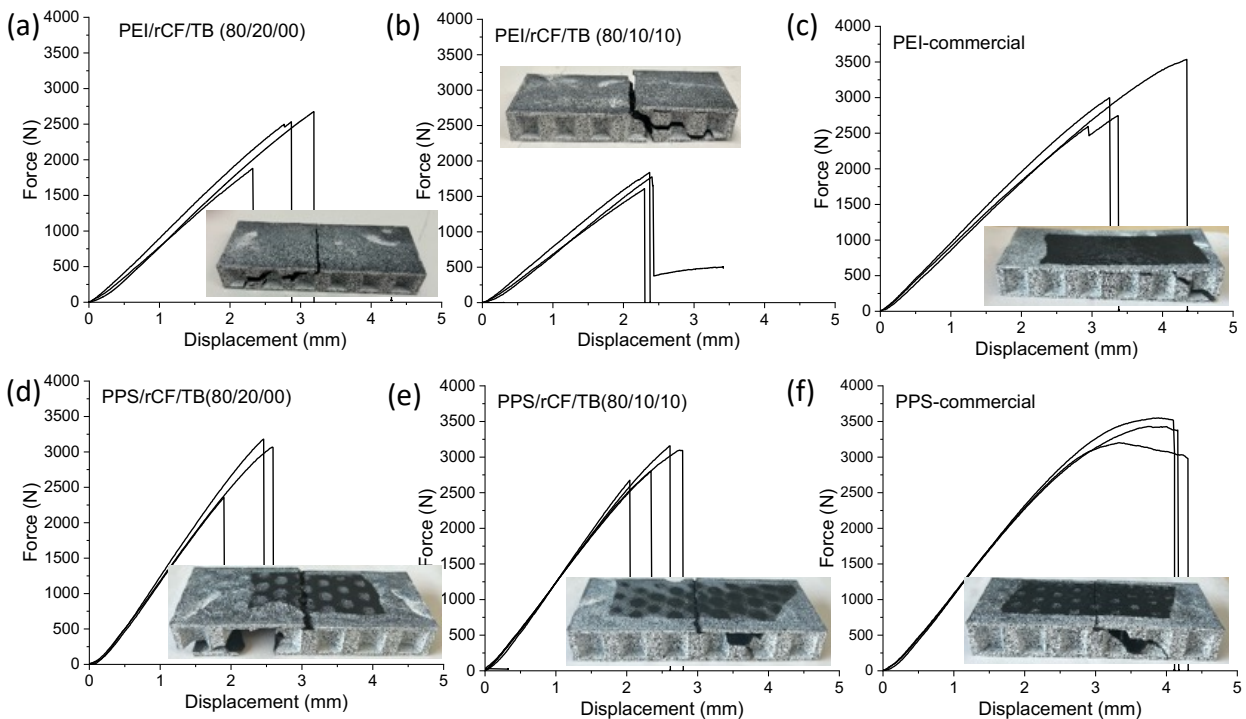


Figure 7.8 Force-displacement curves showing the mechanical response of the sandwich panels during flexural testing with images of failed specimens at maximum load showing the post-mortem analysis of crack propagation in the sandwich panels.

Table 7.6 Mechanical properties comparison of sandwich panels including maximum load, flexural stiffness, maximum displacement, core shear modulus, and core shear strength as computed from the results of flexural testing results based on ASTM standards. The average values are reported with CI of 95 % in the parentheses.

<b>Property / Formulation</b>	<b>PEI/rCF/TB (80/20/00)</b>	<b>PEI/rCF/TB (80/10/10)</b>	<b>PEI-commercial</b>
Maximum load (kN)	2.3 (0.19)	1.7 (0.05)	3.0 (0.21)
Flexural stiffness (kN/mm)	0.94 (0.027)	0.80 (0.023)	0.93 (0.002)
Maximum displacement (mm)	2.75 (0.9)	2.35 (0.2)	3.63 (1.4)
$D$ (kNmm <sup>2</sup> )	29985	29843	60962
$U$ (kN)	72	47	32
Core shear modulus (MPa)	80	53	36
Core shear strength (MPa)	1.41	1.04	1.82
<b>Property / Formulation</b>	<b>PPS/rCF/TB (80/20/00)</b>	<b>PPS/rCF/TB (80/10/10)</b>	<b>PPS-commercial</b>
Maximum load (kN)	2.8 (0.19)	2.9 (0.09)	3.3 (0.08)
Flexural stiffness (kN/mm)	1.44 (0.029)	1.38 (0.024)	1.28 (0.013)
Maximum displacement (mm)	2.30 (0.9)	2.42 (0.5)	4.15 (0.3)
$D$ (kNmm <sup>2</sup> )	42248	38207	32253
$U$ (kN)	11	13	54
Core shear modulus (MPa)	128	152	61
Core shear strength (MPa)	1.73	1.76	2.03

## 7.5 Conclusion

In this study, FFF printed sandwich panels were printed and characterized by using novel formulations of high-temperature composites based on PEI and PPS containing rCF and TB. The flexural properties of sandwich panels were compared with commercial PEI and PPS filaments. Sandwich panel specimens were printed by using an open-source 3D printer equipped with a high-temperature closed chamber. The printed sandwich panels were characterized in terms of dimensional stability, microstructure, and flexural properties. The 3D scanning results showed accurate dimensional stability of the FFF printed sandwich panels when compared to the CAD file, as over 90 % of the C2M distance values deviated by less than 0.2 mm. Sandwich panels printed with PEI composites exhibited up to ~ 12 % porosity on the top skins, while those printed with PPS composites showed up to ~ 8 % porosity. The porosity content on the top skins was also found to be higher than that of the bottom skin for all formulations due to absence of a cooling system which resulted in inconsistency in bridging. No detectable porosity was found on the core wall of the sandwich panels, indicating good layer adhesion between successive layers.

The force-deflection behavior, strength, stiffness, and failure mode of the specimens were evaluated. Crack initiation during flexural testing was detected with the DIC system. The major failure mode observed was core failure and this was consistent across all specimens tested. The

core failure is an indication of good layer-to-layer and core-to-layer adhesion.

The flexural properties of sandwich panels printed with developed filaments were comparable to those printed with commercial filaments, with a bending load capacity of up to 3.0 kN for specimens weighted approximately 50 g. PEI sandwich panels, with a density of 384 kg/m<sup>3</sup>, exhibited a core shear strength of up to 1.4 MPa and a core shear modulus of up to 80 MPa. Similarly, PPS sandwich panels, with a density of 386 kg/m<sup>3</sup>, exhibited a core shear strength of up to 1.7 MPa and a core shear modulus of up to 128 MPa. The core shear modulus results of sandwich panels printed with developed filaments was approximately twice as high as that of the panels printed with commercial filaments.

In conclusion, the novel formulations of composites based on PEI and PPS matrices exhibited good printability and flexural mechanical performance. Considering the performance of the printed sandwich panels, these results are promising, as they are comparable to commercial filaments. Therefore, our study suggests that these composites could be eventually considered for applications of ground transportation and aerospace industry such as interior parts, along with leveraging the flexibility of printing complex core geometries by using FFF that cannot be made with other manufacturing methods.



## CHAPTER 8      GENERAL DISCUSSION

The choice to work in this research project with rCF and TB provided more sustainable and cost reduction perspectives. The virgin CF production is known to be quite energy-intensive (183–286 MJ/kg) and a relatively expensive additive ( $\sim 60$  \$/kg). In contrast, rCF and TB are less expensive ( $\sim 17$  \$/kg for rCF and  $\sim 2$  \$/kg for TB), when compared to virgin CF, to neat PEI, and to neat PPS prices. While the overall cost of the developed composite filaments was not calculated, (not an objective for this work being a complex evaluation process that includes many factors, such as energy consumption, labor time and cost, materials costs etc.), it can be said the simple replacement of 20 wt.% of expensive materials by 20 wt.% of rCF and TB, surely is a cost-effective solution. Moreover, the developed composites are recyclable due to their thermoplastic nature, allowing them to be reused by mechanical recycling as industrial manufacturing waste or at the end of their service life. A small trail was already done during this project and a recycled filament of PPS rCF/TB (10/10) was re-manufactured using granulates obtained from mechanically grinding of broken specimens after their mechanical testing (**Figure 8.1(a)**). This mechanical treatment enables printed parts to be recycled and repurposed again for FFF or for other printing technologies as well, such as granules for fused granule fabrication (FGF). Conducting a life cycle assessment (LCA) for these thermoplastic composites would provide a clearer understanding of their environmental impact, particularly in terms of using rCF and TB compared to virgin carbon fiber.

Chapter 5 and 6 disclosed the primary reason of the presence of intra-layers porosity in the filaments and printed parts being the incorporation of rCF due to degradation of the sizing material normally added on the surface of rCF by their manufacturer (**Figure 8.1(b)**). But, the content of this sizing was reported by its manufacturer to be up to 3.5%, therefore is a reduced quantity. Other factors that possibly can contribute to the intra-layer porosity could be an inadequate polymer drying before its processing at high temperatures or some inconsistency in the printer functioning. Additionally, the addition of rCF increased the matrix viscosity (**Figure 8.1(c)**), which may trap gas produced during processing. Similar levels of porosity were also observed in commercial PEI and PPS composite filaments. Moreover, for the same formulations, but in IM specimens, porosity was very low, only  $\sim 1\%$  due to the high pressure applied during injection of the melt, allowing more efficient compression and degassing compared to FFF. The results and observations regarding FFF printed parts, IM parts, and commercial filaments suggest that the presence of porosity with CF addition is a difficult problem to avoid with the current FFF technology. Using

CF without surface sizing or a sizing material more stable at PEI and PPS processing temperatures would possibly help to reduce porosity. Another method to reduce porosity without material modification could be using a consolidation tool to apply physical pressure on the deposited layer to help eliminate trapped gasses.

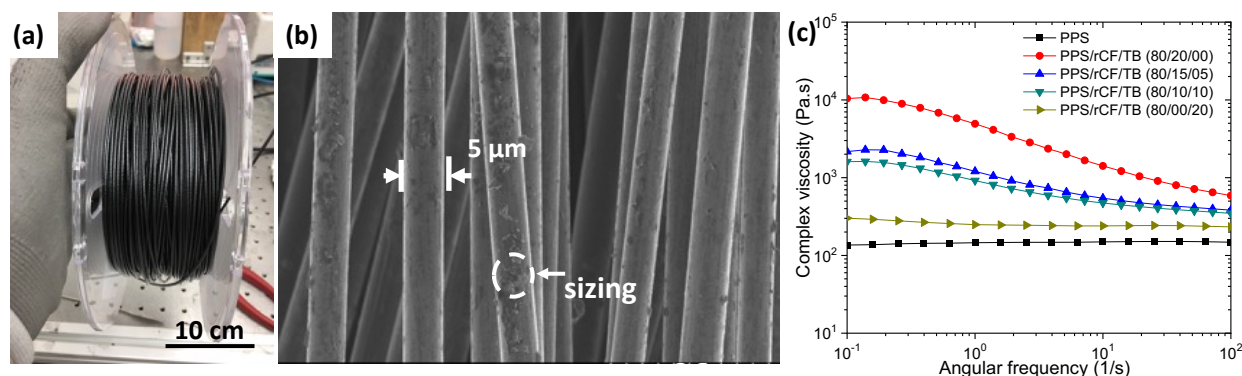


Figure 8.1 (a) Image of the recycled filament spool of PPS composites containing rCF/TB (10/10) that was recycled by mechanically grinding the previously tested mechanical specimens into pellet size. These pellets were then fed into a single-screw extruder, transforming them into filaments suitable for FFF printing, (b) SEM images of the rCF revealed the presence of surface sizing, (c) the frequency sweep test for the PPS composites demonstrated that the incorporation of rCF and TB led to an increase in viscosity, which can impact the presence of porosity.

The rCF length was reduced from an initial 6 mm down to an average of  $\sim 30 - 50 \mu\text{m}$ . It was found that the most significant step for fiber length reduction was during the first compounding step in the twin-screw extruder due to high shear rates, while filament extrusion and FFF printing further reduced fiber length, but to a lesser extent. The IM specimens generally had longer fibers and more aligned fibers in the injection direction compared to FFF printed specimens. In PEI composites, the addition of TB further reduced the average rCF length and hindered the alignment of rCF in both IM and FFF printed specimens. However, in PPS composites containing TB particles, the average rCF length was slightly higher, when compared to rCF length observed in IM specimens. No significant effect on the fiber length was observed after the FFF printing, where all the formulations exhibited a similar average fiber length. Similar to the PEI composites, the addition of TB in PPS composites restricted further alignment during both injection molding and FFF printing. This could be due to the high number of interactions between the TB particles and rCF, which likely altered the matrix viscosity. Clear interactions between rCF and TB were visualized in SEM images, as reported in Chapters 5 and 6, for both matrices. It appears that combining rCF and TB enhances fiber-matrix adhesion, which could potentially influence the observed fiber length

distribution and alignment. However, to quantify this effect and gain a deeper understanding of the underlying mechanisms, further research is required.

For the PPS composites, the 3D printer was used at a maximum chamber temperature limit of 135 °C. A chamber temperature beyond 100 °C could not be used due to a technical issue. The problem was that the print head and the gear responsible for filament feeding into the heated nozzle are located inside the printing chamber. At chamber temperatures above 100 °C, the filament became significantly more ductile due to its  $T_g$  (~ 90 °C), making it difficult to feed the filament into the printer. In Chapter 6, the crystallization studies showed that the environmental printing temperature used in this study may not be sufficient to ensure efficient layers adhesion for improving the mechanical performance. Crystallization of PPS, known for its high crystallization speed, happened before layers deposition and it triggered weak interfaces between deposited layers by inhibiting molecular diffusion during printing and making the mechanical performance of FFF printed parts highly dependent on PPS crystallization kinetics. Isothermal crystallization studies conducted at temperatures ranging from 190 °C to 260 °C suggest that the printing chamber temperature of ~ 240 - 250 °C would significantly contribute to layers adhesion. This range of chamber temperature, higher than the  $T_c$  of PPS composites observed during the cooling, will avoid the PPS composite melt to crystallize before layers deposition while increasing its crystallization half time. Moreover, conventional DSC does not allow full control over crystallization during cooling, as its maximum cooling rate is approximately 1.2 °C/s, while some studies have shown that the critical cooling rate to achieve fully amorphous PPS is approximately 40 °C/s. Therefore, using flash DSC could provide more insight into mimicking FFF printing conditions and into a more detailed evaluation of crystallization kinetics for PPS composites. This being said, the PPS by its innate behaviour remains a highly crystalline thermoplastic having a rapid crystallization rate.

Working with high-temperature 3D printers and composites presented numerous challenges, significantly affecting the overall efficiency of printing. The fastest printing speed it could achieve was 50 mm/s. For example, according to slicing software, each specimen should take, in average, 30 minutes to be printed. However, actual printing time was much longer. Printing a set of five testing specimens for each formulation could take up to a full day due to technical issues, such as nozzle blockage, filament breakage, warping, adhesion issues to the print bed, printer miscalibration during printing, and prolonged waiting times for the chamber to stabilize after each

failed print. These challenges were particularly pronounced for sandwich panels printings, where each specimen took approximately 3 to 5 hours, allowing for only one successful print per day.

Clearly, the current 3D printing technology, such the open-source FFF, needs new developments to further be able to mitigate these problems. New-generation printers seems to feature AI-assisted print failure detection, filament break detection, higher chamber temperatures with adjustable volumes for faster heating, and automated filament feeding systems. These technological advancements could significantly improve the reliability and speed of high-temperature printing processes.

Despite all the encountered issues and challenges, all development novel composites in this PhD research study proved to be promising candidates for FGF, as well. Unlike FFF, FGF can significantly reduce printing time due to its higher extrusion rate and can avoid the extra steps and challenges related to filament production, such as ensuring a consistent diameter and an easy spooling. With FGF, the filler content can potentially be increased beyond the 20 wt.%.

The developed PEI and PPS composites inherently provide exceptional thermal stability and flame retardancy. Preliminary investigations showed that incorporating rCF and TB did not compromise these properties. **Appendix B** presents the thermal characterization results for PEI and its composites, along with Flame Smoke Toxicity (FST) testing results for both PEI and PPS composites. These tests demonstrated that the developed composites meet FST criteria, making them suitable for use in aerospace and ground transportation industries.

## CHAPTER 9 CONCLUSION AND RECOMMENDATIONS

This thesis identifies the challenges in developing amorphous PEI and semi-crystalline PPS matrices with the incorporation of rCF and TB for FFF applications. By employing complementary characterization methods, this work research and its results bridge the gap between the differences in mechanical performance of FFF printed parts and those produced by conventional manufacturing methods while taking into account the behaviours of amorphous and semi-crystalline matrices. The investigated properties of these novel composites include morphological, microstructural, crystallization behaviours, tensile, flexural, impact, and HDT properties. The outcomes of these investigations are as follows:

- Eight (8) different composite formulations, 20 wt.% rCF, 20 wt.% of TB particles, or combinations of 20 wt.% rCF and TB, were manufactured using PEI and PPS as matrices. These concentrations are higher than the currently available commercial PEI and PPS composites, that rarely goes up to 15 wt.%.
- The FFF printing parameters were tuned to reduce the porosity content. The porosity content of FFF printed PEI and PPS specimens with rCF/TB (00/20) was evaluated at  $\sim 2.8$  and  $2.2$  %, respectively, while IM specimens shown  $\sim 1$  % of porosity. The porosity content went up to a maximum of  $16.8$  % and  $9.2$  % for PEI and PPS containing rCF/TB (20/00), respectively.
- The average fiber length was computed and found to vary between  $30 - 50$   $\mu\text{m}$  for both PEI and PPS composites. IM specimens exhibited relatively higher average fiber lengths compared to FFF printed specimens.
- Crystallization studies showed that crystallinity of neat PPS significantly reduced from  $93.5$  % down to  $\sim 40$  % for IM specimens with rCF and TB incorporation. The IM specimens exhibited higher crystallinity of ranging  $37 - 43$  %, when compared to FFF printed specimens were the crystallinity limited at  $31 - 36$  %.
- Isothermal crystallization studies conducted on PPS composites at temperatures ranging from  $190$   $^{\circ}\text{C}$  to  $260$   $^{\circ}\text{C}$  showed that with increasing the temperature of the isothermal step the crystallinity content and the crystallization half time increased for all PPS composites formulations. The crystallization kinetic results suggest that the printing chamber temperature between  $240 - 250$   $^{\circ}\text{C}$  should contribute to layers adhesion and to the

enhancement of the mechanical properties. It seems that delaying the crystallization after the layer deposition would promote more macromolecular chains diffusion and a mutual crystallization between two adjacent layers.

- FFF printed PEI containing rCF/TB (20/00), rCF/TB (15/05), rCF/TB (10/10), and rCF/TB (00/20) exhibited a TS of 70 MPa, 69 MPa, 64 MPa, and 40 MPa and a TM of 4.23 GPa, 4.20 GPa, 4.21 GPa, and 4.14 GPa, respectively. Similarly, the same formulations of IM specimens exhibited a TS of 103 MPa, 88 MPa, 82 MPa, and 42 MPa and a TM of 6.18 GPa, 4.35 GPa, 3.57 GPa, and 4.07 GPa, respectively. For all formulations, FFF printed specimens showed approximately 30 % higher TM, when compared to IM neat PEI.
- FFF printed PPS containing rCF/TB (20/00), rCF/TB (15/05), rCF/TB (10/10), and rCF/TB (00/20) exhibited a TS of 68 MPa, 66 MPa, 65 MPa, and 45 MPa and a TM of 5.96 GPa, 5.73 GPa, 5.39 GPa, and 5.26 GPa, respectively. Similarly, the same formulations of IM specimens exhibited a TS of 151 MPa, 130 MPa, 105 MPa, and 62 MPa and a TM of 19.9 GPa, 17.2 GPa, 13.4 GPa, and 5.0 GPa, respectively. Moreover, for all formulations, FFF printed specimens showed approximately 60 % higher TM, when compared to IM neat PPS.
- PEI and PPS composites exhibited a heat deflection temperature (HDT) of up to 200 °C and 270 °C, respectively. Considering the service temperature requirements for Nomex (up to 180 °C) or Aluminum honeycombs, these novel performant PEI and PPS formulations demonstrate a significant potential to be used in the same applications as Nomex or other commercial materials.
- PEI sandwich panels, with a density of 384 kg/m<sup>3</sup>, exhibited a core shear strength of up to 1.4 MPa and a core shear modulus of up to 80 MPa. Similarly, PPS sandwich panels, with a density of 386 kg/m<sup>3</sup>, exhibited a core shear strength of up to 1.7 MPa and a core shear modulus of up to 128 MPa. These results are promising, as they are comparable to commercial Nomex cores, which are reported to have a shear modulus of up to 112 MPa and a core shear strength of up to 3.2 MPa for cores with a density of 129 kg/m<sup>3</sup>.
- Crack initiations, occurred due to the strain concentration in the core region, were detected using a DIC system. The observed failure mode was consistent across all specimens, demonstrating a high quality for the novel composites, a high print quality, and a strong layer adhesion in the sandwich panel specimens.

Future work on the following issues may further advance this field:

- It was observed that the intra-layer porosity formation could be due to the degradation of the sizing material, normally present on the surface of rCF. In this context, using carbon fiber with sizing material that have thermal stability at high processing temperatures of PEI and PPS could help to reduce porosity content.
- It was demonstrated that FFF printed specimens generally exhibited equivalent mechanical performance compared to IM neat matrices. But some formulations still have the potential for improvement to match their IM composite counterparts. In this context, a printer with a more control of its thermal environment could be used to print specimens at higher chamber temperatures. This will allow to investigate of how higher chamber temperatures would fingerprint the mechanical performance. In this study, the maximum chamber temperature was limited at 135 °C by its manufacturer.
- The effect of the FFF 3D printing and of IM process on the crystallization behavior of the novel PPS composites was studied using conventional DSC, which is limited by maximum cooling and heating rates. A more robust method, such as flash DSC, could be implemented to study the effect of thermal history on the microstructure and mechanical properties of PPS composites.
- The flexural properties of FFF printed sandwich panels were investigated at room temperature and compared with sandwich panels made from commercial filaments. Future research on the investigation mechanical properties variations at lower / higher temperatures, such as the real temperatures encountered during their utilization in planes environment. Also, exploring the impact and fatigue properties of these panels and comparing them to those of commercial Nomex or Al honeycomb sandwich panels would provide valuable insights into their potential to be used in other application areas.
- Flexural mechanical properties were calculated using analytical equations based on ASTM standards, assuming homogeneous material geometry. However, more realistic results could be obtained by implementing numerical analysis methods to identify stress distribution during flexural testing, particularly in the skin and core regions, considering the layered structure of FFF printed parts.
- Conducting a life cycle assessment and evaluating the recyclability of the developed composites., or using Artificial Intelligence tools (Machine Learning, Deep Learning, etc) for FFF printing of novel materials.

## REFERENCES

1. <https://www.marketsandmarkets.com/Market-Reports/3d-printing-market-1276.html>.
2. Grünewald, J., P. Parlevliet, and V. Altstädt, *Manufacturing of thermoplastic composite sandwich structures: A review of literature*. Journal of Thermoplastic Composite Materials, 2017. **30**(4): p. 437-464.
3. Karlsson, K.F. and B. TomasÅström, *Manufacturing and applications of structural sandwich components*. Composites Part A: Applied Science and Manufacturing, 1997. **28**(2): p. 97-111.
4. SABIC, *Engineering Thermoplastics Product Guide*.
5. <https://www.celanese.com/products/fortron-polyphenylene-sulfide>.
6. <https://www.ensingerplastics.com/en/filaments/tecafil-peek-vx-cf30-black-1-75-mm>.
7. <https://www.3dxtech.com/products/carbonx-peek-cf20-1>.
8. Sola, A., *Materials requirements in fused filament fabrication: a framework for the design of next-generation 3D printable thermoplastics and composites*. Macromolecular Materials and Engineering, 2022. **307**(10): p. 2200197.
9. Rafiee, M., R.D. Farahani, and D.J.A.S. Therriault, *Multi-Material 3D and 4D Printing: A Survey*. 2020. **7**(12): p. 1902307.
10. Penumakala, P.K., J. Santo, and A.J.C.P.B.E. Thomas, *A critical review on the fused deposition modeling of thermoplastic polymer composites*. 2020: p. 108336.
11. Rahim, T.N.A.T., A.M. Abdullah, and H. Md Akil, *Recent developments in fused deposition modeling-based 3D printing of polymers and their composites*. Polymer Reviews, 2019. **59**(4): p. 589-624.
12. Irving, P.E. and C. Soutis, *Polymer composites in the aerospace industry*. 2019: Woodhead Publishing.
13. Jayakrishna, K., et al., *Materials selection for aerospace components*, in *Sustainable composites for aerospace applications*. 2018, Elsevier. p. 1-18.
14. Soutis, C., *Aerospace engineering requirements in building with composites*, in *Polymer Composites in the Aerospace Industry*. 2020, Elsevier. p. 3-22.
15. Witik, R.A., et al., *Carbon fibre reinforced composite waste: An environmental assessment of recycling, energy recovery and landfilling*. Composites Part A: Applied Science and Manufacturing, 2013. **49**: p. 89-99.
16. Stoeffler, K., et al., *Polyphenylene sulfide (PPS) composites reinforced with recycled carbon fiber*. Composites Science and Technology, 2013. **84**: p. 65-71.
17. Zhang, J., et al., *Current status of carbon fibre and carbon fibre composites recycling*. Composites Part B: Engineering, 2020. **193**: p. 108053.
18. Ateeq, M., et al., *A review of 3D printing of the recycled carbon fiber reinforced polymer composites: Processing, potential, and perspectives*. journal of materials research and technology, 2023.



19. Huang, H., W. Liu, and Z. Liu, *An additive manufacturing-based approach for carbon fiber reinforced polymer recycling*. CIRP Annals, 2020. **69**(1): p. 33-36.
20. Liu, W., et al., *Integrating carbon fiber reclamation and additive manufacturing for recycling CFRP waste*. Composites Part B: Engineering, 2021. **215**: p. 108808.
21. Cancarb, P.o.M.C.u.T., Available online: <https://cancarb.com/products/>.
22. Cancarb, E.R., Available online: <https://cancarb.com/products/>.
23. Ziebell, R., M. Rogers, and R.D. Abbott. *Thermal carbon black (N-990) for processing performance in architectural sealing*. 2018. Lippincott and Peto Inc.
24. Mihai, M., K. Stoeffler, and E. Norton, *Use of Thermal Black as Eco-Filler in Thermoplastic Composites and Hybrids for Injection Molding and 3D Printing Applications*. Molecules, 2020. **25**(7): p. 1517.
25. Van de Werken, N., et al., *Additively manufactured carbon fiber-reinforced composites: State of the art and perspective*. Additive Manufacturing, 2020. **31**: p. 100962.
26. Lepoivre, A., et al., *Coalescence in fused filament fabrication process: Thermo-dependent characterization of high-performance polymer properties*. Polymer Testing, 2021. **98**: p. 107096.
27. McIlroy, C. and P. Olmsted, *Disentanglement effects on welding behaviour of polymer melts during the fused-filament-fabrication method for additive manufacturing*. Polymer, 2017. **123**: p. 376-391.
28. Wool, R. and K. O'connor, *A theory crack healing in polymers*. Journal of applied physics, 1981. **52**(10): p. 5953-5963.
29. Sun, Q., et al., *Effect of processing conditions on the bonding quality of FDM polymer filaments*. Rapid prototyping journal, 2008. **14**(2): p. 72-80.
30. Heller, B.P., D.E. Smith, and D.A. Jack, *Effects of extrudate swell and nozzle geometry on fiber orientation in Fused Filament Fabrication nozzle flow*. Additive Manufacturing, 2016. **12**: p. 252-264.
31. Collinson, D.W., et al., *Direct evidence of interfacial crystallization preventing weld formation during fused filament fabrication of poly (ether ether ketone)*. Additive Manufacturing, 2022. **51**: p. 102604.
32. Bhandari, S., R.A. Lopez-Anido, and D.J. Gardner, *Enhancing the interlayer tensile strength of 3D printed short carbon fiber reinforced PETG and PLA composites via annealing*. Additive Manufacturing, 2019. **30**: p. 100922.
33. Yang, D., et al., *Effects of crystallinity control on mechanical properties of 3D-printed short-carbon-fiber-reinforced polyether ether ketone composites*. Polymer Testing, 2021. **97**: p. 107149.
34. Levenhagen, N.P. and M.D. Dadmun, *Improving Interlayer Adhesion in 3D Printing with Surface Segregating Additives: Improving the Isotropy of Acrylonitrile–Butadiene–Styrene Parts*. ACS Applied Polymer Materials, 2019. **1**(4): p. 876-884.

35. Levenhagen, N.P. and M.D. Dadmun, *Interlayer diffusion of surface segregating additives to improve the isotropy of fused deposition modeling products*. Polymer, 2018. **152**: p. 35-41.
36. Rostom, S. and M.D. Dadmun, *Improving heat transfer in fused deposition modeling with graphene enhances inter filament bonding*. Polymer Chemistry, 2019. **10**(44): p. 5967-5978.
37. Brenken, B., et al., *Fused filament fabrication of fiber-reinforced polymers: A review*. Additive Manufacturing, 2018. **21**: p. 1-16.
38. Liao, G., et al., *Properties of oriented carbon fiber/polyamide 12 composite parts fabricated by fused deposition modeling*. Materials & Design, 2018. **139**: p. 283-292.
39. Zhong, W., et al., *Short fiber reinforced composites for fused deposition modeling*. Materials Science and Engineering: A, 2001. **301**(2): p. 125-130.
40. Diouf-Lewis, A., et al., *Design and characterization of carbon fiber-reinforced PEEK/PEI blends for Fused Filament Fabrication additive manufacturing*. Materials Today Communications, 2022. **31**: p. 103445.
41. Kishore, V., et al., *Additive manufacturing of high performance semicrystalline thermoplastics and their composites*. 2016, Oak Ridge National Lab.(ORNL), Oak Ridge, TN (United States).
42. Burgos Pintos, P., et al., *Influence of the Carbon Fiber Length Distribution in Polymer Matrix Composites for Large Format Additive Manufacturing via Fused Granular Fabrication*. Polymers, 2023. **16**(1): p. 60.
43. Consul, P., et al., *Effect of extrusion parameters on short fiber alignment in fused filament fabrication*. Polymers, 2021. **13**(15): p. 2443.
44. Hofstätter, T., et al. *Distribution and orientation of carbon fibers in polylactic acid parts produced by fused deposition modeling*. in *Proceedings of ASPE summer topical meeting*. 2016.
45. Sharma, R., et al., *Short carbon fiber-reinforced polycarbonate composites*, in *Composite Materials*. 2017, Springer. p. 199-221.
46. Tekinalp, H.L., et al., *Highly oriented carbon fiber–polymer composites via additive manufacturing*. Composites Science and Technology, 2014. **105**: p. 144-150.
47. Walter, R., et al., *Effect of filament quality, structure, and processing parameters on the properties of fused filament fabricated short fiber-reinforced thermoplastics*, in *Structure and Properties of Additive Manufactured Polymer Components*. 2020, Elsevier. p. 253-302.
48. Chuang, K.C., et al. *Additive manufacturing and characterization of Ultem polymers and composites*. in *Proceedings of the CAMX Conference, Dallas, TX, USA*. 2015.
49. Al-Maharma, A.Y., S.P. Patil, and B. Markert, *Effects of porosity on the mechanical properties of additively manufactured components: a critical review*. Materials Research Express, 2020. **7**(12): p. 122001.

50. Wang, X., et al., *Effect of porosity on mechanical properties of 3D printed polymers: Experiments and micromechanical modeling based on X-ray computed tomography analysis*. Polymers, 2019. **11**(7): p. 1154.
51. Hergenrother, P.M., *The use, design, synthesis, and properties of high performance/high temperature polymers: an overview*. High Performance Polymers, 2003. **15**(1): p. 3-45.
52. Ramgobin, A., G. Fontaine, and S. Bourbigot, *Thermal degradation and fire behavior of high performance polymers*. Polymer Reviews, 2019. **59**(1): p. 55-123.
53. Boyer, R., et al., *Materials considerations for aerospace applications*. MRS Bulletin, 2015. **40**(12): p. 1055-1066.
54. de Leon, A.C., et al., *High performance polymer nanocomposites for additive manufacturing applications*. 2016. **103**: p. 141-155.
55. <https://www.3dxtech.com/products/>.
56. Wu, H., et al., *Multi-functional ULTEM™ 1010 composite filaments for additive manufacturing using Fused Filament Fabrication (FFF)*. Additive Manufacturing, 2018. **24**: p. 298-306.
57. Taylor, G., et al., *Flexural behavior of additively manufactured Ultem 1010: experiment and simulation*. Rapid Prototyping Journal, 2018.
58. Taylor, G., et al., *Fracture toughness of additively manufactured ULTEM 1010*. Virtual and Physical Prototyping, 2019. **14**(3): p. 277-283.
59. Schöppner, V. and K.P. KTP. *Mechanical properties of fused deposition modeling parts manufactured with Ultem\* 9085*. in *Proceedings of the 69th Annual Technical Conference of the Society of Plastics Engineers (ANTEC'11)*, Boston, MA, USA. 2011.
60. Zaldivar, R., et al., *Influence of processing and orientation print effects on the mechanical and thermal behavior of 3D-Printed ULTEM® 9085 Material*. Additive Manufacturing, 2017. **13**: p. 71-80.
61. Zaldivar, R., et al., *Effect of initial filament moisture content on the microstructure and mechanical performance of ULTEM® 9085 3D printed parts*. Additive Manufacturing, 2018. **24**: p. 457-466.
62. Padovano, E., et al., *Mechanical and thermal behavior of ultem® 9085 fabricated by fused-deposition modeling*. Applied Sciences, 2020. **10**(9): p. 3170.
63. Shelton, T.E., et al., *Effects of thermal process parameters on mechanical interlayer strength for additively manufactured Ultem 9085*. Polymer Testing, 2020. **81**: p. 106255.
64. Tosto, C., et al., *Methods for the characterization of polyetherimide based materials processed by fused deposition modelling*. Applied Sciences, 2020. **10**(9): p. 3195.
65. Volkov, Y.M., et al., *Effect of a Temperature on the Mechanical Characteristics of ULTEM 9085 Thermoplastic Produced by Additive Technology*. Strength of Materials, 2020. **52**(3): p. 414-418.
66. Gebisa, A.W. and H.G. Lemu, *Influence of 3D printing FDM process parameters on tensile property of ULTEM 9085*. Procedia Manufacturing, 2019. **30**: p. 331-338.

67. Ajinjeru, C., et al., *The influence of dynamic rheological properties on carbon fiber-reinforced polyetherimide for large-scale extrusion-based additive manufacturing*. The International Journal of Advanced Manufacturing Technology, 2018. **99**(1): p. 411-418.
68. Slonov, A., et al., *The Effect of Modification on the Properties of Polyetherimide and Its Carbon-Filled Composite*. Polymers, 2020. **12**(5): p. 1056.
69. Rahate, A.S., K.R. Nemade, and S.A. Waghuley, *Polyphenylene sulfide (PPS): state of the art and applications*. Reviews in Chemical Engineering, 2013. **29**(6): p. 471-489.
70. MACALLUM, A.D., *A dry synthesis of aromatic sulfides: phenylene sulfide resins*. The Journal of Organic Chemistry, 1948. **13**(1): p. 154-159.
71. Stevens, T., *Polyphenylene sulfide: a breed apart*. Materials engineering, 1990. **107**(2): p. 26-30.
72. Garmabi, M.M., et al., *3D printing of polyphenylene sulfide for functional lightweight automotive component manufacturing through enhancing interlayer bonding*. Additive Manufacturing, 2022. **56**: p. 102780.
73. Geng, P., et al., *Effects of printing parameters on the mechanical properties of high-performance polyphenylene sulfide three-dimensional printing*. 3D Printing and Additive Manufacturing, 2021. **8**(1): p. 33-41.
74. Zirak, N., et al., *Interlayer bonding improvement and optimization of printing parameters of FFF polyphenylene sulfide parts using GRA method*. Progress in Additive Manufacturing, 2024. **9**(2): p. 505-516.
75. Fitzharris, E.R., D.W. Rosen, and M.L. Shofner, *Fast scanning calorimetry for semicrystalline polymers in fused deposition modeling*. Polymer, 2019. **166**: p. 196-205.
76. El Magri, A., et al. *Printing temperature effects on the structural and mechanical performances of 3D printed Poly-(phenylene sulfide) material*. in *IOP Conference Series: Materials Science and Engineering*. 2020. IOP Publishing.
77. Geng, P., et al., *Effect of thermal processing and heat treatment condition on 3D printing PPS properties*. Polymers, 2018. **10**(8): p. 875.
78. Kishore, V., et al., *Post-process annealing of large-scale 3D printed polyphenylene sulfide composites*. Additive Manufacturing, 2020. **35**: p. 101387.
79. Fitzharris, E.R., et al., *Interlayer bonding improvement of material extrusion parts with polyphenylene sulfide using the Taguchi method*. Additive Manufacturing, 2018. **24**: p. 287-297.
80. Yeole, P., et al., *Mechanical characterization of high-temperature carbon fiber-polyphenylene sulfide composites for large area extrusion deposition additive manufacturing*. Additive Manufacturing, 2020. **34**: p. 101255.
81. Krzyżak, A., et al., *Sandwich structured composites for aeronautics: methods of manufacturing affecting some mechanical properties*. International Journal of Aerospace Engineering, 2016. **2016**.

82. Rajkumar, S., et al., *Experimental and finite-element analysis of tee joint's stiffness characteristics of A3003 honeycomb core sandwich panels*. International Journal of Mechanics and Design, 2018. **4**(2): p. 21-29.
83. Zenkert, D., *An introduction to sandwich structures*. 1995.
84. Petras, A., *Design of sandwich structures*. 1998, University of Cambridge.
85. Armstrong, K., D. Stevens, and J. Alet. *25-years of use of Nomex Honeycomb in floor panels and sandwich structures*. in *Proceedings of the 50-Years of Advanced Materials or Back to the Future, SAMPE Conference, Toulouse*. 1994.
86. Castanie, B., C. Bouvet, and M. Ginot, *Review of composite sandwich structure in aeronautic applications*. Composites Part C: Open Access, 2020. **1**: p. 100004.
87. Galatas, A., et al., *Additive manufactured sandwich composite/ABS parts for unmanned aerial vehicle applications*. Polymers, 2018. **10**(11): p. 1262.
88. Turner, A.J., et al., *Low-velocity impact behavior of sandwich structures with additively manufactured polymer lattice cores*. Journal of Materials Engineering and Performance, 2018. **27**(5): p. 2505-2512.
89. Özen, İ., et al., *Low-energy impact response of composite sandwich panels with thermoplastic honeycomb and reentrant cores*. Thin-Walled Structures, 2020. **156**: p. 106989.
90. Ge, L., et al., *Compression behavior of a novel sandwich structure with bi-directional corrugated core*. Thin-Walled Structures, 2021. **161**: p. 107413.
91. Wu, Q., et al., *Mechanical properties and failure mechanisms of sandwich panels with ultra-lightweight three-dimensional hierarchical lattice cores*. International Journal of Solids and Structures, 2018. **132**: p. 171-187.
92. de Castro, B.D., et al., *An Assessment of Fully Integrated Polymer Sandwich Structures Designed by Additive Manufacturing*. Journal of Materials Engineering and Performance, 2021: p. 1-8.
93. Essassi, K., et al., *Experimental and analytical investigation of the bending behaviour of 3D-printed bio-based sandwich structures composites with auxetic core under cyclic fatigue tests*. Composites Part A: Applied Science and Manufacturing, 2020. **131**: p. 105775.
94. Bhate, D., et al., *A validated methodology for predicting the mechanical behavior of ultem-9085 honeycomb structures manufactured by fused deposition modeling*. 2016.
95. Bagsik, A., et al. *Mechanical analysis of lightweight constructions manufactured with fused deposition modeling*. in *AIP Conference Proceedings*. 2014. American Institute of Physics.
96. Pierre, J.M.L., *Fabrication additive de panneaux sandwich multifonctionnels en polymères renforcés résistants à la haute température pour applications aérospatiales*, in *Department of Mechanical Engineering*. 2023, Polytechnique Montréal.
97. Fathi, A., J.-H. Keller, and V. Altstaedt, *Full-field shear analyses of sandwich core materials using Digital Image Correlation (DIC)*. Composites Part B: Engineering, 2015. **70**: p. 156-166.

98. Ogasawara, T., et al., *High-speed observation of bending fracture process of carbon fiber reinforced plastic composite/Nomex™ honeycomb sandwich panel*. Journal of Sandwich Structures & Materials, 2021. **23**(6): p. 1987-1999.
99. Zhang, X., et al., *Study on the bending and shear properties of quasi-honeycomb sandwich structures considering the variable-density core design*. Composite Structures, 2023. **324**: p. 117517.
100. Edelen III, D.L. and H.A. Bruck, *Predicting failure modes of 3D-printed multi-material polymer sandwich structures from process parameters*. Journal of Sandwich Structures & Materials, 2022. **24**(2): p. 1049-1075.
101. Shehab, E., et al., *A cost modelling system for recycling carbon fiber-reinforced composites*. Polymers, 2021. **13**(23): p. 4208.
102. Das, A., et al., *Importance of Polymer Rheology on Material Extrusion Additive Manufacturing: Correlating Process Physics to Print Properties*. ACS Applied Polymer Materials, 2021. **3**(3): p. 1218-1249.
103. Duty, C., et al., *What makes a material printable? A viscoelastic model for extrusion-based 3D printing of polymers*. Journal of Manufacturing Processes, 2018. **35**: p. 526-537.
104. Abderrafai, Y., et al., *Additive manufacturing and characterization of high temperature thermoplastic blends for potential aerospace applications*. Composites Science and Technology, 2023. **231**: p. 109839.
105. Das, A., et al., *Current understanding and challenges in high temperature additive manufacturing of engineering thermoplastic polymers*. Additive Manufacturing, 2020. **34**: p. 101218.
106. Morgret, L.D., K.J. Pawlowski, and J.A. Hinkley, *Electrospinning of Polyvinylidene Fluoride and Polyetherimide From Mixed Solvents*. 2005.
107. Sosa-Rey, F., et al., *OpenFiberSeg: Open-source segmentation of individual fibers and porosity in tomographic scans of additively manufactured short fiber reinforced composites*. Composites Science and Technology, 2022. **226**: p. 109497.
108. Thomason, J.L., et al., *A study of the thermal degradation of glass fibre sizings at composite processing temperatures*. Composites Part A: Applied Science and Manufacturing, 2019. **121**: p. 56-63.
109. Thomason, J., *The influence of fibre length and concentration on the properties of glass fibre reinforced polypropylene: 7. Interface strength and fibre strain in injection moulded long fibre PP at high fibre content*. Composites Part A: applied science and manufacturing, 2007. **38**(1): p. 210-216.
110. Van Ingen, J.W., et al. *Development of the Gulfstream G650 induction welded thermoplastic elevators and rudder*. in *Proceedings of the international SAMPE symposium and exhibition, Seattle, WA, USA*. 2010.
111. Chen, G., A.K. Mohanty, and M. Misra, *Progress in research and applications of Polyphenylene Sulfide blends and composites with carbons*. Composites Part B: Engineering, 2021. **209**: p. 108553.

112. Worrell, E. and M.A. Reuter, *Handbook of Recycling: State-of-the-art for Practitioners, Analysts, and Scientists*. 2014: Newnes.
113. Tao, Y., et al., *A review on voids of 3D printed parts by fused filament fabrication*. Journal of Materials Research and Technology, 2021. **15**: p. 4860-4879.
114. Costa, S., F. Duarte, and J. Covas, *Thermal conditions affecting heat transfer in FDM/FFE: a contribution towards the numerical modelling of the process: This paper investigates convection, conduction and radiation phenomena in the filament deposition process*. Virtual and Physical Prototyping, 2015. **10**(1): p. 35-46.
115. Trofimov, A., et al., *Experimentally validated modeling of the temperature distribution and the distortion during the Fused Filament Fabrication process*. Additive Manufacturing, 2022. **54**: p. 102693.
116. Zhang, J., et al., *Numerical investigation of the influence of process conditions on the temperature variation in fused deposition modeling*. Materials & Design, 2017. **130**: p. 59-68.
117. Ferraris, E., J. Zhang, and B. Van Hooreweder, *Thermography based in-process monitoring of Fused Filament Fabrication of polymeric parts*. CIRP Annals, 2019. **68**(1): p. 213-216.
118. Kishore, V., et al. *Additive manufacturing of high performance semicrystalline thermoplastics and their composites*. in *2016 International Solid Freeform Fabrication Symposium*. 2016. University of Texas at Austin.
119. Fitzharris, E.R., et al., *Effects of material properties on warpage in fused deposition modeling parts*. The International Journal of Advanced Manufacturing Technology, 2018. **95**: p. 2059-2070.
120. DeNardo, N.M., *Additive manufacturing of carbon fiber-reinforced thermoplastic composites*. 2016, Purdue University.
121. Arici, A., et al., *Influence of annealing on the performance of short glass fiber-reinforced polyphenylene sulfide (PPS) composites*. Journal of composite materials, 2005. **39**(1): p. 21-33.
122. Liu, P., et al., *Rheology, crystal structure, and nanomechanical properties in large-scale additive manufacturing of polyphenylene sulfide/carbon fiber composites*. Composites Science and Technology, 2018. **168**: p. 263-271.
123. Zeng, H. and G. Ho, *Investigation on the crystalline morphologies of polyphenylene sulfide and interfacial effect in its fibre composites*. Die Angewandte Makromolekulare Chemie: Applied Macromolecular Chemistry and Physics, 1984. **127**(1): p. 103-114.
124. Desio, G.P. and L. Rebenfeld, *Effects of fibers on the crystallization of poly (phenylene sulfide)*. Journal of applied polymer science, 1990. **39**(4): p. 825-835.
125. Kenny, J. and A. Maffezzoli, *Crystallization kinetics of poly (phenylene sulfide)(PPS) and PPS/carbon fiber composites*. Polymer Engineering & Science, 1991. **31**(8): p. 607-614.
126. Yasuniwa, M., et al., *Crystallization behavior of poly(l-lactic acid)*. Polymer, 2006. **47**(21): p. 7554-7563.

127. Chung, J., J. Bodziuch, and P. Cebe, *Effects of thermal history on crystal structure of poly (phenylene sulphide)*. Journal of materials science, 1992. **27**: p. 5609-5619.
128. Silvestre, C., et al., *Crystallization, morphology, and thermal behavior of poly (p-phenylene sulfide)*. Journal of Polymer Science Part B: Polymer Physics, 2001. **39**(4): p. 415-424.
129. Nohara, L.B., et al., *Study of crystallization behavior of poly (phenylene sulfide)*. Polímeros, 2006. **16**: p. 104-110.
130. Rodzeń, K., et al., *Controlling Crystallization: A Key Factor during 3D Printing with the Advanced Semicrystalline Polymeric Materials PEEK, PEKK 6002, and PEKK 7002*. Macromolecular Materials and Engineering, 2023: p. 2200668.
131. Gao, S.-L. and J.-K. Kim, *Cooling rate influences in carbon fibre/PEEK composites. Part I. Crystallinity and interface adhesion*. Composites Part A: Applied science and manufacturing, 2000. **31**(6): p. 517-530.
132. Lee, A., et al., *Effect of temperature history during additive manufacturing on crystalline morphology of PEEK*. Advances in Industrial and Manufacturing Engineering, 2022. **4**: p. 100085.
133. Dray, D., P. Gilormini, and G. Régnier, *Comparison of several closure approximations for evaluating the thermoelastic properties of an injection molded short-fiber composite*. Composites Science and Technology, 2007. **67**(7-8): p. 1601-1610.
134. Senior, A.B. and T. Osswald, *Measuring fiber length in the core and shell regions of injection molded long fiber-reinforced thermoplastic plaques*. Journal of Composites Science, 2020. **4**(3): p. 104.
135. Bitzer, T., *Honeycomb core*, in *Honeycomb Technology: Materials, Design, Manufacturing, Applications and Testing*. 1997, Springer. p. 10-42.
136. Ward, C., K. Hazra, and K. Potter, *Development of the manufacture of complex composite panels*. International Journal of Materials and Product Technology, 2011. **42**(3-4): p. 131-155.
137. Hou, Z., et al., *3D printed continuous fibre reinforced composite corrugated structure*. Composite Structures, 2018. **184**: p. 1005-1010.
138. Pierre, J., et al., *Material extrusion additive manufacturing of multifunctional sandwich panels with load-bearing and acoustic capabilities for aerospace applications*. Additive Manufacturing, 2023. **61**: p. 103344.
139. de Dios Rodriguez-Ramirez, J., B. Castanie, and C. Bouvet, *Experimental and numerical analysis of the shear nonlinear behaviour of Nomex honeycomb core: Application to insert sizing*. Composite Structures, 2018. **193**: p. 121-139.
140. Sun, G., et al., *Experimental and numerical studies on indentation and perforation characteristics of honeycomb sandwich panels*. Composite Structures, 2018. **184**: p. 110-124.
141. Moghaddam, H.S., et al., *In-plane shear response of a composite hexagonal honeycomb core under large deformation—A numerical and experimental study*. Composite Structures, 2021. **268**: p. 113984.



142. Zamani, M.H., M. Heidari-Rarani, and K. Torabi, *Optimal design of a novel graded auxetic honeycomb core for sandwich beams under bending using digital image correlation (DIC)*. Composite structures, 2022. **286**: p. 115310.
143. Arslan, D., et al., *Formulation and characterization of polyetherimide composites reinforced with recycled carbon fibers and thermal black particles for Fused Filament Fabrication*. Composites Part A: Applied Science and Manufacturing, 2024, Submitted.
144. Arslan, D., et al., *Crystallinity, porosity, and microstructure of polyphenylene sulfide composite parts fabricated by filament-extrusion additive manufacturing* Composite Part B: Engineering, 2024, Submitted.

## APPENDIX A SEM AND EDS ANALYSIS OF RECYCLED CARBON FIBER SURFACE

**Figure A.1** presents the SEM images that provide a detailed surface analysis of the rCF. **Figure A.1.(a)** shows the surface morphology of the rCF, indicating the presence of residual sizing material. Sizing is a thin surface coating applied during fiber processing to protect the fibers and improve adhesion with polymer matrices. The micrograph highlights slight surface irregularities and visible residuals of the sizing layer distributed across the fiber surfaces.

**Figure A.1.(b)** presents the Energy Dispersive Spectroscopy (EDS) elemental mapping of the rCF surface. Elemental mapping reveals the distribution of carbon (C), nitrogen (N), oxygen (O), and trace amounts of fluorine (F), with their respective weight percentages being 88.29%, 9.04%, 2.47%, and 0.20%. Carbon (C) dominates the surface composition, confirming the primary presence of carbon fiber. Nitrogen (N), oxygen (O), and fluorine (F) are linked to the residual sizing layer, indicating organic compounds or functional groups on the fiber surface.

The EDS data and elemental mapping strongly suggest the presence of a sizing or coating on the carbon fiber surface. This sizing layer likely contains nitrogen and oxygen, which may be typical for polymer-based or functionalized sizing applied to carbon fibers for improved composite bonding. These findings could be linked to surface sizing agents like polyurethanes or epoxies.

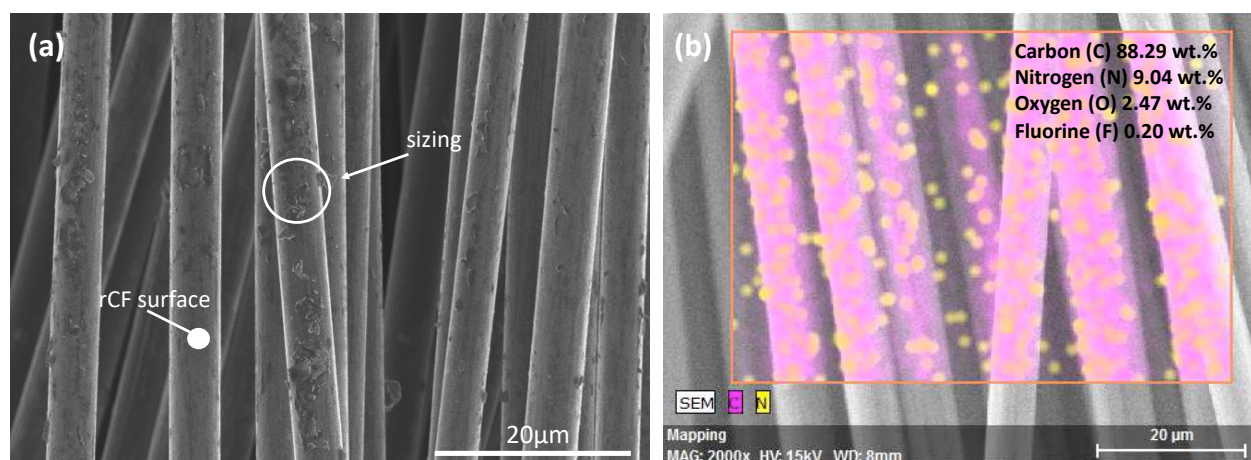


**Figure A.1** SEM and EDS characterization of rCF. (a) The image shows the surface morphology of rCF, highlighting the presence of residual sizing. (b) The image presents the EDS elemental mapping, indicating the distribution of carbon (C), nitrogen (N), oxygen (O), and fluorine (F) on the rCF surface.

## APPENDIX B THERMAL STABILITY AND FLAME SMOKE TOXICITY

### PROPERTIES OF PEI AND PPS COMPOSITES

#### B.1 Thermal stability of PEI and its composites

The thermal degradation behavior of the PEI and its composites was analyzed using TGA under air and nitrogen atmospheres to determine the effect of rCF and TB loading on the thermal stability of the developed composites. **Figure B.1** shows the TGA plots for the thermal behavior of the different formulations under non-isothermal and isothermal heating conditions. **Figure B.1(a)** and **B.1(b)** show the weight reduction of neat PEI with increasing temperature (non-isothermal heating) and time (isothermal heating) under nitrogen and air atmospheres, respectively. During non-isothermal heating, all the formulations are stable up to 500 °C, followed by a rapid drop in the mass, indicating thermal degradation until 800 °C. There is no significant effect of the type of the atmosphere on the onset degradation temperature. However, the thermal degradation is carried out in two fast clear stages under the air atmosphere, by opposition to that observed under the nitrogen atmosphere. For both the air and nitrogen atmospheres, the maximum rate of degradation is near 510°C, while the second step occurs at ~ 600 °C in the air atmosphere. The char residue content is approximately 50 wt.% in the nitrogen atmosphere, while it completely decomposes in the oxidative air atmosphere. Moreover, neat PEI is quite stable at 400 °C without significant weight loss under air and nitrogen atmospheres during isothermal heating. **Figure B.1(c)** shows the weight reduction of PEI composites with increasing temperature for three consecutive non-isothermal heating steps which refer to the compounding (380 °C), filament extrusion (390 °C), and FFF printing (400 °C) cycles, respectively. There is no adverse effect of the incorporation of rCF and TB on the thermal stability of the PEI composites since no significant difference in weight reduction is observed. The isothermal and non-isothermal TGA results showed that the PEI composites are thermally stable during the aforementioned composites processing cycles under air and nitrogen atmospheres.

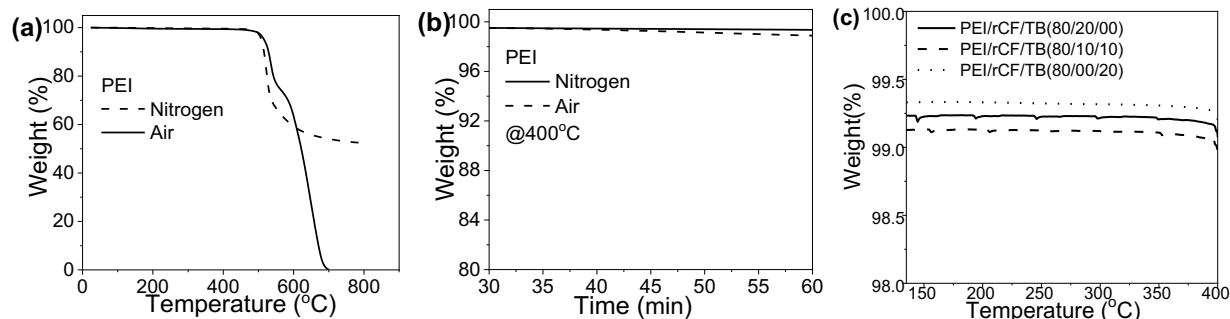


**Figure B.1** TGA graph of PEI and its composites: (a) non-isothermal, (b) isothermal heating for neat PEI under nitrogen and air atmospheres, (c) non-isothermal heating for PEI/rCF/TB (80/20/00), PEI/rCF/TB (80/10/10), and PEI/rCF/TB (80/00/20) composites. The results from both isothermal and non-isothermal TGA clearly demonstrate that the PEI composites exhibit a good thermal stability throughout the processing cycles involved.

## B.2 Fire Safety Performance

The flame smoke toxicity (FST) testing was conducted based on ASTM E662 – flaming mode, "Standard Test Method for Specific Optical Density of Smoke Generated by Solid Materials," to demonstrate that the developed composites are suitable for use in the aerospace and ground transportation industries based on their FST properties. In this context, the FST test specimens were FFF printed for a vertical burning test conducted over a period of 20 minutes. The results indicate that the developed PEI and PPS composites meet or exceed the preliminary FST criteria, making them strong candidates for industrial applications. The details of the results are as follows:

### B.2.1 Flammability

**Figure B.2** and **Table B.1** showed that all tested samples exhibited satisfactory fire resistance, with no dripping observed during the flammability tests. This indicates that the addition of rCF and TB did not negatively affect this crucial safety feature. The formulations of PEI/rCF/TB (80/20/00), PEI/rCF/TB (80/10/10), and PPS/rCF/TB (80/20/00) successfully passed the flammability test without any dripping, which is essential for minimizing fire hazards.

### B.2.2 Smoke Density

The smoke density after 4 minutes ( $D_s(4.0)$ ) was used to evaluate the materials' smoke release behavior in a fire scenario. As summarized in **Table B.1**, the PEI/rCF/TB (80/20/00), PEI/rCF/TB (80/10/10), and PPS/rCF/TB (80/20/00) formulations produced low smoke densities of 14, 15, and 68, respectively, well below the regulatory limit of 200. This suggests strong suppression of smoke

release, which is crucial for maintaining visibility during emergency evacuation. The slight increase in smoke density with the introduction of TB (from 14 to 15) shows a minimal impact on smoke suppression, while still maintaining excellent overall performance.

### B.2.3 Smoke Toxicity

The release of toxic gases such as hydrogen fluoride (HF), hydrogen chloride (HCl), hydrogen cyanide (HCN), sulfur dioxide (SO<sub>2</sub>), and nitrogen oxides (NO/NO<sub>2</sub>) were measured for the PEI/rCF/TB (80/20/00), PEI/rCF/TB (80/10/10), and PPS/rCF/TB (80/20/00) formulations. The results, listed in **Table B.1**, demonstrate the strong performance of all formulations in limiting the release of toxic gases, especially HF and HCl, which were kept well below the maximum permissible limits (HF < 100 ppm, HCl < 150 ppm). For PEI/rCF/TB (80/20/00) and PEI/rCF/TB (80/10/10), HF concentrations were as low as 0.4 ppm and 0.7 ppm, respectively, with no detectable HCl emissions in either case. Additionally, no detectable HF, HCl, or HCN concentrations were found in the PPS/rCF/TB (80/20/00) composites.

The release of HCN was significantly reduced when TB was introduced. The PEI/rCF/TB (80/10/10) formulation exhibited an HCN value of 20.0 ppm, a marked reduction from the 49.1 ppm recorded for the formulation containing 20 wt.% rCF, showcasing the effectiveness of TB in lowering this harmful gas. Both values remained well below the safety threshold of 150 ppm.

For SO<sub>2</sub>, both PEI formulations produced comparable results, with values of 24.6 ppm and 25.7 ppm for PEI/rCF/TB (80/20/00) and PEI/rCF/TB (80/10/10), respectively, well below the limit of 100 ppm. Although SO<sub>2</sub> concentrations were higher after 20 minutes of testing for the PPS formulation, this was expected due to the sulfur content in its matrix. However, the release rate of SO<sub>2</sub> remained low during the first 4 minutes of the test, ensuring that the PPS/rCF/TB composite passed the FST criteria.

Similarly, the release of nitrogen oxides (NO/NO<sub>2</sub>) was effectively controlled. The PEI/rCF/TB (80/10/10) formulation showed a 47.8% reduction in NO/NO<sub>2</sub> emissions compared to PEI/rCF/TB (80/20/00) (17.7 ppm vs. 33.9 ppm), demonstrating improved performance in reducing toxic NO/NO<sub>2</sub> emissions. The PPS/rCF/TB (80/20/00) formulation also met the criteria for NO/NO<sub>2</sub>, with low emissions of 7.7 ppm.

In conclusion, the PEI and PPS composites tested under ASTM E662 for FST performance exhibit excellent fire safety characteristics, low smoke release, and controlled toxic gas emissions, making them suitable for aerospace and ground transportation applications.

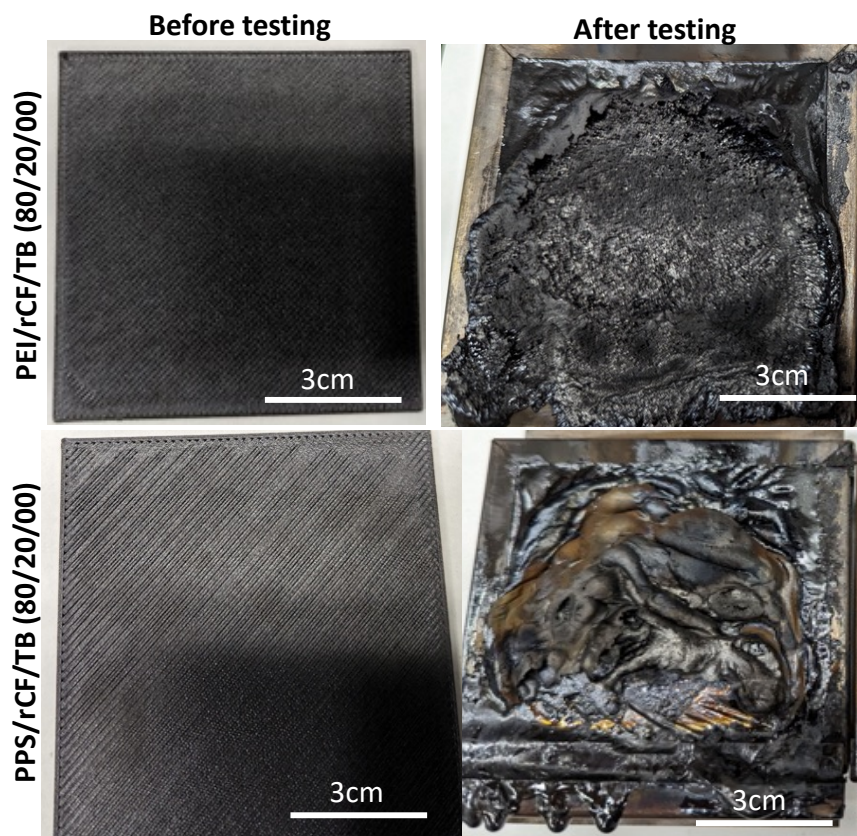


**Figure B.2** Images of FFF printed PEI/rCF/TB (80/20/00) and PPS/rCF/TB (80/20/00) composites before and after the 20-minute vertical burning test. The burned specimens showed no dripping and met the flammability criteria according to ASTM standards.

**Table B.1** Summary of flammability, smoke density, and smoke toxicity performance for FFF printed PEI and PPS composites after 20 min exposure of flame. This table presents the results of key fire safety performance indicators with their limits based on ASTM standards.

Test Method	Requirement/max limit	PEI/rCF/TB (80/20/00)	PEI/rCF/TB (80/10/10)	PPS/rCF/TB (80/20/00)
Flammability	No dripping	No dripping	No dripping	No dripping
Smoke density @4min (Ds(4.0))	<200	14.0	15.0	68
Smoke toxicity	HF <100 ppm	0.4	0.7	0
	HCl <150 ppm	0.0	0.0	0
	HCN <150 ppm	49.1	20.0	0
	SO <sub>2</sub> <100 ppm	24.6	25.7	641
	NO/NO <sub>2</sub> <100 ppm	33.9	17.7	7.7

## Acknowledgments

This work was done in collaboration with National Research Council of Canada through the project entitled 3DREAM, “*3D Research Ecosystem for Additive Manufacturing of Thermoplastic Composites*”. The work was founded by Natural Sciences and Engineering Research Council of Canada (*NSERC Alliance*, #560257-20) and PRIMA-Quebec (*Research and Development in Advanced Materials*, # R17-13-004). The authors gratefully acknowledge NRC’s technical team: Tarik Beragrag for extrusion of composites and filaments, Ali Ihid for extrusion and injection molding of composites, Patrick Gagnon for mechanical and HDT characterization, and Sajjad Saeidlou for some of the SEM observations. We also acknowledge Facundo Sosa-Rey, PhD, for his assistance with micro-CT image processing using the OpenFiberSeg tool.